Highly Precise MEMS Gyroscopes for Fully Automated Driving

DISSERTATION

zur Erlangung des Grades eines Doktors
der Ingenieurwissenschaften

vorgelegt von

M.Sc. Tobias Hiller

eingereicht bei der
Naturwissenschaftlich-Technischen Fakultät
der Universität Siegen

Siegen 2021

gedruckt auf alterungsbeständigem holz- und säurefreiem Papier

Betreuer und erster Gutachter
Prof. Dr.-Ing. Dr. h. c. Hubert Roth
Universität Siegen

Zweiter Gutachter
Prof. Dr.-Ing. Alfons Dehé
Albert-Ludwigs-Universität Freiburg

Tag der mündlichen Prüfung
1. Februar 2021

Declaration of Academic Integrity

Formulierung entsprechend §7 Promotionsordnung
Ich erkläre hiermit an Eides statt, dass ich die vorliegende Arbeit ohne unzulässige Hilfe Dritter und ohne Benutzung anderer, nicht angegebener Hilfsmittel angefertigt habe. Die aus anderen Quellen direkt oder indirekt übernommenen Daten und Konzepte sind unter Angabe der Quelle gekennzeichnet. Die Arbeit wurde bisher weder im In- noch im Ausland in gleicher oder ähnlicher Form einer anderen Prüfungsbehörde vorgelegt. Es wurden keine Dienste eines Promotionsvermittlungsinstituts oder einer ähnlichen Organisation in Anspruch genommen.

English Translation
I hereby declare in lieu of an oath that I have written the present work without any undue assistance by third parties and without using any aids other than the ones specified. The data and concepts taken, either directly or indirectly, from any other sources have been marked, indicating the source. The work has not been submitted to any other examining authority neither in Germany nor abroad and neither in the same nor in any similar form. Use of the services of any PhD mediation institute or of any similar organization has not been made.

Remark: Some texts, tables, figures and other content in this work have been previously published by me in similar or identical form in [1] [2], as well as in reporting documents of the TRACE and IPCEI projects. Permission of reuse has been granted by the IEEE Society.

S. Heller

Weil im Schönbuch, March 1, 2021

Place, Date

Signature

Acknowledgments

My sincere appreciation goes to Prof. Hubert Roth for his supervision and Prof. Alfons Dehé for being second examiner. I also want to thank Prof. Otmar Loffeld and Prof. Bhaskar Choubey for being part of the examination committee. Furthermore, I am deeply grateful for the advice and support of my advisors at Robert Bosch GmbH, Alexander Buhmann and Burkhard Kuhlmann. My research would not have been possible if I would not have gotten a head start in scientific practice at UC Santa Barbara. I want to thank Prof. Kimberly Foster as well as Lily Li for all their help and support.

I owe profound gratefulness to my colleagues at Bosch for their friendliness, for supporting my research in-between their daily work, for listening to my ideas and giving advice, for speeding up processes and for helping me with access to equipment. Among the many colleagues, I want to give special thanks to Timo Liewald, Thorsten Balslink, Rainer Schillinger, Marko Rocznik, Peter Degenfeld-Schonburg, Dusan Radovic, Markus Sonnemann and my mentor Mathias Reimann. I would like to acknowledge the dedication of students Bilel Djebali, Tim Häring, Steffen Tacke, Alexander Grauer, Fernando Valdespino, Michael Reibe, Marco Arena and Wolfram Mayer. Their work on the redundant inertial sensor platform has benefited my own research a lot. I would also like to thank my fellow PhD researchers within Bosch, especially Zsigmond Pentek, Keerthana Govindaraj, Ulrike Nabholz and Lukas Blocher.

I furthermore want to acknowledge Timon Huber, Anja Schöneck, Jonathan Rieger, Ulrich Klein and Heiner Lasi, as well as Shannon and Rick Mangrum, who all have helped me in countless ways. I am thankful beyond words for my parents Gudrun and Axel and my brother Simon as well as my grandparents Doris and Karl, who all have done everything to support my education. Above all, I received whatever small wisdom, strength, joy or favorable odds I had from the hands of my good Lord Jesus Christ.

Support

Robert Bosch GmbH

This creation of this dissertation was enabled by a three-year research contract within the department AE/EAC1 of Robert Bosch GmbH in Reutlingen, Germany. The content of this dissertation does not necessarily reflect the position or the policy of Bosch or her subsidiaries.

German Federal Ministry of Education and Research

This work was supported in part by the TRACE project within the research program ICT 2020 by the German Federal Ministry of Education and Research through the grant BMBF 16ES0488-16ES0502. No official endorsement by the funding agencies should be inferred.

German Federal Ministry for Economic Affairs and Energy

This work was supported in part by the IPCEI project by the German Federal Ministry for Economic Affairs and Energy by resolution of the German Bundestag. The grant number is BMWi 16IPCEI626. No official endorsement by the funding agencies should be inferred.

Abstract

Future, fully automated vehicles pose strict requirements on the performance of inertial sensors. Achievable accuracies of micro-electromechanical (MEMS) gyroscopes are however challenged by a number of non-idealities and long-term drift effects like bias instability. This dissertation analyzes the effect of bias instability on purely inertial navigation in comparison with other noise effects. It is shown, that bias instability becomes the dominant error component during navigation periods as short as ten seconds. At the core of the dissertation, origins and mechanisms of bias instability in triaxial, mode-matched, force-feedback MEMS gyroscopes are examined. Results gain credibility through a combination of analytical investigation, model-based simulation and extensive experimental analysis on real-world, next-generation sensor prototypes. It is found, that a combination of flicker noise on the frequency tuning voltage ensuring mode-matching together with certain types of rate offsets form a dominant source of bias instability. Feedback control on the frequency tuning voltage using pilot tones leads to an improvement of up to a factor of ten for the z-axis. Bias instabilities of lower than 0.1 dph are reached, which is an unprecedented value for automotive-type MEMS gyroscopes. The out-of-plane sensing x- and y-axes are shown to experience an additional, yet-unknown contribution of bias instability and could not be improved by frequency tuning control. For the first time, scale-factor instability was described and analyzed in detail. This effect produces an increase in signal drift with higher measured angular rates. Lastly, a novel measure for mode-matching was devised, which, contrarily to the pilot tone scheme, only uses the existing noise in the gyroscope's force-feedback structure to estimate the sense mode's detuning and scale-factor.

Keywords

MEMS, gyroscope, triaxial, navigation, automated driving, mode-matched, Allan variance, bias instability, frequency tuning, scale-factor instability

Zusammenfassung

Zukünftige, vollautomatisierte Fahrzeuge stellen strenge Anforderungen an die verwendete Inertialsensorik. Die Genauigkeit von MEMS Drehratensensoren wird durch eine Vielzahl an Nichtidealitäten und langsamen Drifteffekten wie Biasinstabilität begrenzt. Diese Dissertation befasst sich mit dem Einfluss von Biasinstabilität auf die Genauigkeit von rein inertialer Navigation im Vergleich zu anderen Rauschtypen. Es wird aufgezeigt, dass sich Biasinstabilität bereits bei Navigationsdauern über zehn Sekunden als größter Fehleranteil erweist. Im Hauptteil der Arbeit werden Ursprünge und Mechanismen von Biasinstabilität in dreiachsigen MEMS Drehratensensoren mit identischen Antriebs- und Detektionsmodenfrequenzen und Kraftrückkopplung untersucht. Dies findet unter Einbeziehung von analytischen Berechnungen, ausführlicher Systemmodellierung und -simulation sowie experimentellen Untersuchungen an aktuellen Prototypen statt. Es wird gezeigt, dass eine Kombination aus Flickerrauschen auf der Frequenztuningspannung der Detektionsmode sowie gewissen Offsets die dominante Quelle für Biasinstabilität in den z-Achsen darstellt. Wird die Frequenztuningspannung geregelt und damit die Resonanzfrequenz der Detektionsmode in Relation zur Antriebsmode konstant gehalten, kann die Biasinstabilität um bis zu einem Faktor zehn auf unter $0.1\,°/\mathrm{h}$ verbessert werden. Hierbei findet die Messung der Resonanzfrequenz der Detektionsmode unter Verwendung von sogenannten Pilottönen statt. Für die senkrecht zur Sensorebene messenden x- und y-Achsen besteht eine weitere, unbekannte Ursache von Biasinstabilität. Eine Reduktion mittels der genannten Methode ist hierbei nicht möglich. Darüber hinaus wird zum ersten Mal in der Literatur ein Effekt der Empfindlichkeitsinstabilität detailliert beschrieben, welcher als ein Anwachsen von Drift bei größeren gemessenen Drehraten auftritt. Zuletzt wird eine neuartige Methode entwickelt, die eine Identifikation von Detektionsmodenfrequenz und Sensorempfindlichkeit im Betrieb allein aufgrund des Rauschens in der Kraftrückkopplung ermöglicht. Im Gegensatz zum Pilottonverfahren benötigt diese Methode keine Injektion von zusätzlichen Signalen in den Regelkreis.

Schlüsselworte

MEMS, Drehratensensor, dreiachsig, Navigation, Automatisiertes Fahren, Allan Varianz, Biasinstabilität, Frequenztuning, Empfindlichkeitsinstabilität

List of Publications

L. Li, **T. Hiller**, B. Bamieh, and K. Turner, “Amplitude control of parametric resonances for mass sensing,” in *IEEE Sensors 2014*. IEEE, 2014, pp. 198-201.

T. Hiller, L. Li, E. Holthoff, B. Bamieh, and K. Turner, “System identification, design and implementation of amplitude feedback control on a nonlinear parametric MEM resonator for trace nerve agent sensing,” in *IEEE Journal of Microelectromechanical Systems*, vol. 24, no. 5, pp. 1275-1284, 2015.

E. Holthoff, L. Li, **T. Hiller**, and K. Turner, “A molecularly imprinted polymer (MIP)-coated microbeam MEMS sensor for chemical detection,” in *Chemical, Biological, Radiological, Nuclear, and Explosives (CBRNE) Sensing XVI.* Vol. 9455. International Society for Optics and Photonics, 2015.

T. Hiller, B. Kuhlmann, A. Buhmann, and H. Roth, “Noise contributions in a closed-loop MEMS gyroscope for automotive applications,” in *IEEE Int. Symposium on Inertial Sensors and Systems 2017.* IEEE, 2017, pp. 62-65.

Z. Pentek, **T. Hiller**, T. Liewald, B. Kuhlmann, and A. Czmerk, “IMU-based mounting parameter estimation on construction vehicles,” in *DGON Inertial Sensors and Systems (ISS) 2017.* IEEE, 2017, pp. 1-14.

T. Hiller, Z. Pentek, T. Liewald, A. Buhmann, and H. Roth, “Origins and Mechanisms of Bias Instability Noise in a 3-Axis Mode-Matched MEMS Gyroscope,” in *IEEE Journal of Microelectromechanical Systems*, vol. 28, no. 4, pp. 586-596, 2019.

L. Blocher, F. Baklanov, **T. Hiller**, M. Rocznik, J. Gerlach, and O. Bringmann, “An Experimental Localization Sensor Platform for Enhanced Initial Heading Estimation,” in *IEEE International Symposium on Inertial Sensors and Systems 2020.* IEEE, 2020, pp. 1-2.

Z. Pentek, **T. Hiller**, and A. Czmerk, “Algorithmic Enhancement of Automotive MEMS Inertial Sensors with Consumer-Type Redundancy,” in *IEEE Sensors Journal*, vol. 21, no. 2, pp. 2092-2103, 2021.

L. Blocher, W. Mayer, M. Arena, D. Radovic, **T. Hiller**, J. Gerlach, and O. Bringmann, “Purely Inertial Navigation with a Low-Cost MEMS Inertial Sensor Array,” in *IEEE International Symposium on Inertial Sensors and Systems 2021*. IEEE, 2021, in press.

T. Hiller, L. Blocher, M. Vujadinovic, Z. Pentek, A. Buhmann and H. Roth, “Analysis and Compensation of Cross-Axis Sensitivity in Low-Cost MEMS Inertial Sensors,” in *IEEE International Symposium on Inertial Sensors and Systems 2021*. IEEE, 2021, in press.

List of Patent Applications

K. Govindaraj and **T. Hiller**, *"Method for creating an object map for a factory environment,"* publicized as P.C.T. patent WO 2019/025221 A1 and German patent DE 10 2017 213 601 A1, February 2019.

T. Hiller and K. Govindaraj, *"Verfahren zum Betreiben eines kollaborativen Roboters,"* publicized as German patent DE 10 2017 221 305 A1, May 2019

Z. Pentek, **T. Hiller**, B. Kuhlmann, T. Liewald and T. Fischl *"Datenfusioniertes Sensorsystem,"* patent application submitted and under review, May 2019.

T. Hiller, Z. Pentek, B. Kuhlmann, T. Liewald and A. Buhmann *"Vorrichtung und Verfahren zum Betreiben eines Inertialsensors,"* patent application submitted and under review, October 2019.

T. Hiller, Z. Pentek and A. Buhmann *"Methode zur Messung von Empfindlichkeitsänderungen bei MEMS Drehratensensoren,"* patent application submitted and under review, March 2020.

List of Supervised Works

B. Djebali, “Characterization, Modelling and Data Fusion of MEMS Inertial Sensors for High Performance Applications,” supervised in part, *Master’s thesis, Technical University of Munich*, 2016.

T. Häring, “Redundant MEMS Inertial Sensors for High-Performance Navigation Application,” *Bachelor’s thesis, Eberhard Karls University Tübingen*, 2017.

S. Tacke, “Graphical User Interface for a Demonstrator with Redundant MEMS Inertial Sensors for High-Performance Inertial Navigation Applications,” *Bachelor’s thesis, Eberhard Karls University Tübingen*, 2017.

A. Grauer, “Entwicklung und Simulation eines Empfängers für ein Software-Defined Radio GPS,” *Master’s thesis, Reutlingen University*, 2018.

F. Valdespino Vaca, “Internship Report (Sources of Bias Instability Noise in Open-Loop MEMS Gyroscopes),” *Internship, University of Stuttgart*, 2018.

M. Reibe, “Internship Report (Characterization of High-Performance Consumer-Type Inertial Sensors for Navigation Applications),” *Internship, Ilmenau University of Technology*, 2019.

M. Arena, “Indoor Navigation mit redundanten MEMS Inertialsensoren am Beispiel eines Werkzeugwagens,” *Bachelor’s thesis, Reutlingen Univ.*, 2020.

W. Mayer, “Indoor Navigation with Redundant MEMS Inertial Sensors Using Motion Constrains,” currently ongoing, *Bachelor’s thesis, Baden-Wuerttemberg Cooperative State University (DHBW)*, 2020.

L. Blocher, “Initial Heading Estimation for Automated Driving Using Dual-GNSS Receivers (preliminary title),” *Ph.D. dissertation, Eberhard Karls University Tübingen*, currently ongoing.

Nomenclature

List of Symbols

Chapter 2	
Q_z	quantization noise coefficient
Q	angle random walk coefficient
B	bias instability coefficient
K	rate random walk coefficient
R	drift rate ramp coefficient
f	frequency
Ω	angular rate
σ_{AD}	Allan deviation
T_s	sample time
τ_{AD}	Allan deviation cluster time
S_{PSD}	one-sided power spectral density
S_{2PSD}	two-sided power spectral density
$\sigma_{\mathrm{ARW}}, \sigma_{\mathrm{VRW}}$	angle/velocity random walk
σ_{BIS}	bias instability
σ_{RRW}	rate random walk
Ω_b, Ω_n	angular rate in body/navigation frame
ϕ_n, θ_n, ψ_n	attitude in navigation frame
f_b, f_n	specific force in body/navigation frame
v_n	velocity in navigation frame
x_n, y_n, z_n	position in navigation frame
g	gravity
Ω_{true}	ground-truth angular rate
Ω_{ARW}	angle random walk angular rate
Ω_{BIS}	bias instability angular rate
f_{true}	ground-truth specific force
f_{VRW}	velocity random walk specific force
f_{BIS}	bias instability specific force
t	time
σ	standard deviation
$\sigma_{\phi/\theta/\psi,\mathrm{ARW}}$	angle error due to angle random walk
$\sigma_{\phi/\theta/\psi,\mathrm{BIS}}$	angle error due to bias instability
$\sigma_{x/y/z,\mathrm{ARW}}$	position error due to angle random walk
$\sigma_{x/y/z,\mathrm{BIS}}$	position error due to bias instability

Chapter 3

F_{cor}	Coriolis force
m	mass
v	velocity
Ω_{r}	applied angular rate
F_{para}	force of parallel plate capacitor
F_{comb}	force of comb drive capacitor
x	drive displacement
y	sense displacement
u	additional mode displacement
F_{dr}	drive force
F_{sn}	sense feedback force
k_{dr}	drive force efficacy
k_{fb}	sense feedback efficacy
ω	frequency
ω_{pll}	drive frequency
V_{DR}	drive voltage
V_{FB}	feedback voltage
c	damping
k	stiffness
k_{gyr}	gyroscopic factor
k_{xy}	quadrature coefficient
c_{xy}	non-proportional damping
k_{df}	drive force coupling coefficient
k_{xu}	excitability of additional mode
k_{cvd}	electrical cross-coupling on CV converter
$k_{\mathrm{cv}y}$	efficacy of sense displacement on CV converter
$k_{\mathrm{cv}u}$	additional mode effect on CV converter
V_{QC}	quadrature compensation voltage
V_{QCM}	quadrature common-mode compensation voltage
k_{q}	quadrature compensation capability
V_{FT}	frequency tuning voltage
k_{ft}	spring softening capability
$k_{x\mathrm{d}}$	duffing coefficient
ω_{mec}	mechanical frequency of drive mode
V_{CV}	CV converter output voltage
H_{sns}	transfer function of sense mode
H_{CV}	transfer function of CV converter
H_{ADC}	transfer function of sense ADC
H_{fctrl}	transfer function of force-feedback control
H_{fDAC}	transfer function of force-feedback DAC
$H_{\Omega_{\mathrm{r}}\dot{x}\to\star}$	closed-loop rate transfer function
$H_{k_{\mathrm{cvd}}V^2\to\star}$	closed-loop CV transfer function

k_{fDAC}	force-feedback DAC efficacy
ω_{pt}	pilot-tone frequency
S_{pt}	pilot-tone signal
k_{pt}	pilot-tone signal amplitude
ω_{dr}	drive mode natural frequency
ω_{sn}	sense mode natural frequency
$\Delta\omega_{\mathrm{split}}$	frequency split between drive and sense modes
S_{PSD}	one-sided power spectral density
$V_{\mathrm{FB,flic}}$	force-feedback DAC flicker noise
$V_{\mathrm{QC,flic}}$	quadrature control DAC flicker noise
$V_{\mathrm{QCM,flic}}$	quadrature common-mode DAC flicker noise
$V_{\mathrm{FT,flic}}$	frequency tuning DAC flicker noise
$V_{\mathrm{DR,flic}}$	drive DAC flicker noise
$V_{\mathrm{PLL,flic}}$	analog PLL voltage flicker noise
$S_{\mathrm{ADC,dr,flic}}$	drive ADC scale-factor flicker noise
$S_{\mathrm{ADC,sn,flic}}$	sense ADC scale-factor flicker noise
ΔV_{FT}	frequency *de*tuning voltage
S_V	susceptibility of offset due to voltage change
Ω_{np}	rate offset due to non-proportional damping
Ω_{fc}	rate offset due to drive force coupling
Ω_{uq}	rate offset due to uncompensated quadrature
Ω_{ec}	rate offset due to electrical cross-coupling
Ω_{am}	rate offset due to an additional mode
σ_{SIS}	scale-factor instability
$\mathrm{SF}_{V_{\mathrm{FB}}}$	scale-factor due to feedback voltage change
$\Delta\mathrm{SF}_{V_{\mathrm{FB}}}$	scale-factor difference due to feedback voltage change

Chapter 4

d_1	$\Delta\Sigma$ ADC dither signal
d_2	$\Delta\Sigma$ DAC dither signal
q	$\Delta\Sigma$ DAC quantization noise
u_1	estimation input signal
u_2	estimation output signal
$u_{1,\mathrm{r}}$	rectified estimation input signal
$u_{2,\mathrm{r}}$	rectified estimation output signal
H_{sns}	sense mode transfer function
k_{cv}	relationship of capacitance to voltage
$k_{x\mathrm{c}}$	relationship of displacement to capacitance
H_{adc}	ADC transfer function
k_{fdac}	gain of the force-feedback DAC
k_{vc}	relationship of voltage to capacitance
$k_{\mathrm{c}x}$	relationship of capacitance to displacement
u	output signal of the force-feedback control

y	output signal of the force-feedback $\Delta\Sigma$ DAC
s	input signal to the force-feedback $\Delta\Sigma$ DAC quantizer
k_q	linearized quantizer gain
H_stf	$\Delta\Sigma$ DAC signal transfer function
$H_\mathrm{ntf,1}$	$\Delta\Sigma$ DAC noise transfer function for the dither d_2
$H_\mathrm{ntf,2}$	$\Delta\Sigma$ DAC noise transfer function for quantization noise q
$H_{\Delta\Sigma\text{-dac}}$	$\Delta\Sigma$ DAC transfer function
x'	input of the output-error estimation model
y'	output of the output-error estimation model
n_k	delay of the output-error estimation model
e	noise input of the output-error estimation model
t	time of the output-error estimation model
ΔV_FB	feedback voltage change
ΔV_FT	frequency detuning voltage
SF	scale-factor
$\Delta\omega_\mathrm{split}$	frequency split between drive and sense modes
$\sigma_{\mathrm{AD},\Delta\omega_\mathrm{split}}$	Allan deviation of the frequency split estimate
$\sigma_{\mathrm{AD},\Delta\mathrm{SF}}$	Allan deviation of the scale-factor estimate
y_sub	output y with subtracted in-band frequency content

Appendix

w	mean-free, discrete, random, white noise process
k	sample step
N	total amount of samples
τ_0	constant sample time
σ_w	standard deviation of white noise
t	time
σ_ARW	angle random walk
Q	angle random walk coefficient
$\sigma_\mathrm{1/f}$	standard deviation of 1/f noise
ω_1, ω_2	angular frequency
S_PSD	one-sided power spectral density
S_2PSD	two-sided power spectral density
f_1, f_2	lower/upper frequency limit of 1/f behavior
T_1	time constant of lower frequency limit of 1/f behavior
T_end	measurement duration
N_1Hz	1/f noise magnitude at 1 Hz
σ_BIS	bias instability
B	bias instability coefficient
$\sigma_{\theta,\mathrm{BIS}}$	angle error of integrated bias instability
v	discrete, random, 1/f noise process
R_{vv}	autocovariance of v
γ	Euler-Mascheroni constant

Ω_T	temperature induced offset drift
θ_T	temperature induced angle error
x_T	temperature induced position error
k_T	temperature coefficient of the offset (TCO)
ΔT	temperature change
S_{pt}	pilot tone signal
k_{pt}	pilot tone magnitude
ω_{pt}	pilot tone frequency
ω_{pll}	drive frequency
k'_{pt}	amplified pilot tone magnitude
ϕ_{pt}	pilot tone phase change
k_{det}	increase or reduction in pilot tone magnitude
D_{pt}	detuning measure
$D_{\mathrm{pt,lp}}$	low-pass filtered detuning measure
$S_{\mathrm{pt,det}}$	force control output signal
B	bias instability coefficient
V_{flic}	flicker noise voltage
S_V	susceptibility of offset due to voltage change
Ω	angular rate
V_{FB}	feedback voltage
ΔV_{FB}	small feedback voltage variation
$V_{\mathrm{FB,flic}}$	feedback voltage flicker noise
k_{fDAC}	relation between digital signal and feedback force
k_{fb}	relation between voltage and feedback force
$V_{\mathrm{fDAC,full\text{-}scale}}$	full-scale voltage DAC range
$\mathrm{LSB}_{\mathrm{fDAC,full\text{-}scale}}$	full-scale LSB range
$\mathrm{SF}_{V_{\mathrm{FB}}}$	scale factor depending on feedback voltage
ω_y	sense mode resonance frequency
$H_{\Omega_{\mathrm{r}}\dot{x}\rightarrow\star}$	closed-loop rate transfer function
$H_{k_{\mathrm{cvd}}V^2\rightarrow\star}$	closed-loop CV transfer function

List of Abbreviations

AD	Allan deviation
ADC	analog-to-digital converter
AMM	automatic mode-matching
ARMAX	autoregressive–moving-average model w. exogenous inputs
ARW	angle random walk
ASIC	application-specific integrated circuit
BASt	German federal highway research institute
BAW	bulk acoustic wave
BIS	bias instability
CLCC	ceramic leaded chip-carrier
CV	capacitance-to-voltage converter
DAC	digital-to-analog converter
DoF	degrees of freedom
DRIE	deep reactive ion etching
DRR	drift rate ramp
ESC	electronic stability control
FFB	force-feedback
FFT	fast Fourier transform
FOG	fiber optic gyroscope
FPGA	field-programmable gate array
GNSS	global navigation satellite systems
IMU	inertial measurement unit
INS	inertial navigation system
LP	low-pass
LSB	least significant bit
MEMS	micro-electromechanical systems
NHTSA	US national highway traffic safety administration
OEDR	object and event detection and response
OL / CL	open-loop / closed-loop
PCB	printed circuit board
PLL	phase-locked loop
PSD	power spectral density
PT	pilot tone
QC	quadrature compensation
RAV	root Allan variance
RLG	ring laser gyroscope
RRW	rate random walk
SMID	simultaneous mode identification
TCO	temperature coefficient of the offset
VRW	velocity random walk
WSS	wheel speed sensors

Contents

1. Introduction

This chapter provides a brief introduction and acts as motivation for the dissertation. Recent developments in automated driving are illustrated and the role of micro-electromechanical systems (MEMS) inertial sensors in navigation, especially during emergency-stop maneuvers, is highlighted. Lastly, the importance of long-term stability of the MEMS gyroscope output is demonstrated and the dissertation objective is substantiated. Detailed state-of-the-art summaries for highly precise MEMS gyroscopes are presented in Chapters 3 and 4.

1.1. Automated Driving

The promises of automated driving impel research institutions and industry worldwide to wide-ranging technological efforts [3]. Individual mobility is likely to change in a way unseen since the mass-adoption of the automobile [4]. Among the technologies' promises are fewer accidents, less traffic congestion, cost savings, lower environmental impact, mobility for non-drivers and the elderly, reduced stress, freed-up time and in general solutions to the transportation problem of the future's mega-cities [5] [6]. Particularly the reduction of accidents stands out, as the vast majority of them are caused by human error - more than 90 percent in the United States [7]. Worldwide, yearly traffic fatalities amount to an epidemic-like 1.35 million and traffic has in fact become the number one cause of death for people between 5 to 29 years of age [8]. Automated driving offers a solution by partly or entirely removing the human factor from driving.

The SAE International's description of an automated driving system is "The hardware and software that are collectively capable of performing the entire dynamic driving task on a sustained basis [...]" [9, p. 3]. Among the many terms that are used in public discourse like "robotic", "self-driving", "autonomous", "unmanned" or "driverless", only "automated" is precise and technically correct and is therefore suggested by SAE International as the sole descriptor [9]. This dissertation therefore follows that notion. The German Federal Highway Research Institute (BASt) in 2012 and the US National Highway Traffic Safety Administration (NHTSA) shortly after, developed descriptions of automated driving based on levels [4] [10]. In 2016, the SAE International largely sided with the German framework, added a further level and thereby created the current de-facto standard. It comprises six levels from 0 to 5 [9]: Level 0 contains no driving automation, level 1 has driver assistance with a sustained driving automation system for *either* longitudinal *or* lateral motion control. Level 2 is described as partial driving automation where *both* longitudinal and lateral motion control are active. Here, the driver is expected to continuously *supervise* the driving automation system as it is only partially capable of object and event detection and response (OEDR) functions. Actual automated driving begins at level 3, called conditional driving automation, where the *complete* OEDR is managed by the automated driving system and the driver is merely responsible for being “fallback-ready” in the event of vehicle or automated driving system failure. Level 4 shifts the fallback responsibility to the automated driving system and is named high driving automation. The difference to level 5 full driving automation is that level 4 is domain specific, e.g. only certain areas, speeds, daytimes or weather conditions, whereas level 5 is unlimited in its domain. Figure 1.1 shows an overview of the SAE International’s framework.

It is important to note that none of the levels are characterized by the absence of e.g pedals or steering wheel and in fact a level 5 capable vehicle might still be driven by a human driver if they chose to deactivate the automated driving system. At the same time level 4 automated driving is already reality today by this definition, e.g. by passenger shuttles on research campuses [9]. A level 4 or 5 vehicle may furthermore still *suggest* the driver taking over the driving task, but will still arrive at a minimal risk condition if the driver does not react to the prompt [9]. The feasibility of level 3 automated driving is challenged by a series of studies and ample experiences from aviation [11] [12] [13]. The main issue is that humans perform terribly when made the fallback option within prolonged automated operation, particularly in the area of cognition [14]. Suddenly putting the driver on the spot in an extreme situation that the automated driving system was not able to manage, seems unwise [13]. Level 3 systems might therefore not see large-scale adoption [15] and markets may move straight to level 4.

Within level 4 and 5, the reply to automated driving system and/or vehicle failure or departure of the operating domain is the achievement of a minimal risk condition [9]. While this generic term includes all kinds of possibilities, the most practicable solution is to bring the vehicle to a halt for further measures like restarting the software, take-over by a remote operator or pick-up for repair [9] [16] [17]. An emergency stop maneuver may include driving onto the road shoulder or simply stopping in lane with hazard flashers turned on. The occasionally used description “safe-stop” is therefore somewhat deceiving, as standing in lane might provoke accidents nonetheless. In any case, the minimal risk condition is met, as continuing at speed would harbor much higher risks. For this work, a maximum highway speed of 130 kmph is assumed [17], which would put a realistic stop maneuver at a duration of 10 to 20 seconds. Depending on the exact failure mode, the vehicle has to follow a pre-calculated emergency stop trajectory with reduced or complete lack of OEDR capabilities [9] [16]. Level 3 systems may also perform some forms of emergency stop maneuvers in order to give the driver more time for take-over.

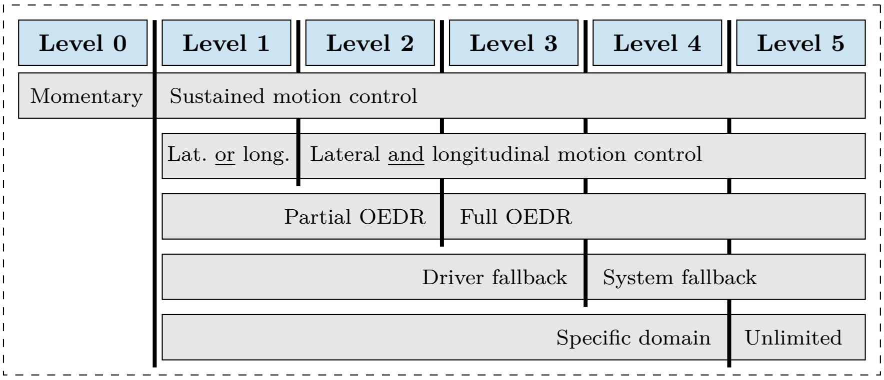

Figure 1.1.: Automated driving divided into five levels according to the SAE International definition. This graphic was derived from [9, p. 25, Fig. 11].

The reliability, performance, form-factor and affordability of sensor systems are at the center of the technological advancement of automated driving [18]. It remains to be seen which types and combinations of sensors are truly obligatory [18]. At the same time, sensor-fusion and decision-making algorithms and architectures constitute a vast field of research for years to come [3] [17]. With changing societal perception [19], jurisdictional requirements, customer expectations and behavior [20] as well as entirely novel business models [21], new engineering requirements may emerge, such as faster development cycles or increased focus on performance versus price. The field of automated driving systems is moreover marked by the presence of not only established vehicle manufacturers, but also Tier-1 suppliers, IT-companies and start-ups [6]. Lastly, the close interconnection of automated driving with vehicle connectivity and electrification shall be mentioned. For further information on the state-of-the-art and outlook of automated driving systems, the reader is referred to these excellent review articles [3] [5] [18] [21] [22].

1.2. Inertial Sensing

A prime aspect of automated driving systems is navigation, both relative to the vehicles surroundings and in absolute terms on a local or global map. In general, cm-precision is required for successfully navigating within road lanes [17] [23]. Types of sensors employed in automated driving systems include among others, mono and stereo cameras, radio detection and ranging (radar), light detection and ranging (lidar), sound navigation and ranging (sonar), global navigation satellite systems (GNSS), inertial measurement units (IMUs) and wheel speed sensors (WSS) [3] [24], all of which may aid in the navigation task during times of sufficient automated driving system availability. Sensors may be categorized into proprioceptive, i.e. self-sensing, and exteroceptive, i.e. surround-sensing, physical principles [3]. This dissertation bases on the assumption, that the automated driving system will resort to proprioceptive sensors during an emergency stop maneuver, as the actual need for reaching a minimal risk condition is typically predicated on the unavailability of some or all exteroceptive sensors or their subsequent processing. Practical examples include cameras being blinded by low-standing sun, radar sensors being fooled by aluminum food packaging, lidar sensing being hindered by snow or GNSS signals deteriorating due to urban environments, tree lines and tunnels [3] [25]. Active sensors like radar, lidar and sonar also suffer from signal interferences due to other traffic participants with similar sensors, which necessitates encoding [26].

Inertial sensors based on MEMS technology are already present in virtually all modern cars [27]. The main use cases are crash and roll-over detection for airbag release as well as electronic stability control (ESC) [28]. Automotive-grade MEMS inertial sensors have been well-proven in terms of reliability, availability, longevity and safety for over a decade [29]. They have very small form-factor, are inexpensive, require little computing power and can hardly be disturbed by external effects such as electromagnetic influences or vibration [29]. These unique properties make MEMS inertial sensors suited candidates for providing the necessary motion data for an emergency stop maneuver [16], especially when combined with wheel speed sensors [30] [31]. An inertial measurement unit tracks linear acceleration, or more accurately, specific force, and angular rate. A difference to crash detection and ESC inertial MEMS is the number of sensing axes, which must be a minimum of three, one for each spacial dimension, for accelerometers and gyroscopes in an IMU [32].

MEMS technology is characterized by engineering at the micro-meter scale or below, typically done by lithography and bulk etching techniques on flat wavers [33]. Silicon and silicon-oxide are oftentimes the materials of choice [33]. Depending on device size, tens of thousands of devices may be fabricated on a single wafer, making MEMS technology cheaper per device than most other manufacturing methods [34]. The deep reactive ion etching (DRIE) technique [35] [36], also called the Bosch-process, has enabled or advanced a plethora of different MEMS devices such as microphones, microfluidic actuators and sensors, micromirrors, radio-frequency devices, pressure sensors, accelerometers and gyroscopes [29] [33] [37]. The micro-scale active masses of inertial MEMS stand in direct opposition to signal-to-noise and signal-to-disturbance ratios while measuring inertial forces, compare with [38]. MEMS inertial sensors are therefore seen as the least precise inertial sensor type [39]. Optical devices such as ring laser gyroscopes (RLG) and fiber optic gyroscopes (FOG) employ the Sagnac interference effect and offer higher performance than MEMS [39] [40]. Surprisingly, the most precise gyroscopes are again (large) mechanical devices with rotating masses which are used primarily for strategic missiles [41] [42]. The high cost of the non-MEMS devices allows for use in airplanes, spacecraft, weapon systems, submarines or drilling equipment [43] but is very likely prohibitive for automated driving systems. Recent developments toward the improvement of MEMS sensors specifically for defense applications resulted in MEMS devices with performance close to FOG levels, compare e.g. [44].

Inertial sensors by themselves can only offer *relative* navigation from a known starting point, known as dead-reckoning [43]. An IMU can provide position and orientation data by employing a strap-down mechanism within an inertial navigation system (INS) [25]. The exact algorithm is shown in the next chapter. Specific force and angular rate along with any errors are integrated two and three times, respectively, which explains why gyroscope performance is typically more important compared to the accelerometers assuming both are based on similar technology. Inertial sensor errors are discerned into stochastic and systematic effects [45] [46]. Systematic effects can be calibrated and include errors like offset, scale factor, scale factor nonlinearity, misalignment of axes, misalignment of the entire device, cross-axis sensitivity as well as the changes of each effect over temperature, stress or humidity [45] [47]. Kalman filter estimation while moving and tumbling the device in an angular rate chamber is an established technique [48]. Recent results suggest, that typical automotive and even consumer drone movement profiles might not excite MEMS inertial sensors enough to make all Kalman filter error states observable and to calibrate it in the field [45] [49]. Among the stochastic effects in each sensor output white noise, also called angle/velocity random walk (ARW/VRW), and bias instability (BIS) [50] are most important. Particularly gyroscope bias instability is central to long-term precision of an INS, which is why bias instability, along with angle random walk and scale factor stability, is usually the prime performance measure of gyroscopes [34] [40] [41] [43] [51] [52].

Apart from automotive use, MEMS inertial sensors have found widespread adoption in the consumer segment, notably in smartphones, wearables and drones [32] [53]. In the consumer market, the volumes sold exceed automotive qualified MEMS devices by far. Robert Bosch GmbH alone has sold its ten billionth MEMS sensor recently, of which most were consumer type [54]. The consumer market offers equally promising developments compared to automated driving like indoor navigation [55] [56] [57] and augmented/mixed reality [58]. These fields also request for higher inertial navigation precision [55] [58]. As the fundamental measurement principle is the same for automotive and consumer gyroscopes, the latter will benefit from the results in this dissertation, too.

1.3. Dissertation Outline

Above, the relevance of highly precise MEMS gyroscopes for automated driving systems was established. Out of the manifold sensor error sources affecting navigation accuracy and precision, the dissertation will focus on the understanding and improvement of MEMS gyroscope bias instability. Figure 1.2 shows the

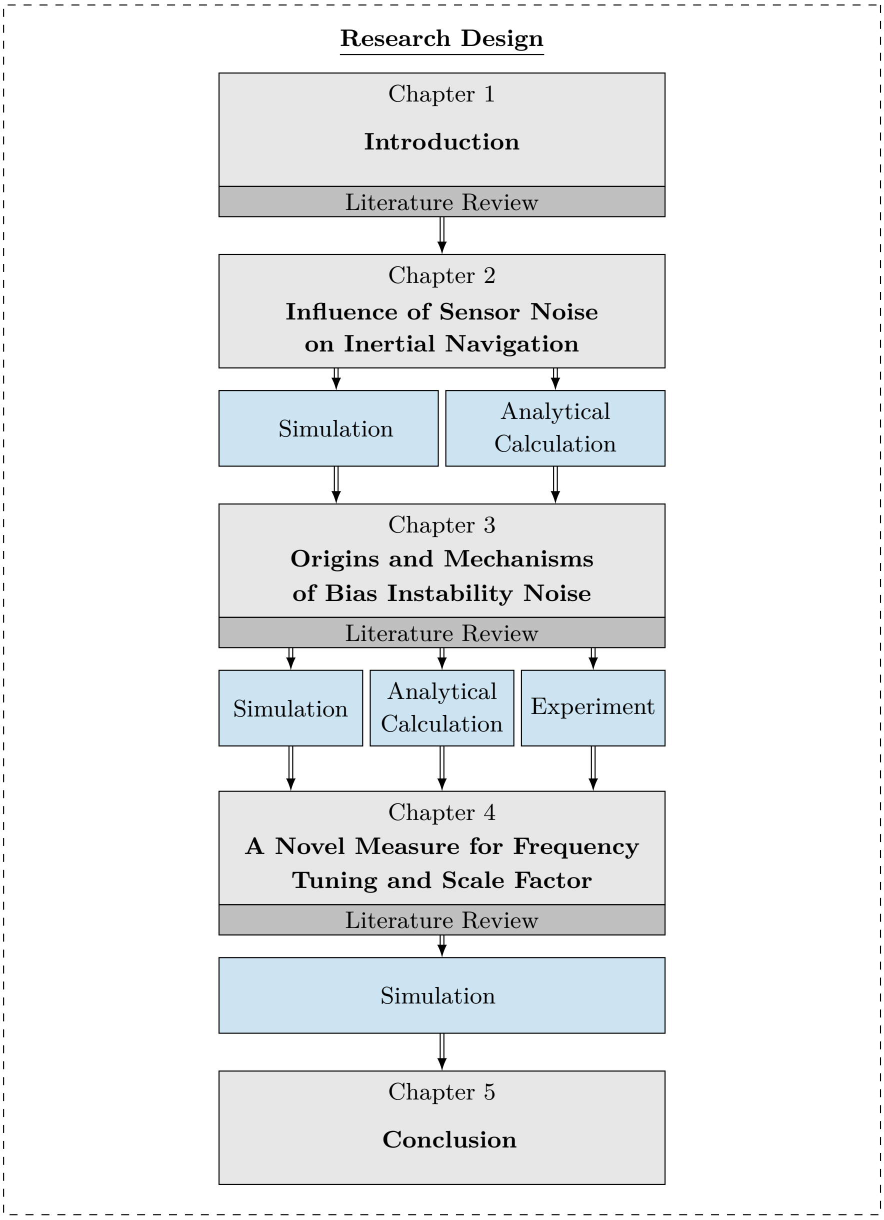

Figure 1.2.: Research design and dissertation outline. The adequacy of the methods (*blue*) to address each topic is discussed in the corresponding chapters.

research design of the dissertation alongside the division into chapters.

Following the introduction and a broad literature review in this chapter, Chapter 2 aims to examine the influence of bias instability and white noise on purely-inertial emergency stop maneuvers on the basis of analytical calculations and iterative simulations. The relevance of gyroscope bias instability is substantiated and a theoretical background on each of the different noise types is provided. Chapter 3 comprises the central contribution of the dissertation. Its aims are (i) to analyze the experimental as-is performance of a triaxial, automotive-grade MEMS research gyroscope by Robert Bosch GmbH, (ii) to thoroughly understand sources of bias instability with the help of simulations, analytical calculations and experiments, and lastly (iii) to improve bias instability in experiment through suitable mechanisms, like test signals. A comprehensive literature review of the state of the art on the matter will be offered beforehand. Chapter 4 applies the findings to a simulation study of a novel estimation algorithm that aims to improve bias instability without the need for test signals. A further state-of-the-art summary relates the proposed algorithm to existing methods. Chapter 5 summarizes and reflects the dissertation's findings and gives an outlook onto yet-unanswered research questions, some of which have been newly formed by this work.

2. Influence of Sensor Noise on Inertial Navigation

Within this chapter, sensor noise influences on the accuracy of purely inertial navigation are presented. While the underlying theory has been described in literature before [30] [50] [59] [60] [61], it is summarized here in a more complete form. As an exemplary use-case, an emergency stop maneuver of an automated driving system is modeled within a 3D-environment. Iterative simulations assess the impact of single and combined noise sources of accelerometers and gyroscopes on the final position deviation. Other errors of inertial sensors, particularly systematic ones, are not taken into consideration, because the focus here is solely on noise influences. The results shown are therefore not representative of the worst-case performance of MEMS inertial sensors, but rather of a *lower bound*, which cannot be circumvented save for improving the noise characteristics of the sensor. In later practice, inertial sensor data might very well be combined with wheel speed read-out [30] or other information from still-functional exteroceptive sensors during an emergency stop maneuver. In order to preserve generality, these are not considered here and a complete automated driving system failure except for the inertial sensors is assumed.

2.1. Theory

In the following, typical measures for noise in inertial sensors are presented, as well as theory on an Euler-angle strap-down mechanism which generates position data from specific force and angular rate input.

2.1.1. Noise Characteristics

Any physical sensing read-out is inevitably accompanied by noise. For accelerometer and gyroscope data, the root Allan variance (RAV), or Allan deviation (AD), has become the standard measure for separating and quantifying different noise components [46] [50] [61] [62] [63] [64] [65]. The Allan deviation is a time-domain method useful mostly for long-term stability analyses. Its frequency-domain pendant is the power spectral density (PSD), which gives a poor representation of effects with long time constants. It is however much better suited for disambiguation of short-term and oscillatory effects compared to the Allan deviation. A holistic analysis of inertial sensor data therefore always includes the Allan

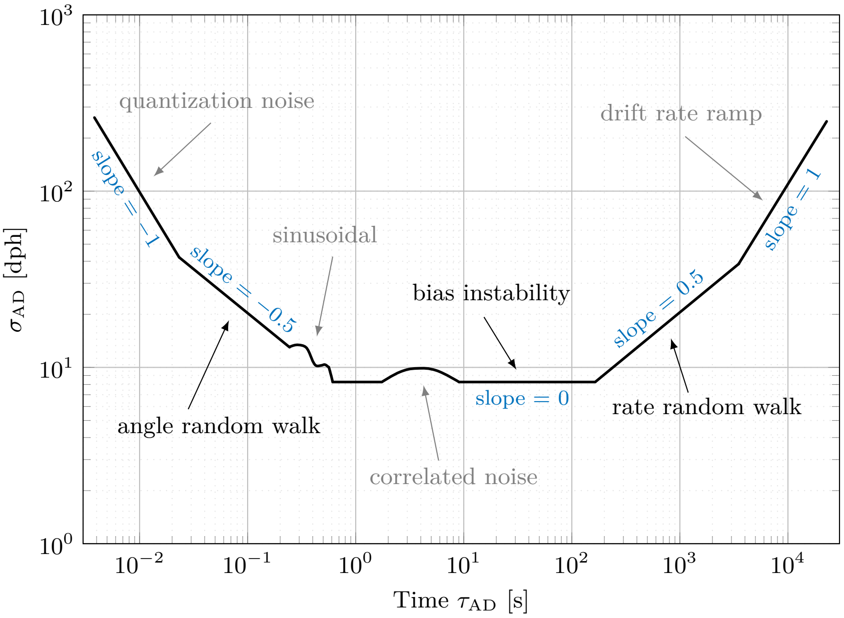

Figure 2.1.: Prototypical Allan deviation plot with noise slopes [61].

deviation *and* the power spectral density, based on the same dataset [66]. Allan deviation analysis aims to characterize the sensor-internal, stochastic signal components, which constitute a lower bound for performance, as explained above. It is therefore crucial, that data generation for Allan deviation analysis occurs at ideal, undisturbed conditions. In practice, this includes measuring the sensor at rest for at least 24 hours, ideally in a window-less laboratory with continuously-operating air conditioning. Vibration, loud sounds, temperature changes or power supply perturbations are to be avoided as best as possible.

Figure 2.1 shows the basic appearance of an Allan deviation plot. The IEEE standard [61] contains a number of additional and supernumerary definitions, which were reduced to the most important ones in this work. Allan deviation is calculated as a single number in the same physical units as the original signal

Table 2.1.: Noise components in an angular rate Allan deviation plot [50].

AD component	**Abbrv.**	**Slope**	**Coeff.**	$S_{\mathrm{PSD}}(f)$	**“Color”**
Quantization noise	QNT	-1	Q_z	f	blue
Angle random walk	ARW	-0.5	Q	1	white
Bias instability	BIS	0	B	$1/f$	pink
Rate random walk	RRW	0.5	K	$1/f^2$	red/brown
Drift rate ramp	DRR	1	R	$1/f^3$	-

for each cluster time τ_{AD}. The entire dataset is separated into as many clusters as possible with length of τ_{AD}. The Allan deviation is defined as the (standard) deviation of the differences of the means of each cluster [50]. The V-shape of the Allan deviation appears, because most sensors will have noise characteristics, in which longer measurements lead to a higher precision of the actual signal value up to a certain, lowest point. Eventually, long-term drift effects will prevail, measuring longer will not lead to more information about the true signal value and Allan deviation in return rises again.

Noise types differ in the Allan deviation just as in the power spectral density S_{PSD} by their slope or rather by their dependence on frequency f and cluster time τ_{AD}, respectively. The components in Figure 2.1 are detailed in Table 2.1. The noise types have been attributed colloquial color descriptions. There is however no connection to actual color appearances or light spectra. The three most important Allan deviation components, angle random walk, bias instability and rate random walk will be outlined in the following in detail. Not of relevance in this chapter - but partly visible in the experimental results later on - are the sinusoidal and correlated (or Markov [67]) components. Concerning the drift rate ramp, it was found that this is mostly the influence of temperature changes and therefore not noise, but a systematic effect that is to be reduced as much as possible when gathering the experimental data [50].

The exact Allan deviation calculation is defined in [50] [61] [64] [68]. In this work, a slightly more intuitive notation is chosen. A data set Ω of N measurement samples with uniform sample time T_s is separated into two subsequent clusters of n samples with cluster time $\tau_{\mathrm{AD}} = nT_s$, starting at sample k. The averages of the two groups are

$$\overline{\Omega}_k(n) = \frac{1}{n} \sum_{i=k}^{k+n-1} \Omega[i] \tag{2.1}$$

and

$$\overline{\Omega}_{k+n}(n) = \frac{1}{n} \sum_{i=k+n}^{k+2n-1} \Omega[i]. \tag{2.2}$$

Allan deviation σ_{AD} as a function of cluster time τ_{AD} is then defined as

$$\sigma^2_{\mathrm{AD}}(\tau_{\mathrm{AD}}) = \sigma^2_{\mathrm{AD}}(nT_s) = \frac{1}{2(N-2n)} \sum_{k=1}^{N-2n} \left(\overline{\Omega}_{k+n}(n) - \overline{\Omega}_k(n)\right)^2, \tag{2.3}$$

where $N - 2n$ is the maximum number that two sets of n can be shifted by one within N samples. Calculating the sum of the sums for every cluster size n makes this method quite inefficient. Alternatively, one can integrate the data set beforehand. If the data is angular rate, then one receives the angle θ

$$\theta = \int \Omega \, \mathrm{d}t. \tag{2.4}$$

The cluster averages can then much simpler be calculated with

$$\overline{\Omega}_k(n) = \frac{\theta[k+n] - \theta[k]}{nT_s} \tag{2.5}$$

and

$$\overline{\Omega}_{k+n}(n) = \frac{\theta[k+2n] - \theta[k+n]}{nT_s}. \tag{2.6}$$

Allan deviation becomes

$$\sigma^2_{\mathrm{AD}}(\tau_{\mathrm{AD}}) = \frac{1}{2\tau^2_{\mathrm{AD}}(N-2n)} \sum_{k=1}^{N-2n} \Big(\theta[k+2n] - 2\theta[k+n] + \theta[k]\Big)^2, \tag{2.7}$$

which is the form of the IEEE standard [61]. Similarly to overlapping when calculating spectra, the stepping trough *every* k will result in a smoothed depiction, but not in a more accurate estimate. Better estimates of σ_{AD} can only be reached by measuring longer data-sets. The increase in variance at large cluster times can be seen in the Allan deviation plots below. The numerous Allan plots in this work were for this reason, and to also save computational time, calculated in a non-overlapping manner, i.e. k has step-size of n. Using equation (2.7) without overlap, the Allan deviation even for week-long measurements with tens of millions of data points can be calculated in mere seconds.

The relationship between the *two-sided* power spectral density $S_{\mathrm{2PSD}}(f)$ and Allan deviation is given by [50] [69]

$$\sigma^2_{\mathrm{AD}}(\tau_{AD}) = 4 \int_0^\infty S_{\mathrm{2PSD}}(f) \frac{\sin^4(\pi f \tau_{\mathrm{AD}})}{(\pi f \tau_{\mathrm{AD}})} \, \mathrm{d}f. \tag{2.8}$$

The full derivation can be found in [69] [70]. Different noise types defined as a function of f in the frequency domain can be plugged into the above formula. Solving of the integral then prompts the corresponding Allan deviation as a function of τ_{AD} in the time domain. It is important to note, that the order of f (compare Table 2.1) has a non-unique relationship to the slope of Allan deviation. The timing community has therefore introduced the modified Allan deviation [64]. Since the non-unique noise types of order f^1 and f^2 usually do not appear in inertial sensors, the modified Allan deviation has had little relevance for the characterization of gyroscopes and accelerometers. Lastly, it shall be noted that all spectral density plots within this dissertation use Welch's estimate with Blackman windowing [71] [72].

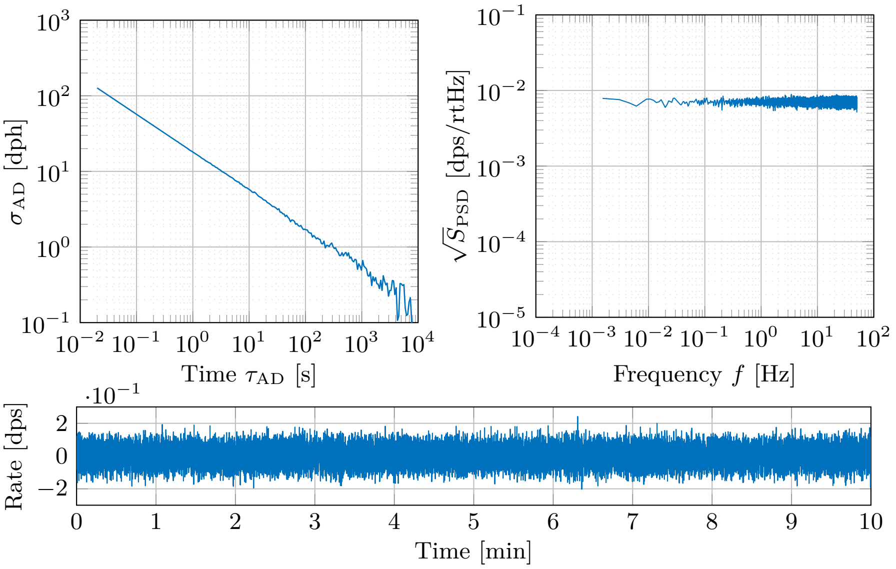

Figure 2.2.: Allan deviation (*left*), one-sided spectral density (*right*) and 10 min exemplary time series (*bottom*) of 10 h of simulated white noise sampled at 100 Hz, see [73] [74]. A typical magnitude of $Q = 5\,\mathrm{mdps/rtHz}$ is shown here.

Angle Random Walk

Angle random walk or white noise forms the largest contribution in MEMS gyroscopes and is what is generally understood as '*the* noise of a MEMS gyroscope'. Its sources and composition depend on the type and design of the gyroscope as well as its read-out electronics and control mechanisms [75] [76] [77]. As optimizing white noise of a MEMS gyroscope has been an objective since the inception of the technology, the sources are fairly well understood. Among them are electrical noise of the analog-to-digital converters (ADCs), digital-to-analog converters (DACs), quantization noise and effects of Brownian motion of gas molecules inside the device, which - contrary to their names - all produce white noise. White noise two-sided power spectral density is defined as [50]

$$S_{\mathrm{2PSD}}(f) = Q^2 \tag{2.9}$$

which results in an Allan deviation value of

$$\sigma_{\mathrm{ARW}} = \frac{Q}{\sqrt{\tau_{\mathrm{AD}}}}. \tag{2.10}$$

The angle random walk coefficient Q can therefore be found by reading off the Allan deviation value, or more precisely an appropriately fitted line, see Figure 2.5, at $\tau_{\mathrm{AD}} = 1\,\mathrm{s}$. There, and in Figure 2.2 above, Q equals $5\,\mathrm{mdps/rtHz}$. For accelerometers, this noise type is called *velocity* random walk (VRW) instead.

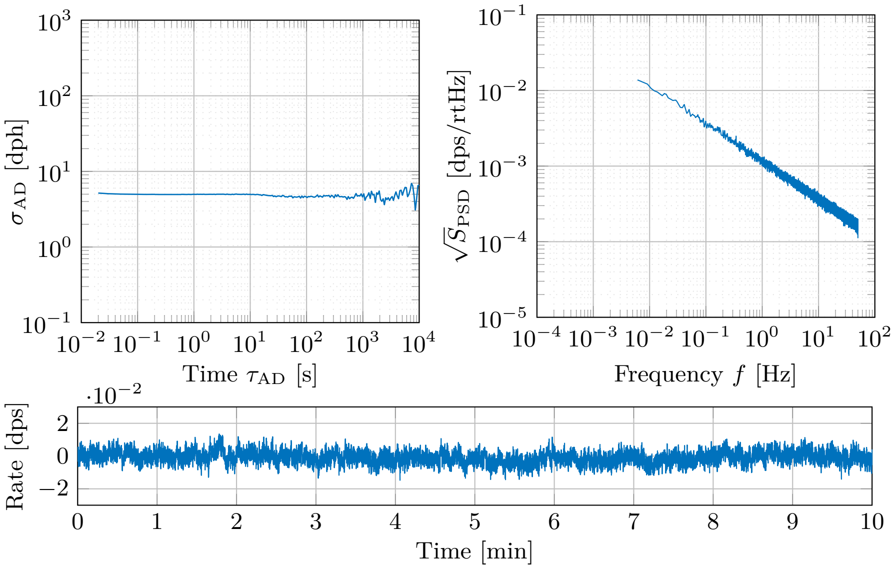

Figure 2.3.: Allan deviation (*left*), one-sided spectral density (*right*) and 10 min exemplary time series (*bottom*) of 10 h of simulated pink noise sampled at 100 Hz, see [73] [74]. A typical magnitude of $\sigma_{\mathrm{BIS}} = 5\,\mathrm{dph}$ is shown here.

Bias Instability

Bias instability or pink noise has a $1/f$ spectral characteristic [50]

$$S_{2\mathrm{PSD}}(f) = \frac{B^2}{2\pi f} \tag{2.11}$$

and is determined by a constant value in the Allan deviation plot

$$\sigma_{\mathrm{BIS}} = B\sqrt{2\ln(2)/\pi} \approx 0.664\,B. \tag{2.12}$$

Its time series plot has a more jagged look than white noise. Stationarity of the stochastic process has been debated in literature [78] [79] [80] [81]. Contrary to (rate) random walk, 1/f noise cannot be generated out of white noise by basic mathematical operations. In fact, a filter with an infinite number of poles and zeros would be necessary to shape white into perfect pink noise [78]. An easier way of generating high-quality pink noise is to fast Fourier transform (FFT) white noise into the frequency domain, shape the $1/f$ characteristic there, and bring the signal back to the time domain by inverse FFT, like in [82]. $1/f$ noise occurs in countless natural processes, oftentimes called flicker noise [83]. In the context at hand it appears in analog voltage generation and is thus the prime candidate for causing bias instability. Section A.2 in the appendix discusses physical sources and the relation between measurement time and variance.

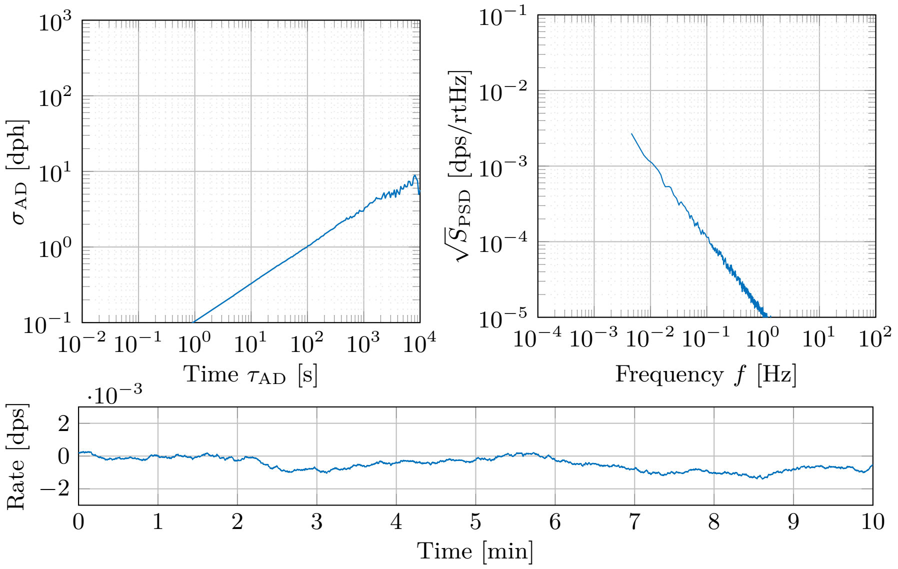

Figure 2.4.: Allan deviation (*left*), one-sided spectral density (*right*) and 10 min exemplary time series (*bottom*) of 10 h of simulated red noise sampled at 100 Hz, see [73] [74]. A larger-than-typical magnitude of $K = 50\,\mu$dps/rts is shown.

Rate Random Walk

The stochastic properties of rate random walk are much more intuitive than bias instability, as it can simply be generated by integration of white noise [60]. Such an integrating behavior might for example appear for high frequencies in an low-pass RC-network. However, our experiments, e.g. in Section 3.4, show that when proper care is taken to keep temperature changes small, there is only very little to no rate random walk present. Specifying rate random walk as a *stochastic* parameter is thus not advocated. It may however be useful for modeling systematic error effects that appeared in *one specific* measurement. One has to keep in mind however, that slow drifts will appear as drift rate ramp rather than rate random walk [50]. Typical reasons for offset drift are stress, temperature and humidity. Rate random walk is defined in spectral density as

$$S_{2\mathrm{PSD}}(f) = \frac{K^2}{(2\pi f)^2}. \tag{2.13}$$

Allan deviation then becomes

$$\sigma_{\mathrm{RRW}} = K\sqrt{\frac{\tau_{\mathrm{AD}}}{3}}. \tag{2.14}$$

If a line fit of rate random walk is extended to the left, the coefficient $K/\sqrt{3}$ can be read of at $\tau_{\mathrm{AD}} = 1$ s. In Figure 2.4, rate random walk is $K = 50\,\mu$dps/rts.

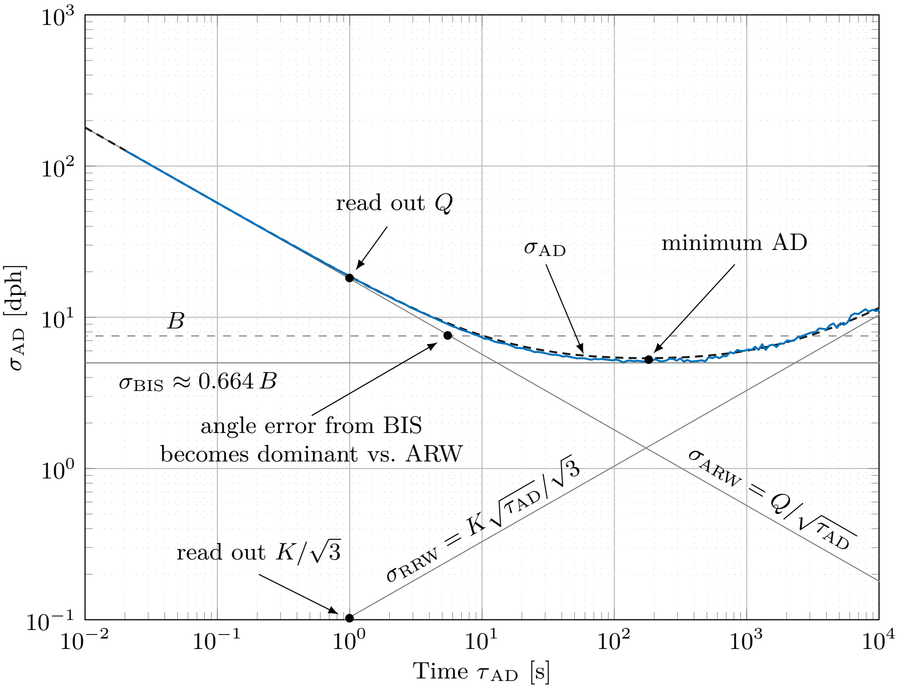

Figure 2.5.: All three major Allan deviation components with theoretical fit lines and combined curve of σ_{AD}. The noise levels Q, σ_{BIS} and K are the same as in the figures above, but the simulated data set was extended to 100 h for higher accuracy of the Allan deviation estimate at long cluster times.

Combined Noise

Like any other non-correlated, stochastic process, Allan deviation noise terms are added as the square root of the sum of squares

$$\sigma_{\mathrm{AD}}(\tau_{\mathrm{AD}}) = \sqrt{\sigma^2_{\mathrm{ARW}}(\tau_{\mathrm{AD}}) + \sigma^2_{\mathrm{BIS}}(\tau_{\mathrm{AD}}) + \sigma^2_{\mathrm{RRW}}(\tau_{\mathrm{AD}}) + \ldots}\ . \tag{2.15}$$

Figure 2.5 summarizes the basics of Allan deviation in a single plot where all three noise types from above were simulated for 100 h. The theoretical dashed curve of σ_{AD} aligns well with the simulation results in blue. The minimum of the Allan deviation curve is sometimes inaccurately called bias instability. For MEMS gyroscopes, that is not as much of an issue, as bias instability is typically a dominant component. The minimum and the true σ_{BIS} are then not far apart. While we do not call the sole coefficient B “bias instability” in this work, its level can be useful, when examining the influence of bias instability on the angle error after integration of the angular rate. The intersection of the angle random walk and the dashed “coefficient-B” line approximately marks the integration time after which bias instability becomes the dominant error [30]. The following pages will talk more about noise influence in integration.

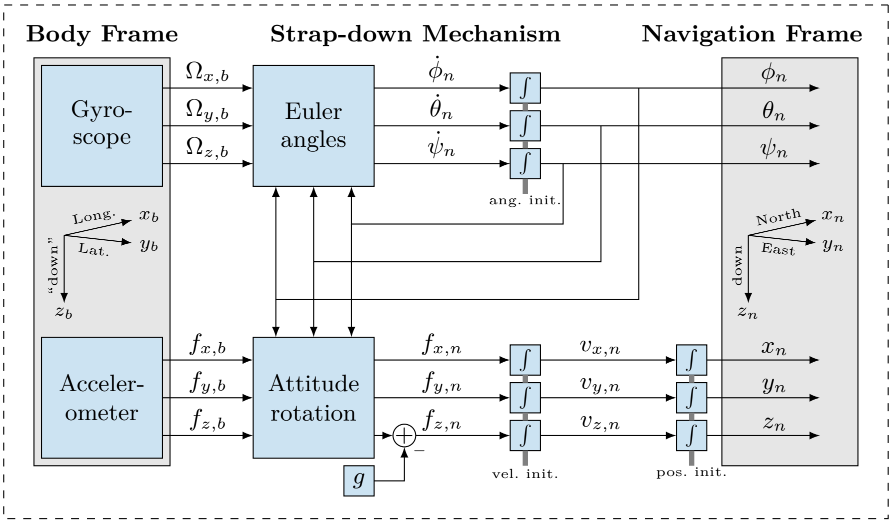

Figure 2.6.: An INS using a strap-down mechanism with Euler angle calculation and gravity compensation transforms inertial data measured in the vehicles body frame to position and attitude in the navigation frame [84] [85].

2.1.2. Strap-Down Mechanism

The main advantage of a strap-down configuration is, that the accelerometers can be placed directly onto the vehicle. No gimbals and therefore no moving parts outside of the actual sensors are necessary. However, the measured data must then be transformed from the vehicles body frame coordinate system to the outside world navigation frame coordinate system. The body frame b is defined here as a Cartesian, right-hand sided coordinate system with its origin in the center of mass. The x-axis points forward and the y-axis lies in the lateral plane of symmetry, pointing to the right. The perpendicular z-axis points "downwards" [86]. The roll, pitch and yaw rotations $\Omega_{x,b}$, $\Omega_{y,b}$ and $\Omega_{z,b}$ are defined around the x, y and z-axis.

For the (world) navigation frame coordinate system n, a Cartesian, right-hand sided North-East-down convention is used. Earth rotation and the resulting Coriolis acceleration is ignored here, since it is a systematic effect depending on driving direction. Also, navigation time is short and velocities are moderate, resulting in sub-cm position effects. Thus n is defined as an inertial reference frame, i.e. it does not move in relation to the fixed stars [84]. It is furthermore assumed, that the Earth's gravity vector is exactly $g = 9.81\,\mathrm{m/s^2}$ and remains constant at all positions during the maneuver. Euler angle calculations

$$\dot{\phi}_n = \left(\Omega_{y,b}\sin\phi_n + \Omega_{z,b}\cos\phi_n\right)\tan\theta_n + \Omega_{x,b} \tag{2.16}$$

$$\dot{\theta}_n = \Omega_{y,b}\cos\theta_n - \Omega_{z,b}\sin\theta_n \tag{2.17}$$

$$\dot{\psi}_n = \left(\Omega_{y,b}\sin\theta_n + \Omega_{z,b}\cos\theta_n\right)/\cos\theta_n \tag{2.18}$$

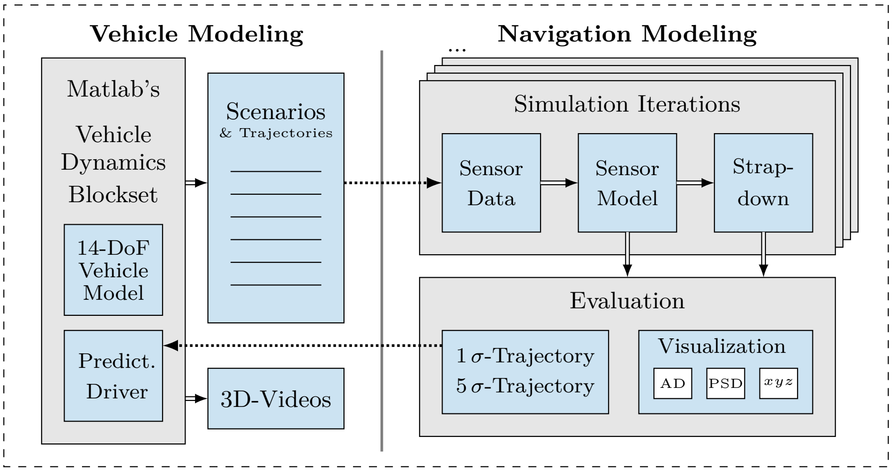

Figure 2.7.: The simulation structure includes slow and complex trajectory generation (*left*) and fast, efficient sensor noise and strap-down modeling (*right*).

are used to transform the measured angular rates from the body frame into the navigation frame [84]. Figure 2.6 shows the structure of a strap-down mechanism. A singularity appears when θ_n approaches ±90 deg which would be solved by using quaternions. Since road vehicles are modeled here, pitch will never be that high in a realistic use-case and the Euler angle calculation suffices. The navigation frame angular rates $\dot{\phi}_n$, $\dot{\theta}_n$ and $\dot{\psi}_n$ are integrated to attitude angles ϕ_n, θ_n and ψ_n, which are then used to rotate the specific force measurements f_b to the navigation frame as well. Now, gravity g can be subtracted from $f_{z,n}$ and double integration firstly yields velocity v_n and then positions x_n, y_n and z_n.

All nine individual integrators need to be primed with the correct initial-condition angles, velocities and positions. The initial-condition angles need to be particularly precise, because the subsequent double integration lets any error grow rapidly. Providing the initial-condition values is the responsibility of the automated driving system while it is still fully operational. Zero error in the initial conditions is assumed here.

2.2. Simulation

A simulation environment was set up within Matlab/Simulink where a vehicle, a six-axis inertial sensor and a strap-down mechanism were modeled. The structure is split in two as shown in Figure 2.7. First, a rather complex and therefore time-intensive, 14-degrees-of-freedom (DoF) vehicle simulation using Matlab's Vehicle Dynamics Blockset [87] generates driving trajectories for different scenarios. Two of the scenarios will be detailed below. In a second step, one trajectory is loaded into the navigation model, which is much more efficient and therefore allows to run hundreds of iterations in reasonable time. Each iteration adds random

Figure 2.8.: 3D-visualization using Matlab/Simulink's Vehicle Dynamics Blockset. *Left:* Two overlayed vehicles at the start of the emergency stop maneuver. *Right:* After 20 s, the blue vehicle possessing a more accurate inertial sensor comes to a halt on the road shoulder, while the silver vehicle stops halfway on the road due to the worse performance parameters of its inertial sensor.

and independent noise of predefined intensity to the ground-truth trajectory. After all iterations have been simulated, the results are visualized. Furthermore, 1 and 5 σ-error trajectories that were caused by the sensor noise are calculated. In a third step, these can be supplied back to the Vehicle Dynamics Blockset for generation of overlay videos which compare the ideal path and the trajectory disturbed by sensor noise in a 3D-environment, see Figure 2.8.

2.2.1. Vehicle Model

The Vehicle Dynamics Blockset offers very complex vehicle models, including the vehicle body kinematics, powertrain, steering, wheels, tires and suspension [87]. For the trajectory generation, the default parametrization of the double lane change [88] and increasing steering [89] examples was used and adjusted where necessary. Since the details of the vehicle modeling are not entirely relevant for the topic at hand, they are omitted here. Of more importance is, that the generated trajectories represent reasonably realistic vehicle behavior.

2.2.2. Sensor Model

The iteration simulation includes a MEMS inertial sensor with three accelerometers and gyroscopes. The ground-truth angular rates, forces and gravity in the body frame are loaded from the Vehicle Dynamics Blockset simulation. Since gravity and all of the other forces are provided separately, the iteration simulation offers the possibility to turn off gravity in order to examine the influence of all non-gravity related effects. The inertial sensor and strap-down is sampled at 200 Hz, which therefore allows for a bandwidth maximum of 100 Hz. This is considered adequate for vehicle dynamics [29]. Angle random walk Ω_{ARW} and bias instability Ω_{BIS} of predefined intensities Q and $0.664B$ are

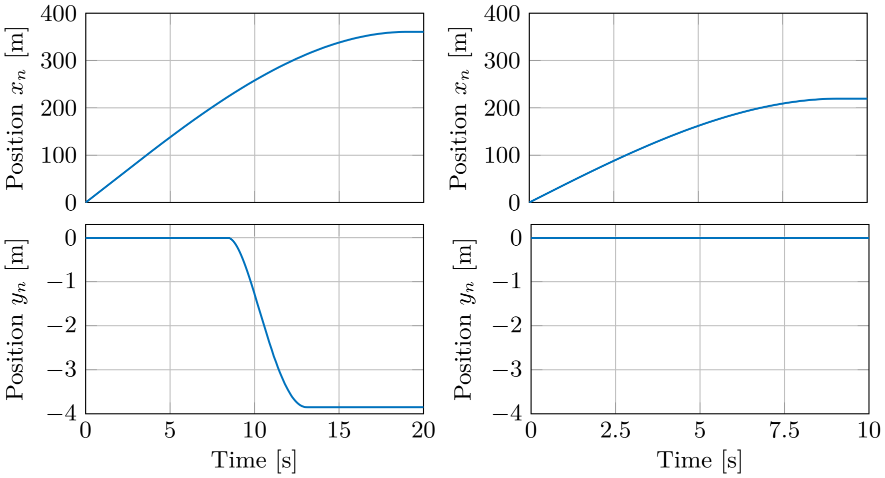

Figure 2.9.: Vehicle position during conservative emergency stop maneuver with 20 s of moderate deceleration and shift to the road shoulder (*left*) and aggressive emergency stop with 10 s of hard braking and stop in-lane (*right*).

added to the ground-truth angular rate signal $\Omega_{\mathrm{b,true}}$ for each individual axis and analogously to the specific forces according to Table 2.2.

$$\Omega_{x,b} = \Omega_{x,b,\mathrm{true}} + \Omega_{x,\mathrm{ARW}} + \Omega_{x,\mathrm{BIS}} \tag{2.19}$$

$$f_{x,b} = f_{x,b,\mathrm{true}} + f_{x,\mathrm{VRW}} + f_{x,\mathrm{BIS}} \tag{2.20}$$

For each iteration and axis, an independent noise vector of 9 min length is generated. Thereof, the actual 10 or 20 s portion for the simulation is picked and subjected to a subtraction of the mean of the previous 3 min. This approach mimics the preceding phase of the purely inertial navigation, where availability of the exteroceptive sensor is assumed to be optimal and where the inertial sensor offsets can be ideally estimated. As discussed above, rate random walk is not deemed to have a significant impact on these time scales and is therefore omitted here. The simulation includes a signal-pane, where the Allan deviation and spectral densities of the added noise can be checked for correctness. Further effects may have considerable influence on the final position but are omitted for this analysis. Nonetheless the simulation would allow simple modeling of e.g. temperature drifts, offsets, sinusoidal tones, vibration disturbances, misalignment, cross-axis sensitivity or gravity-dependence of the gyroscopes.

2.2.3. Trajectory Models

A total of ten scenarios were created, two of which are presented here. Both scenarios are modeled on a level and straight highway road. The vehicle is assumed to point northwards at $t = 0\,\mathrm{s}$, i.e. axes x_n, y_n and x_b, y_b are approximately parallel. Each path is iterated in the simulation 3000 times with randomly generated noise of identical intensity, producing reliable $1\,\sigma$ error paths. A first, conservative scenario assumes that e.g. some radar function for collision braking is still active and that the minimal risk condition would be fulfilled by driving to the road shoulder with moderate deceleration over the course of 20 s. An initial speed of 100 kmph is modeled. Since the integration time is longer, this scenario will make higher demands on the noise level of the inertial sensors. The second scenario assumes the outage of all safety systems and thus comprises a more aggressive maneuver with rapid braking and stopping in the current lane within just 10 s. The initial speed is set to 130 kmph which results in a quite hefty, average deceleration of about $3.6\,\mathrm{m/s^2}$. Figure 2.9 displays the two scenarios. More detailed plots of angles, velocities and positions are shown in Section A.5 of the appendix, together with the results from the iteration simulation.

2.3. Results

2.3.1. Analytic Description

It was established above, that *gyroscope* non-idealities typically have dominant influence on the final position due to the triple integration [30]. Therefore, the analytical description of only the gyroscope influence will be given here. For an analysis of accelerometer noise effects, the reader is referred to [59]. The angle standard deviation after single integration of an angular rate signal with angle random walk and bias instability, respectively, is [30] [90]

$$\sigma_{\phi/\theta/\psi,\mathrm{ARW}} = Q\sqrt{t} \qquad \text{and} \qquad \sigma_{\phi/\theta/\psi,\mathrm{BIS}} \approx Bt. \tag{2.21}$$

An extensive discussion about the validity and nature of the formula for integrated bias instability is given in Section A.2 of the appendix, because it has not been provided elsewhere yet. Based on equation (2.21) the intersection point of σ_{ARW} and the B-level determines approximately at which integration time bias instability becomes dominant versus angle random walk as shown in Figure 2.5. A simulation of 100 integration iterations shows the comparison of the numerically determined $1\,\sigma$ standard deviation with the analytical curve

Table 2.2.: Specified noise levels for the iteration simulations of both scenarios.

Sensor Noise	$\Omega_{x,b}$	$\Omega_{y,b}$	$\Omega_{z,b}$	$f_{x,b}$	$f_{y,b}$	$f_{x,b}$	**Units**
Angle random walk	5	5	5	-	-	-	mdps/rtHz
Bias instability	5	5	5	-	-	-	dph
Velocity random walk	-	-	-	200	200	200	μg/rtHz
Bias instability	-	-	-	50	50	50	μg

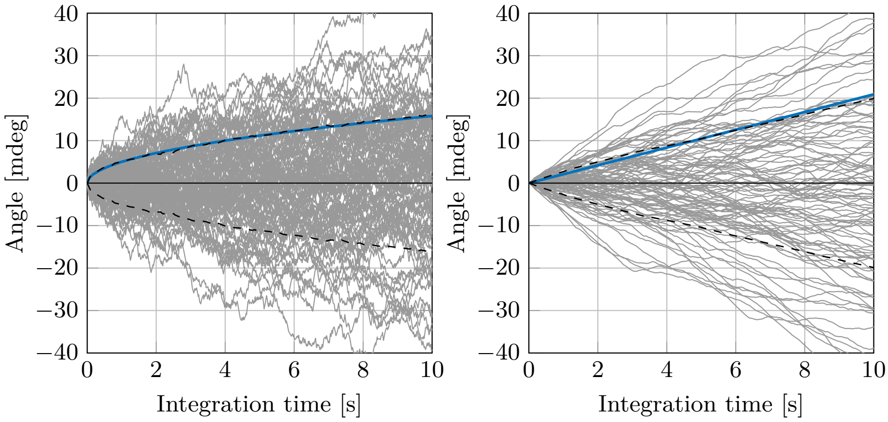

Figure 2.10.: One hundred iterations (*gray*) of integrated white noise (*left*) and pink noise (*right*) with averaged $1\,\sigma$ standard deviation (*black, dashed*), true zero-error (*black, solid*) and analytical curve (*blue*). Note the $\sqrt{t}$ and t dependencies. The noise intensities were $Q = 5\,\mathrm{mdps/rtHz}$ and $0.664B = 5\,\mathrm{dph}$.

in Figure 2.10. Note, that angle-errors due to noise are nominally zero-mean. Figure 2.11 exhibits angle error curves for exemplary bias instability and angle random walk values. If it is assumed that bias instability noise behaves like a constant offset, its influence on position error can be determined by simply integrating equation 2.21 twice, under assumptions that error angles are small ($\sin(\alpha) \approx \alpha$). It is furthermore presumed that a significant error only occurs in the x_n and y_n axis because z_b and z_n are approximately parallel. Gravity is thus almost only measured in $f_{z,b}$. All other non-gravity accelerations are investigated by simulation in the next section. Position error due to gyroscope bias instability and gravity then becomes

$$\sigma_{x/y,\mathrm{BIS}}(t) \approx B\frac{t^3}{6} \cdot \frac{\pi}{180}\, 9.81 \Big[\frac{\mathrm{rad}}{\mathrm{deg}}\frac{\mathrm{m}}{\mathrm{s}^2}\Big]. \tag{2.22}$$

The analoguous triple-integration relationship for angle random walk is derived in section A.1 of the appendix. One receives

$$\begin{aligned}\sigma_{x/y,\mathrm{ARW}}(t) &= Q\sqrt{\frac{t^5}{20} + \frac{\tau_0 t^4}{4} + \frac{5\tau_0^2 t^3}{12} + \frac{\tau_0^3 t^2}{4} + \frac{\tau_0^4 t}{30}} \cdot \frac{\pi}{180}\, 9.81 \Big[\frac{\mathrm{rad}}{\mathrm{deg}}\frac{\mathrm{m}}{\mathrm{s}^2}\Big] \\ &\approx Q\sqrt{\frac{t^5}{20}} \cdot \frac{\pi}{180}\, 9.81 \Big[\frac{\mathrm{rad}}{\mathrm{deg}}\frac{\mathrm{m}}{\mathrm{s}^2}\Big]. \end{aligned} \tag{2.23}$$

The angle or position errors are of course added as the square root of the sum of squares. Figure 2.12 reveals the rapid increase of error with time as well as curves of equal position error which can be used to determine trade-offs when designing an inertial measurement unit.

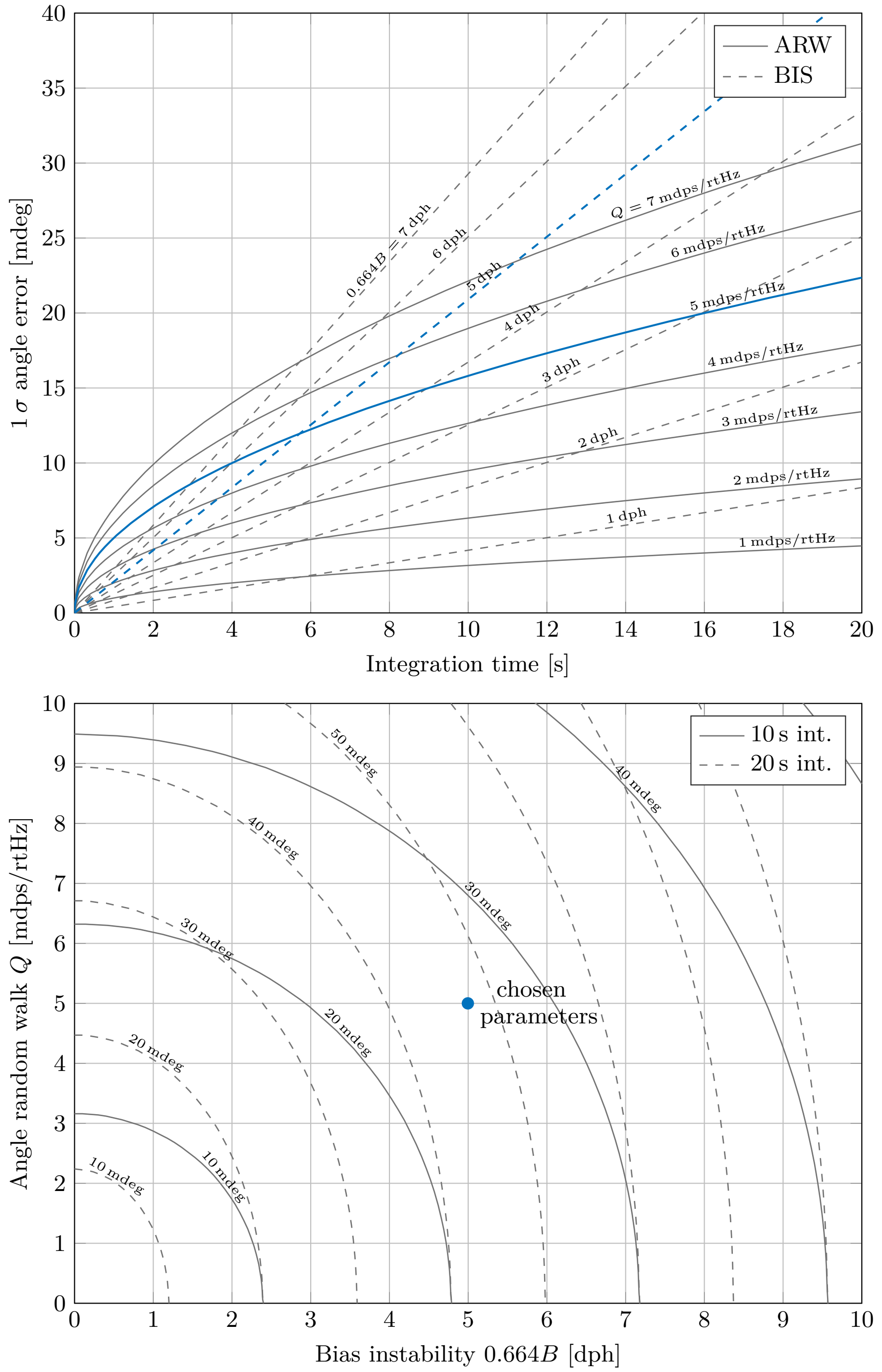

Figure 2.11.: *Top:* Analytical $1\,\sigma$ standard deviation of *angle* error after single integration for different values of angle random walk and bias instability during 20 s of integration time. *Bottom:* Lines of equal $1\,\sigma$ angle error as a combination of angle random walk and bias instability for 10 and 20 s of integration time. The error types are added as the square root of the sum of squares.

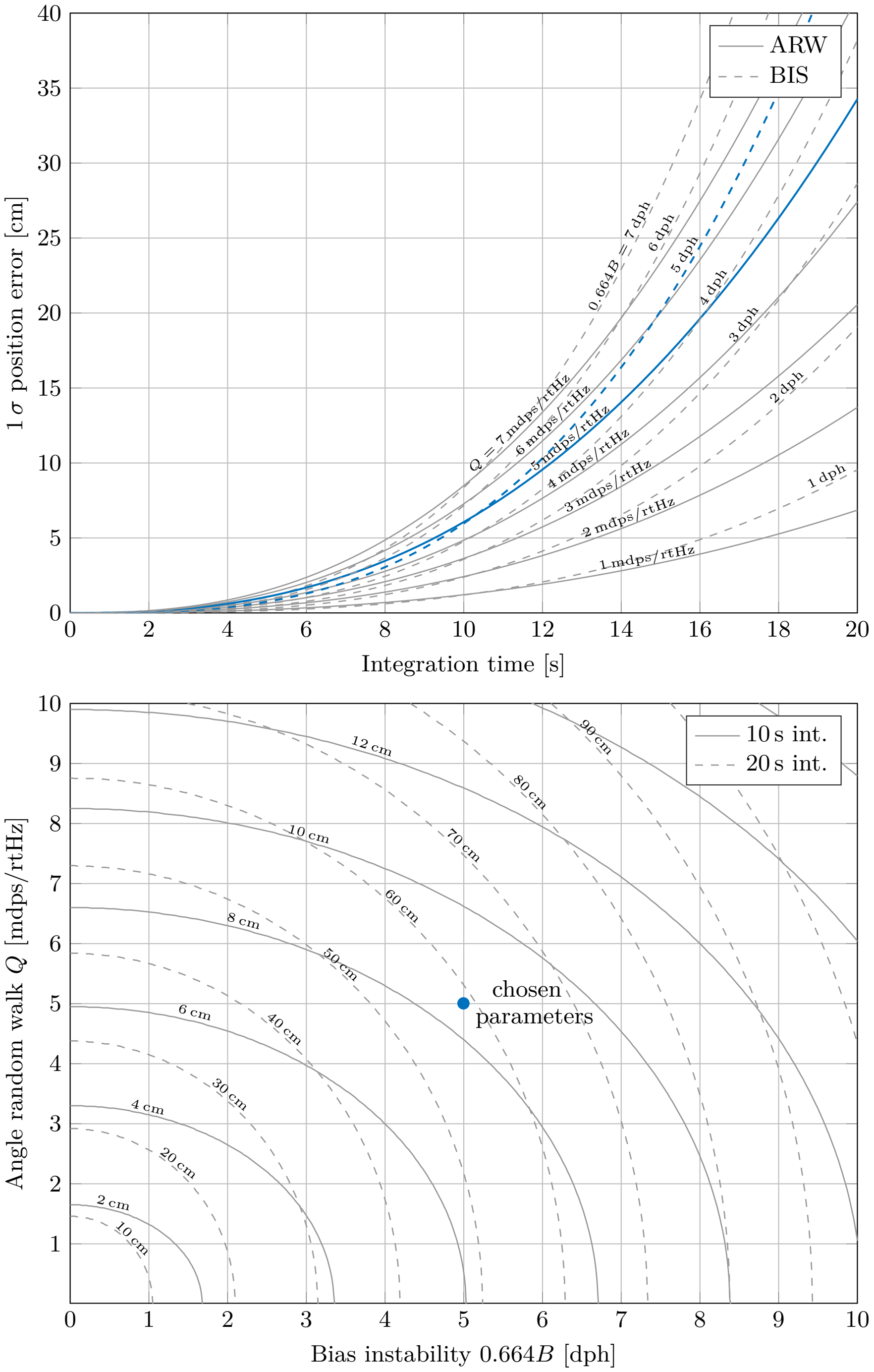

Figure 2.12.: *Top:* Analytical 1 σ standard deviation of *position* error solely due to gravity after triple integration for different values of angle random walk and bias instability. Note that e.g. 1 mdps/rtHz and 1 dph produce about the same position error at 10 seconds of integration. *Bottom:* Lines of equal 1 σ position error as a combination of angle random walk and bias instability for 10 and 20 s of integration time.

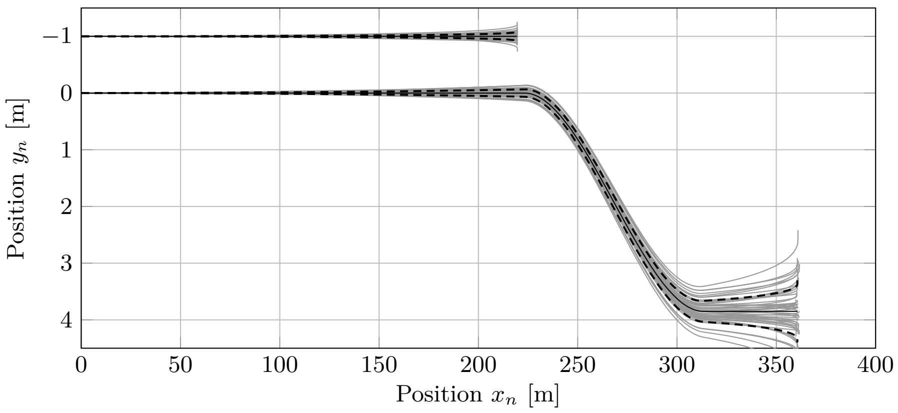

Figure 2.13.: Fifty simulation iterations of the aggressive in-lane emergency stop maneuver during 10 s (*top*) and the conservative scenario for 20 s (*bottom*) from the bird's eye view. The black, solid lines mark the ground truth without noise disturbance and the black, dashed lines the 1 σ lateral error.

A neat memory aid can also be seen in the Figure 2.12. If one uses typical units of mdps/rtHz for angle random walk and dph for bias instability, then the position error of identical figures of angle random walk and bias instability is roughly the same after 10 s of integration.

2.3.2. Simulation Outcome

The two emergency stop scenarios are simulated with the parameter set listed in Table 2.2, which represents realistic performance for MEMS inertial sensors. Figure 2.13 shows 50 iterations of both scenarios next to each other. As expected, the 20 s maneuver accumulates much larger errors. Figures 2.14 and 2.15 show the contributions of angle random walk and bias instability for each sensor axis on the total position error of each axis in the navigation frame. Gyroscope bias instability is the largest error contributor in the 20 s simulation and is approximately on par with angle random walk in the 10 s run. Gyroscope noise performance is limiting for both scenarios compared to the accelerometers in the x_n and y_n axes. For z_n, the accelerometers are dominant. Since the braking deceleration has smaller magnitudes than gravity in both scenarios, the error share from gyroscope-and-gravity effects is much larger than from any other driving-related accelerations.

Equations (2.22) and (2.23) therefore give a good, rough estimate of the final x_n and y_n position, which is also evident when comparing the simulation results with Figure 2.12. Minor deviations between simulation and analytical prediction are attributed to the following effects: Even though 3000 iterations where performed for each bar, some statistical uncertainty will remain. Also, the noise generation may not perfectly produce the specified level. For angle random

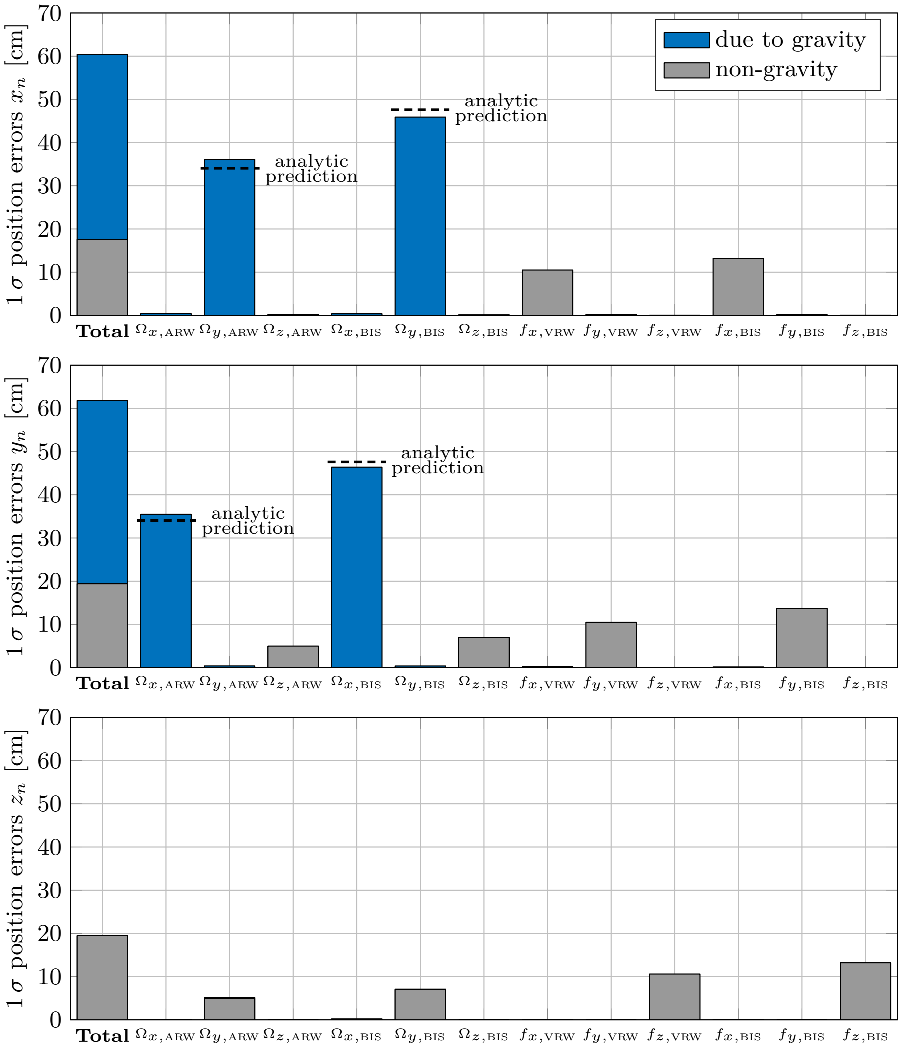

Figure 2.14.: Position error of each axis x_n (*top*), y_n (*middle*) and z_n (*bottom*) in the navigation frame due to angle random walk and bias instability of the gyroscope as well as velocity random walk and bias instability of the accelerometer. The 20 s conservative emergency stop scenario was simulated with 3000 iterations for each bar. Blue marks the share of gyroscope-and-gravity related errors and gray indicates all other errors. The black, dashed lines indicate the values predicted by equations (2.22) and (2.23).

walk, equation (2.23) describes the error if the offset would have been estimated for an infinitely long time before the navigation start. Since here a 3 min offset subtraction period was assumed, small additional errors appears. For bias instability, Section A.3 in the appendix discusses in detail how equation (2.22) gives merely a rough approximation. In actuality, the behavior of integrated bias instability depends on how low in frequency the 1/f property continues.

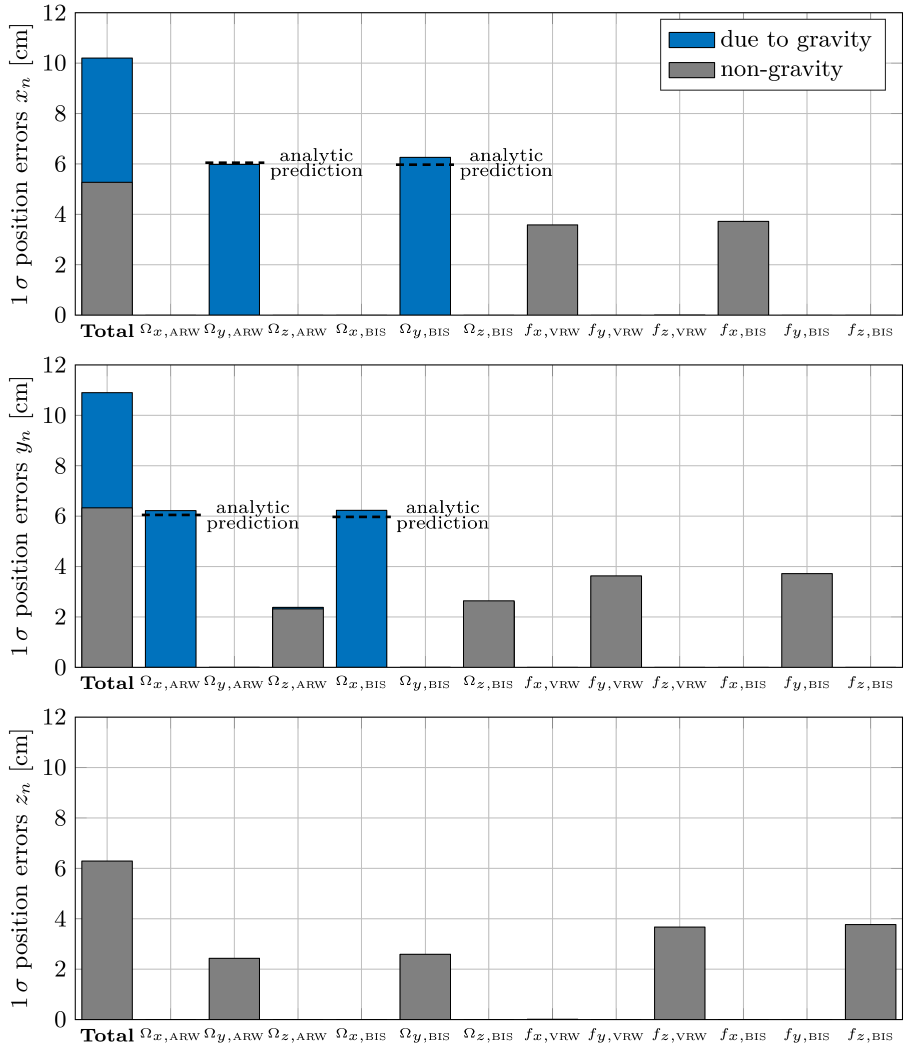

Figure 2.15.: Position error of each axis x_n (*top*), y_n (*middle*) and z_n (*bottom*) in the navigation frame due to angle random walk and bias instability of the gyroscope as well as velocity random walk and bias instability of the accelerometer. The 10 s aggressive emergency stop scenario was simulated with 3000 iterations for each bar. Blue marks the share of gyroscope-and-gravity related errors and gray indicates all other errors. The black, dashed lines indicate the values predicted by equations (2.22) and (2.23).

Since the total generated noise length for each iteration and sensor axis was 9 min, the influence of bias instability slightly surpasses the prediction for the 10 s scenario and falls below for the 20 s maneuver.

More figures of the simulation results are revealed in Section A.5 of the appendix. Since breaking happens in the longitudinal direction of the vehicle, the Ω_y gyroscope axis noise causes slightly more position error than the Ω_x

signal. It is of course important to remember, that the error distribution among the axes depends on the driving scenario and the final heading of the vehicle. The influence of Ω_z noise is barely relevant. This may however change into the opposite if e.g. wheel speed is included in the navigation algorithm and dead-reckoning using velocities is performed [30]. The accuracy of the Ω_z axis is also crucial in the correct estimation of the initial heading at the start of the purely inertial navigation. Particularly in the case of short time spans of exteroceptive sensor availably before the emergency stop maneuver, generating sufficiently accurate heading information is challenging [91].

As in this simulation, one has to decide in the real world how to best generate an offset error estimate before the purely inertial navigation starts. In the simplest case, the angular rate offset is determined by identifying phases where the sensor is at complete rest without external disturbances. Then, the Allan deviation provides the information on how long one should ideally average the signal to calculate the offset value and what uncertainty will fundamentally remain in that value [90]. If the duration for determination of the offset is shorter than what the Allan deviation minimum dictates, then the navigation accuracy is deteriorated by an additional linearly rising offset according to the ARW value of that duration, as described above.

This line of thought points to an important difference between the integral of angle random walk and that of bias instability. For angle random walk, equation (2.21) describes the standard deviation of the angle error exclusively for the noise occurring *within* the integration period. The reason is, that with an ideal reference and with long calibration time, the offset uncertainty of averaged angle random walk becomes very small. By contrast, bias instability noise fundamentally does not allow a better offset estimate at longer times. No matter how short or long the available averaging time, the uncertainty - by definition - is always the same. The angle error formula of bias instability does therefore not just include the error occurring due to the noise within the integration period, but also reflects the error prevailing in the calibration phase beforehand.

2.4. Discussion

In this chapter an introduction of inertial sensor noise and its characterization by Allan deviation was provided. It was demonstrated by analytical calculation and iteration simulations of an Euler angle strap-down mechanism that angle random walk and bias instability of the angular rates are the most influential noise parameters for purely inertial navigation for durations on the order of tens of seconds. It shall be reiterated here once again, that the results constitute a *lower bound* for inertial sensor performance and that other, deterministic influences like temperature, stress or external vibration may cause further and much greater deterioration. In an exemplary fashion, the influence of a linear offset drift due to temperature is shown in Section A.4 of the appendix. A typical specification parameter for MEMS gyroscopes is the temperature coefficient of the offset (TCO). Using common values for cheap, consumer-type devices and realistic temperature changes of 1 to 5 K over a duration of 20 s, temperature influence surpasses the stochastic influences of angle random walk and bias instability by far. If however TCO values in line with high-performance automotive sensors are used, the influence of temperature drift is lower than or on par with that of the noise errors.

When assuming typical noise performance of MEMS inertial sensor in this chapter, this lower bound alone is not low enough to make an emergency stop maneuver feasible. Using a rather lax 3-σ specification, the lateral position error would be 168 cm and 31 cm for the 20 s and 10 s trajectory, respectively. This much tolerance is deemed infeasible without touching other vehicles or e.g. the guard railing. MEMS gyroscope accuracy needs to be better than the typical performance examined in this chapter. A three-axial, automotive-grade MEMS research gyroscope with greatly reduced noise was therefore developed at Robert Bosch GmbH. These devices are taken as a benchmark for further improvement of bias instability levels, which will be the central theme of the next chapter.

In this chapter, the error propagation *during* the purely inertial navigation period was investigated. Of similar importance is good sensor performance at the time *before* the emergency stop maneuver [90] [91]. The better the sensor, the quicker the error estimator, e.g. Kalman filter, can calculate the deterministic errors. From a practical viewpoint, the driver will want to engage a fully automated driving feature quickly after starting their vehicle and not be forced to drive for long durations until all errors have been estimated sufficiently.

The feasibility of using *redundant* sensors to improve performance was evaluated by the author as a side topic. Results are briefly discussed in Section A.6 of the appendix. In summary, noise of one sensor, e.g. bias instability, is typically not correlated to another sensor. This leads to a maximum noise improvement of a factor of $\sqrt{N}$, where N is the number of identical sensors. The discussion section of the next chapter compares the achieved improvements with what could theoretically be attained with redundancy concepts.

3. Origins and Mechanisms of Bias Instability Noise

This chapter constitutes the central part of the dissertation. First, a literature review summarizes the current research on highly-precise MEMS gyroscopes. The most common zero-rate offset effects are subsequently recapitulated and an overview of the employed feedback control structures is given. Measurements on future-generation, three-axial, automotive-grade devices are combined with a detailed simulation model in order to explore the sources of the so-far unknown origins of bias instability. A further *scale-factor* instability effect is discovered and analytic predictions for both types of instabilities are derived.

3.1. State of the Art

This section provides a comprehensive overview of current findings related to offset stability of MEMS gyroscopes. Compared to the two introductory chapters, the terminology is now much more specialized and not all terms are introduced in this section for the sake of brevity. However, the theory section below contains detailed explanations of most of the terms and phenomena.

Vibrating mass MEMS gyroscopes measure angular rate by transferring energy proportionally to the applied angular rate from a constantly oscillating drive mode to a sense mode in perpendicular orientation via Coriolis force [92]. These two modes may either be separated in their natural frequency - oftentimes several kHz - or the modes may be matched [93]. The majority of MEMS gyroscopes, particularly of consumer-grade, are operated with split modes [93]. Since the transferred Coriolis force is proportional to the oscillating mass, see equation (3.1), miniaturization runs counter to a large measurement signal. This is exacerbated further by the fact, that micro-scale fabrication is less precise than conventional, macro-scale manufacturing when comparing the size of the smallest features to those of the accruing defects [38]. Increasing symmetry of the design is therefore generally beneficial, along with increasing the percentage of active mass per allowed device size. The authors of [94] reach near-navigation grade performance with a single-axis, quadruple-mass gyroscope with a huge $100\,\mu$m device layer thickness and $74\,\mathrm{mm}^2$ footprint. They report a bias instability of 0.09 dph and an angle random walk of 0.25 mdps/rtHz in a high-Q, mode-matched configuration. Due to the lack of force-rebalance [95], the bandwidth is most likely and rather impractically in the sub-Hz domain [96] and the scale factor is highly dependent on temperature [97]. The devices in this dissertation include *three* axes on a footprint smaller than 5 mm^2. Simple mass or size increase is not compatible with customer demands and the price goal. Since fabrication technology has by now reached a certain maturity [98], improving offset stability is oftentimes attempted by algorithm- and control-based approaches. Two distinct areas of active research were identified. The first field includes approaches that employ mode reversal, the second makes use of either already known sensor-internal signals or measuring or estimating them or actively injecting additional test-signals to extract information about error effects like quadrature, temperature or mechanical stress.

A major source of offset is the unwanted leakage of energy from the drive to the sense mode by other means than Coriolis force [99], e.g. due to mechanical manufacturing imperfections. The basic idea behind mode reversal is the rejection of common mode error effects [100] by either continuously switching the drive and sense mode [101] or by driving both modes and reading out the phase difference [102]. The advantage of the latter is, that incredibly high angular rates - up to hundreds of thousands of dps - can be measured with high bandwidth [96] and great temperature stability, which makes them attractive for defense applications. However, these so-called rate-integrating, whole-angle or frequency-modulation gyroscopes [95] [103] often cannot detect small rates [104] [105]. “Virtual” rotation was shown to aid in overcoming this disadvantage [105] and was furthermore employed to estimate scale factor changes [106]. Rate-integrating gyroscope design is in most cases axis- or at least mode-symmetric [107], which is difficult to realize for out-of-plane sensing, i.e. x- and y-axis gyroscopes. The first three-axial frequency-modulated gyroscope has been published only very recently [108]. For in-plane sensing gyroscopes however, significant offset stability improvement has been achieved [109]. A mode-reversal technique improved bias instability from 9 dph in the regular rate mode to 1.7 dph, however at the cost of more than thrice the angle random walk [110]. Additional control loops for damping mismatch and quadrature were implemented with moderate experimental success in [111]. In an early control-based approach, a self-calibrating dual-stage control for rate-integrating gyroscopes was demonstrated in simulation [112]. Later contributions of this research group include a rate-integrating gyroscope realized on the above mentioned quadruple-mass device with bias instability of 0.5 dph and angle random walk of 1.4 mdps/rtHz, which was shown to be worse in terms of noise performance compared to the conventional, rate-measuring operation of one and the same device [113]. The finding is contrasted by [114] [115], wherein a much smaller 4 mm^2, 2.6 MHz bulk acoustic wave gyroscope had improved angle random walk and bias instability performance - from 26 to 5 dph - when using the whole-angle mode together with automatic mode-matching. Summarizing it can be said that rate-integrating gyroscopes may reach excellent performance and are well-suited for niche applications, where extremely high angular rates need to be measured. Nonetheless, the conventional rate measuring configuration is better suited for the majority of commercial applications [113], especially automotive. Furthermore, modern three-axial MEMS gyroscopes only have a single drive control loop that excites movement of all three drive modes. Introducing separate drives to enable rate-integrating operation would complicate the system and raise costs due the additionally necessary connection pads. The rate-integrating approach is therefore not pursued further in this dissertation.

As mentioned above, mode-matched MEMS gyroscopes are mostly operated in a closed-loop configuration, also called force-rebalance, force-to-rebalance or force-feedback, in order to allow high quality factors *and* practical bandwidths [28] [116] [117] [118]. Herein, movement of the sense mode is suppressed by feedback control and the modulated angular rate signal is retrieved from the control output [95] [119]. Around this high-dynamic force-feedback loop, a slower quadrature compensation loop may be placed [28] [120] [121]. Quadrature is unwanted, direct movement stimulation from drive to sense which has 90 deg phase difference to the Coriolis angular rate signal, hence the name. Our group published a fully commercialized automotive MEMS gyroscope with force-feedback and 1.4 dph bias instability in 2007 [29]. Later designs presented single-bit $\Delta\Sigma$ force-feedback and quadrature compensation which resulted in similar bias instability levels [28]. Northrop Grumman LITEF showed a prototypical device with both force-feedback and quadrature compensation reach 0.1 dph in 2008. In the same year Georgia Tech published a sub-2 mm^2, mode-matched but open-loop device with 0.15 dph bias instability [122]. Quadrature cancellation improved a 7 dph device to 0.9 dph in [123] [124] along with tenfold angle random walk betterment. The already mentioned quadruple-mass gyroscope in force-feedback and quadrature compensation mode reached bias instabilities of 0.2 dph [125] [126]. Instead of actively compensating the quadrature in the system, a passive method that injected charges into the readout in opposition to the charges produced by quadrature was proposed and 1.3 dph of bias instability was measured [127]. Utilizing correlations of the quadrature signal to the rate output drift again on the quadruple-mass gyroscope improved temperature ramp and rate random walk [128] [129] [130]. The same contribution as well as others employed correlation to temperature, which was termed self-sensing as temperature was not measured with a dedicated sensor but via change of the drive resonance frequency [131] [132]. Since most modern MEMS inertial sensors do have a dedicated temperature sensor and high-performance systems need to be calibrated across their entire temperature range in any case, the temperature self-sensing approach may be somewhat superfluous. On-chip stress sensors removed rate random walk and temperature ramp portions in [133] [134].

Mode-reversal without whole-angle configuration was demonstrated in [135], where merely the polarity of the drive movement was alternated, see also [136] [137] [138]. Three-fold bias instability improvement to 5 dph came along with a trade-off of three-fold decrease of angle random walk. The authors therefore suggested to combine two gyroscopes, one regularly operated and one with the proposed method, or to fuse permanent readout during alternation of the drive polarity with readout at certain epochs [139]. An in-run scale-factor estimation was demonstrated with a similar technique of injecting a switching signal into the drive dynamics, resulting in 3 dph bias instability [140].

It has been revealed in recent years, that continuously controlling the mode-matching between drive and sense in-run improves bias instability [93] [141], which in turn indicates that slow, uncontrolled relative drift between the resonance frequencies of drive and sense is related to bias instability. The effects of detuning on white noise levels was covered in [75] [142], but bias instability noise was not included. A quadrature dither signal outside the angular rate bandwidth was used to measure detuning and improve bias instability from 6.5 to 0.2 dph [143] by controlling the frequency tuning voltage and thus the detuning. In contrast, no injected signal was necessary in [116] and frequency detuning information was gathered solely from noise observations. A 0.9 dph bias instability was achieved. A more comprehensive state-of-the-art on frequency detuning measures is provided in Chapter 4.

In summary, excellent bias instability performance has been demonstrated for numerous MEMS devices with a variety of different operating schemes. Particularly continuous mode-matching is deemed promising and therefore pursued further in this dissertation. All presented methods however fall short of truly examining the origins of bias instability and to address its 1/f noise nature, which is different from the slow temperature- and stress-related drifts that were improved in many works. With very few exceptions like [144], almost the entire literature examined in-plane sensing (z-axis) gyroscopes. This dissertation will expand the bias instability analysis to all three axes. It can also be observed, that large, prototypical devices tend to give better results than commercialized gyroscopes, which are driven by low-power ASICs only as opposed to operation by large, table-top lab equipment. The noise performance especially of the ASIC digital-to-analog converters will therefore be tackled as well. Table 3.1 compares the most prominent scientific contributions focusing on MEMS gyroscope bias instability improvement. The table also shows, that most - but not all - of the sub-1-dph gyroscopes were the large quadruple mass (74 mm^2 area) device from Prof. Shkel's group at UC Irvine.

Recently, Honeywell published a gyroscope with 0.06 mdps/rtHz angle random walk and bias instability as low as 0.02 dph [145] [146]. The offset stability over the entire temperature range was 0.2 dph. Their devices are operated mode-split in open-loop configuration. Among the reasons for reaching such phenomenal values, they list an increased size and thickness of the device and the supporting laboratory electronics (i.e. no ASICs) which were placed mostly outside the testing chamber and connected via long cables. Their target application is gyroscopic North-finding, compare [147]. Another research group using a 30 mm^2 area, 80 μm height, mode-split gyroscope reached bias instability values of 0.5 dph down to 0.08 dph, depending on the power intake of the read-out electronics [117] [148]. Employing a mode-matched, closed-loop design, Honeywell's competitor Northrop Grumman LITEF also recently published values as low as 0.01 dph, for in-plane axis gyroscopes [118]. Although not much about the actual mechanisms of improvement was revealed in their publication, optimizations in the read-out control loops were deemed instrumental. The push for better bias instability values in these high-end, defense and aeronautic applications further emphasizes the importance of bias instability as a valid performance parameter for MEMS gyroscopes, see also [149].

Table 3.1.: Prominent scientific contributions on the topic of bias instability improvement of mode-matched, in-plane sensing (z-axis) MEMS gyroscopes. Abbreviations are: Force-feedback (FFB), quadrature compensation (QC), open-loop (OL), rate-integrating gyroscope (RIG), bulk-acoustic wave (BAW), automatic mode-matching (AMM).

Architecture	**Ref.**	**Area**	**Height**	**BW**	**Range**	**ARW**	**BIS**
Units		[mm^2]	[μm]	[Hz]	[dps]	[mdps/rtHz]	[dph]
FFB, QC	[118]	n/a	n/a	240	499	0.2	0.01
OL	[94]	74	100	low	high	0.25	0.09
OL	[113]	74	100	low	300	1.0	0.1
OL, QC	[128]	74	100	low	high	0.3	0.1
FFB, QC	[34]	n/a	50	500	1000	5.0	0.12
OL, RIG	[122]	2	60	1-10	20	0.05	0.15
FFB, QC, AMM	[143]	4	n/a	high	n/a	4.2	0.2
FFB	[126]	74	100	100	100	0.8	0.2
FFB	[107]	74	100	200	1350	0.3	0.2
OL, RIG	[103]	74	100	high	18000	1.1	0.22
FFB, QC	[123]	2.2	n/a	n/a	100	0.23	0.4
OL, RIG	[113]	74	100	high	18000	1.4	0.5
FFB	[130]	n/a	n/a	n/a	n/a	0.6	0.8
FFB, QC, AMM	[141]	n/a	n/a	100	n/a	0.11	0.84
FFB, QC, AMM	[116]	n/a	n/a	med.	n/a	1.4	0.9
FFB, QC	[124]	n/a	n/a	high	high	0.6	0.91
FFB, QC	[28]	n/a	20	630	80	2.7	1.2
FFB, QC	[29]	n/a	n/a	60	187	2.5	1.3
OL, QC	[127]	1450	500	high	high	3.3	1.3
OL, RIG	[110]	13	n/a	n/a	n/a	26.6	1.7
FFB	[130]	2.6	n/a	n/a	100	5.3	3
FFB, QC, AMM	[93]	n/a	n/a	high	n/a	55	4
BAW, RIG	[115]	4	n/a	36	3000	11.6	5.4
OL, mode-rev.	[135]	7.8	n/a	125	300	14	6
OL, QC	[92]	n/a	n/a	n/a	30	6	7.1
FFB	[110]	13	n/a	n/a	n/a	7.2	9.2

3.2. Theory

The linear dynamics of Coriolis vibratory gyroscope have been covered many times before, for example in [32] [92] [95] [150] [151] [152]. Therefore, only a brief overview will be given here before non-idealities are addressed. Coriolis force F_{cor} appears on an object with mass m and velocity v as a fictitious force during rotation Ω_{r} of a reference frame when viewed from that reference frame

$$\vec{F}_{\mathrm{cor}} = -2m\,\vec{\Omega}_{\mathrm{r}} \times \vec{v}. \tag{3.1}$$

Figure 3.1 shows a mechanical model of a Coriolis vibratory gyroscope. In this example, the drive movement actuated by F_{dr} occurs in the x direction. Ideally, the only energy transfer to the vertical sense mode is that of Coriolis force and the modes are otherwise independent. Coriolis force is counteracted by the sense feedback control force F_{sn}. Although other physical principles like magnetic or piezoelectric drives are possible, capacitive actuation and read-out is the most widely used method for MEMS inertial sensors, e.g. [153] [154] [155]. A single drive frame movement is excited and read out in the in-plane direction for all three sense modes by interdigitated comb drives. Although the drive frame is excited in-plane, its intricate design includes drive modes that vibrate in a rotating or linear manner so that Coriolis force in all three spacial dimensions can be measured. The sense mode usually has comb drives for the in-plane sensing z-axis, but parallel plate structures in the out-of-plane sensing x- and y-axes. The force by parallel plate and comb drive capacitive actuators is

$$F_{\mathrm{para}} = \frac{\epsilon A}{2x^2}V^2 \qquad \text{and} \qquad F_{\mathrm{comb}} = \frac{\epsilon N h}{g}V^2, \tag{3.2}$$

where ϵ is permittivity, A the parallel plate area, x the plate distance, N the number of interdigitated fingers, h the height of the fingers, g the gap between two fingers and V the actuation voltage [33] [156]. Note, that force is a function of displacement in parallel plate capacitors but not in comb capacitors. Replacing the two fractions by constants k_{dr} and k_{fb} one receives the linear equations of motion for the two modes

$$F_{\mathrm{dr}} = k_{\mathrm{dr}}(V_{\mathrm{DR,ac}}\sin(\omega_{\mathrm{pll}}t) + V_{\mathrm{DR,dc}})^2 = m_x\ddot{x} + c_x\dot{x} + k_x x \tag{3.3}$$

$$F_{\mathrm{sn}} = k_{\mathrm{fb}}V_{\mathrm{FB}}^2\mathrm{sign}(V_{\mathrm{FB}}) = m_y\ddot{y} + c_y\dot{y} + k_y y + 2m_x k_{\mathrm{gyr}}\Omega_{\mathrm{r}}\dot{x}. \tag{3.4}$$

Here, F_{dr} and F_{sn} are the drive and sense forces, $V_{\mathrm{DR}} = V_{\mathrm{DR,ac}}\sin(\omega_{\mathrm{pll}}t) + V_{\mathrm{DR,dc}}$ the drive and V_{FB} the force-feedback voltage, m_x and m_y the masses, c_x and c_y the damping coefficients and lastly k_x and k_y the spring stiffnesses. The frequency of the drive vibration is forced by ω_{pll}. The gyroscopic factor k_{gyr} determines what ratio of the entire drive frame mass m_x actually induces Coriolis force for an individual sense axis. Furthermore, in some designs mass

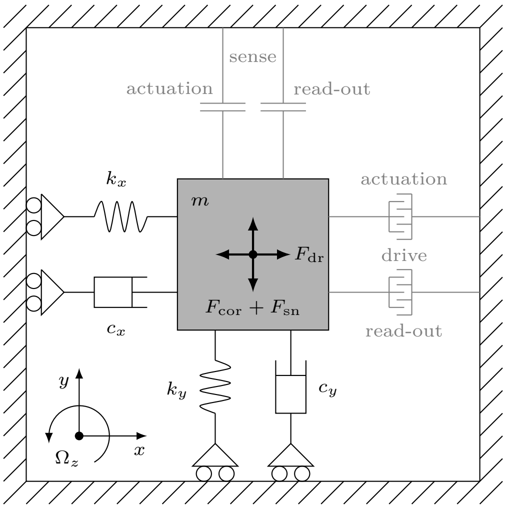

Figure 3.1.: Schematic of the mechanical functional principle of a Coriolis vibratory gyroscopes modeled as a lumped mass-spring-damper system [32] [92] [95] [150] [151] actuated by interdigitated comb drives or parallel plate capacitors. No non-idealities are shown in this figure and Coriolis force is thus the only energy transfer from drive to sense mode.

m_y may be physically a substructure of m_x. Alternatively, m_x might be include a so-called Coriolis frame which passes on Coriolis force to a separate sensing structure m_y that is mostly at rest and is not part of the drive frame, see e.g. [29]. The actuation and read-out capacitances of drive and/or sense might also be physically the same structure, if time-multiplexing is employed. In order to avoid measuring linear vibration instead of angular rate, the sensor's entire mechanical structure is almost always mirrored, with opposing movement and differential read-out [29]. For the sake of simplicity, the formulas and the simulation implementation here do not include the opposing movement.

3.2.1. Offset Sources

Angular rate offsets appear in virtually all MEMS gyroscopes and have numerous causes, many of them related to the specific control architecture. A limited number of publications have dealt with identifying and differentiating of offset sources explicitly [150] [157] [158] [159] [160]. Under ideal conditions, the offsets would be constant and would therefore not produce bias instability. Angular rate offsets are also easily calibrated to zero by simply keeping the device at rest for a few seconds. Investigating bias instability is therefore not the search for the dominant offset type, but for which offset type might carry enough 1/f noise to partly of fully explain the amount of experimentally measured bias instability. As mentioned above, flicker noise on the voltage converters is deemed as the mostly likely source of 1/f noise [78]. However, since the angular rate signal measurement happens modulated at the drive frequency, low-frequency flicker noise should in theory have no significant influence on the final sensor output. Bias instability mechanisms are therefore more complex. Different types of offsets are analyzed below and then modeled together with flicker noise sources to examine in simulation which combination of noise and non-ideality might produce bias instability. A gyroscope output Ω may be produced by these root causes, among others. For further details, see the above mentioned publications.

- *Angular rate:* The externally applied rotation Ω_r of the sensor leads to the desired measurement as described above. Depending on orientation of the sensing axis, a gyroscope always measures a portion of Earth's rotation, at most 4.2 mdps.

- *Quadrature:* This is the most important error source in MEMS gyroscopes, evidenced by the large amount of scientific contributions concerned with it, see Table 3.1. Quadrature occurs, when the drive movement is not perfectly perpendicular to the sense axis, i.e. the sense mode is excited by the *position* of the drive mass via coefficient k_{xy}. Since angular rate is transferred with *velocity*, quadrature and Coriolis force are separated in phase by 90 deg. By synchronous demodulation, both signals can be extracted individually. Oftentimes, quadrature is much larger than typical angular rates - up to tens of thousands of dps. In force-feedback systems, a quadrature cancellation loop is usually necessary because the sense front-end of the force-feedback loop would saturate otherwise.

- *Non-proportional damping:* Similarly, to quadrature, this effect is the excitation of the sense mode but by the drive *velocity* via coefficient c_{xy}. Since the mechanism is the same as for Coriolis force, this offset type can by definition not be differentiated from applied angular rate.

- *Drive force coupling:* The drive actuation may have asymmetries or produce fringe fields which let the drive force F_dr act directly on the sense mode via k_df. The effect is in phase with rate, not with quadrature, because the sense force-feedback dynamics have zero phase shift at the drive frequency (see Figure 3.3) as compared to the drive dynamics which have the typical minus 90 deg phase shift of a lumped mass-spring-damper system at resonance. This offset effect can be identified experimentally by applying an off-resonant frequency to the drive mode. The drive is therefore only barely in motion and any measured rate offset is thus likely to originate from drive force coupling.

- *Additional modes:* A MEMS gyroscope is a complex structure with subdivided masses and numerous spring structures. Inevitably, it therefore features many more mechanical modes than just the drive and sense modes. All above mentioned effects may also excite one of these additional modes and its movement might then influence the sense dynamics or the read-out, here modeled with $k_{\mathrm{cv}u}$. Since these additional modes are typically above the drive mode in resonance frequency, they are also called higher modes. Additional modes and non-linearities were shown to form complex dynamical behavior in [161]. Efficient simulation of some of these non-linearities was demonstrated in [162]. The entire topic of additional modes demands more research than what can be covered by our examination of bias instability sources in this dissertation.

- *Electrical cross-coupling:* Parasitic capacitances might directly couple control voltages like drive voltage, ASIC clock or any other ASIC signal to the sense front end, without any mechanics involved. Here, we model drive voltage via coefficient k_{cvd} to be the offset source.
- *Phase errors:* Lastly, the phase of the synchronous demodulation to receive the angular rate signal may not be perfectly precise. Small components of the quadrature signal may therefore creep into the rate signal. Since quadrature compensation control reduces the actual quadrature movement to zero, this effect is not deemed to be substantial in our implementation.

In this model, an additional light duffing behavior k_{xd} may be included in the drive mode, which in itself is not capable of producing offsets. The implementation also comprises quadrature compensation and common-mode voltages V_{QC}, V_{QCM} and their efficacy k_{q}, as well as frequency tuning voltage V_{FT} with spring softening capability k_{ft}. The model is described in the time-domain with dynamic equations of motion for drive mode,

$$F_{\mathrm{dr}} = k_{\mathrm{dr}}(V_{\mathrm{DR,ac}}\sin(\omega_{\mathrm{pll}}t) + V_{\mathrm{DR,dc}})^2 = m_x\ddot{x} + c_x\dot{x} + k_x x + k_{xd}x^3, \tag{3.5}$$

the potential additional mode,

$$0 = m_u\ddot{u} + c_u\dot{u} + k_u u + k_{xu}x, \tag{3.6}$$

the sense mode,

$$\begin{aligned} F_{\mathrm{sn}} &= k_{\mathrm{fb}}V_{\mathrm{FB}}^2\mathrm{sign}(V_{\mathrm{FB}}) + k_{\mathrm{df}}F_{\mathrm{dr}} \\ &\quad + k_{\mathrm{q}}((V_{\mathrm{QCM}} + V_{\mathrm{QC}})^2 - (V_{\mathrm{QCM}} - V_{\mathrm{QC}})^2)\sin(\omega_{\mathrm{mec}}t) \\ &= m_y\ddot{y} + c_y\dot{y} + (k_y + k_{\mathrm{ft}}V_{\mathrm{FT}}^2)y + (c_{xy} + 2m_x k_{\mathrm{gyr}}\Omega_{\mathrm{r}})\dot{x} + k_{xy}x \end{aligned} \tag{3.7}$$

and the output of the sense read-out capacitance-to-voltage (CV) converter which measures displacement via capacitance,

$$V_{\mathrm{CV}} = k_{\mathrm{cv}y}y + k_{\mathrm{cv}u}u + k_{\mathrm{cvd}}V_{\mathrm{DR}}\sin(\omega_{\mathrm{pll}}t). \tag{3.8}$$

Dots signify derivation in time t. Sense displacement is modeled as proportional to capacitance, which is transformed to voltage by $k_{\mathrm{cv}y}$. k_{xu} is the excitability of the assumed higher mode by the drive movement. Once steady-state is reached, the drive voltage frequency ω_{pll} is virtually identical with the drive's actual movement frequency ω_{mec}. Figure 3.2 reveals the offset paths within the control architecture and furthermore indicates the sensor's common mode voltage V_{CM} which was not modeled for the simulation. The demodulation phase determines if the offsets appear in the rate signal, quadrature signal or in both.

3.2.2. Sources of 1/f Noise

Flicker noise is assumed to appear wherever analog voltages are being generated. Primarily, that would be the digital-to-analog voltage converters (DACs). However, the analog-to-digital (ADCs) and CV converters may also use analog reference voltages and therefore experience flicker noise. All components that are realized in the digital domain are flicker free, of course. Whether wiring and electro-mechanical elements within the MEMS element can produce flicker noise is uncertain and for now this possibility is disregarded. Figure 3.2 includes a hatched bar under each component where a 1/f noise source was modeled.

As mentioned in Chapter 1, the 1/f behavior might also be produced by white noise which is shaped, i.e. filtered, to appear as bias instability for a limited range of τ_{AD} [50]. This type of correlated noise is sometimes also referred to as Gauss-Markov noise [163]. White noise is ubiquitous throughout the entire sensor e.g. due to Brownian motion, thermal or quantization noise. The possibility of shaped white noise producing bias instability is deemed unlikely but not entirely impossible. It will be discussed later on in this chapter.

3.2.3. Closed-Loop Control Structure

Figure 3.2 shows a signal flow graph with five control loops, compare [28] [29] [151]. The single drive frame movement is regulated by an amplitude control, which ensures that a constant vibrational amplitude of about $6\,\mu$m is maintained. The phase-locked loop (PLL) keeps the excitation frequency at resonance, so that the least amount of energy is expended. The bottom three control loops are realized individually for each individual axis. A high-bandwidth force-feedback control counteracts and largely suppresses movement of the sense mode within a certain frequency range, compare Figure 3.3, be they Coriolis-induced, quadrature or any other type of offset. The control's feedback output, i.e. the plant input (German: *Stellgröße*), is used to recover the angular rate and quadrature signal by synchronous demodulation and subsequent low-pass (LP) filtering. Around this inner loop, a quadrature compensation with bandwidth of less than 100 Hz applies voltages to dedicated quadrature compensation electrodes which counteract the mechanical quadrature until there is zero quadrature left. The modulation of the slowly varying quadrature

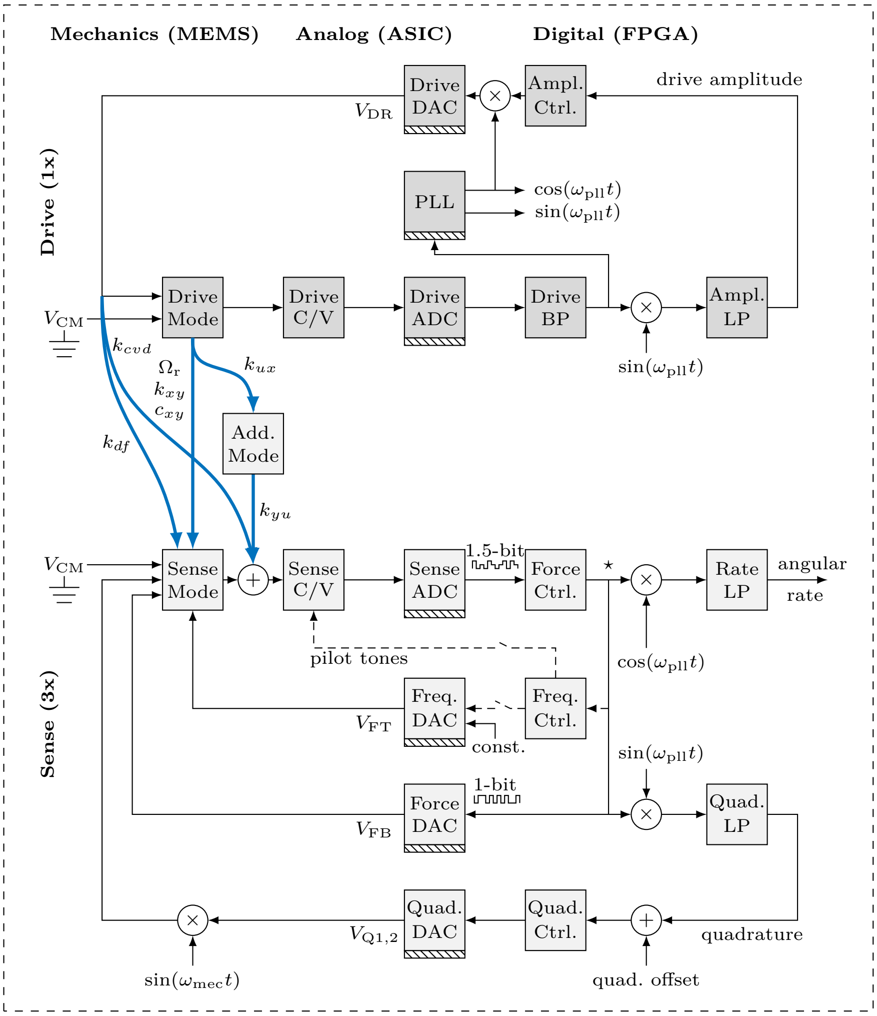

Figure 3.2.: Mode-matched MEMS gyroscope signal diagram with amplitude control and phase-locked loop (PLL) to regulate the drive movement as well as force-feedback, quadrature and frequency tuning control for each sense axis [2]. The above described offset sources are indicated by their coefficients and the blue arrows. The hatched bars show where a 1/f noise source was modeled in simulation. Synchronous demodulation and subsequent low-pass (LP) filtering grants drive amplitude, angular rate and quadrature. © 2019 IEEE.

compensation voltages to the drive frequency is done mechanically with ω_{mec}, i.e. the quadrature electrodes project a force onto the sense mode depending on the sense mode's position [150]. The drive and sense modes are matched to a few Hz by electrostatic frequency softening via dedicated frequency tuning electrodes. Matching is typically done once at the factory and that voltage value is maintained for the gyroscope's entire lifetime. Alternatively, a frequency tuning control loop may be closed, which measures the current detuning value and brings it to zero. A method based on pilot tones is described below and a novel technique is developed in Chapter 4.

All DACs and ADCs within the gyroscope are implemented as $\Delta\Sigma$ modulators for improved linearity and noise performance. Particularly the force-feedback control producing a 1-bit output is carefully designed to shape quantization noise away from the drive frequency towards higher frequencies where it does not influence the noise level of the demodulated, low-pass filtered angular rate output signal. The full details of our implementation can be found in [28].

3.2.4. Force-Feedback Transfer Functions

The transfer function from applied angular rate Ω_{r}, modulated onto the drive frequency, to the force-feedback control output ($\star$ in Figure 3.2) is sought to be as constant as possible over a large frequency range around the drive frequency. At the same time, white noise or any other disturbance acting on the CV converter should be suppressed as much as possible around the critical drive frequency. Force-feedback control delivers just that. Its transfer functions are

$$H_{\Omega_{\mathrm{r}}\dot{x}\to\star} = \frac{H_{\mathrm{sns}}H_{\mathrm{CV}}H_{\mathrm{ADC}}H_{\mathrm{fctrl}}}{1 - H_{\mathrm{sns}}H_{\mathrm{CV}}H_{\mathrm{ADC}}H_{\mathrm{fctrl}}H_{\mathrm{fDAC}}} \tag{3.9}$$

and e.g. for electrical cross-coupling in front of the CV.

$$H_{k_{\mathrm{cvd}}V^2\to\star} = \frac{H_{\mathrm{CV}}H_{\mathrm{ADC}}H_{\mathrm{fctrl}}}{1 - H_{\mathrm{sns}}H_{\mathrm{CV}}H_{\mathrm{ADC}}H_{\mathrm{fctrl}}H_{\mathrm{fDAC}}}. \tag{3.10}$$

Here, H are sense transfer functions. Force control and force DAC are abbreviated by fctrl and fDAC, respectively. In the vicinity of the sense mode resonance frequency $\omega_y = \sqrt{k_y/m_y}$, H_{sns} has high gain, the 1 in the denominators becomes insignificant and most terms can be canceled. If it is furthermore assumed that the force DAC has roughly linear characteristic, then

$$H_{\Omega_{\mathrm{r}}\dot{x}\to\star}\Big|_{\omega_y} \approx \frac{1}{-H_{\mathrm{fDAC}}} \approx \frac{1}{k_{\mathrm{fDAC}}} \tag{3.11}$$

$$H_{k_{cvd}V^2\to\star}\Big|_{\omega_y} \approx \frac{1}{-H_{\mathrm{fDAC}}H_{\mathrm{sns}}} \approx \frac{1}{k_{\mathrm{fDAC}}H_{\mathrm{sns}}}. \tag{3.12}$$

Around the drive frequency, the angular rate transfer function is thus approximately linear, as desired. The CV transfer function is roughly the *inverse* of the sense mode in this frequency range, which forms the characteristic “notch” of force-feedback gyroscopes, suppressing noise and disturbance signals at the CV converter. Figure 3.3 shows a Bode diagram of both transfer functions.

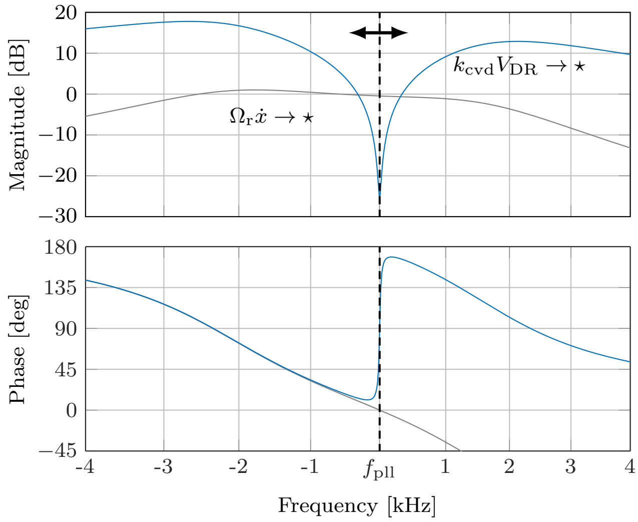

Figure 3.3.: Exemplary bode diagram of closed-loop force-feedback transfer functions of rate (*gray*) and CV (*blue*) to the force control output ($\star$) [2]. The magnitude scaling of the CV transfer functions is arbitrary, depending on how much cross-coupling signal or CV noise is modeled. The quadrature control loop is not included in the transfer functions. The drive frequency is marked by the vertical dashed line. If drive and sense modes become mismatched, the transfer functions move slightly left or right, as indicated by the arrow. Signals that pass the rate transfer function like applied angular rate or non-proportional damping are not affected much, but offsets undergoing the CV transfer function are drastically influenced in amplitude and phase. © 2019 IEEE.

3.2.5. Pilot Tones

Identifying the ideal mode-matching of each sense mode can be done by sweeping the frequency tuning voltage with the device at rest and recording at which voltage the rate noise reaches a minimum. This is of course not a feasible method if the gyroscope is moved and it is also time-consuming for factory calibration where each second counts. A more advanced method was therefore developed in [28] [151] [164], which injects so-called pilot tones at the CV converter via switchable capacitor arrays by digitally modulating a low-frequency tone $\omega_{\mathrm{pt}} \approx 250\,\mathrm{Hz}$ onto the drive frequency ω_{pll},

$$S_{\mathrm{pt}}(t) = k_{\mathrm{pt}} \cos(\omega_{\mathrm{pt}} t) \cos(\omega_{\mathrm{pll}} t). \tag{3.13}$$

The factor k_{pt} is adjusted so that the tones have a rate equivalent magnitude significantly lower than the maximum angular rate that the force-feedback can handle. The tones pass the CV closed-loop transfer function detailed above and appear well-visible in the spectrum of the force control output, left and right of the drive frequency. Figure 3.4 shows an experimentally measured noise

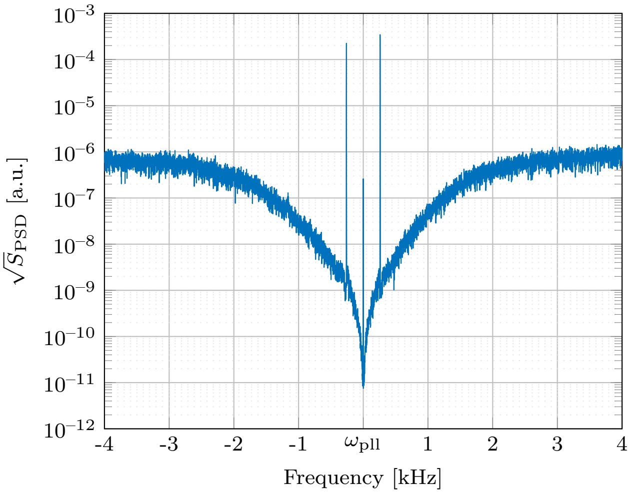

Figure 3.4.: Power spectral density of the force control output signal from experiment of one of the devices introduced below [2]. The two pilot tones appear left and right of the drive frequency ω_{pll}. The rate offset of the device can be seen in the center. The remainder of the spectrum consists of noise of all sorts of sources. Among them are $\Delta\Sigma$ quantization noise, additional $\Delta\Sigma$ dithers to prevent toning, CV noise, noise of the quadrature control and Brownian motion. More details on the noise composition is provided below and in Chapter 4. The typical notch shape is created largely by the CV transfer function in figure 3.3, but also from other contributors like the $\Delta\Sigma$ force-feedback and quadrature transfer functions.

spectrum with pilot tones. If the force control output is demodulated with S_{pt} and the outcome then low-pass filtered, a measure of frequency tuning is received. In other words, if the sense mode does not match the drive mode, one of the two tones will be amplified more and the other one less. The difference of the two tones' amplitudes is the measure of frequency detuning. Section A.9 of the appendix shows a simplified derivation in the time domain, the derivation in the frequency domain can be found in [151]. The detuning measure can be used to regulate the frequency tuning voltage via e.g. a simple integral control to permit continuous mode-matching, even in-run while measuring angular rate.

3.3. Simulation Analysis

The system dynamics including the non-idealities and offset sources introduced above were implemented within a Matlab/Simulink simulation environment. Compared to an existing simulation model available at the AE/EAC Bosch research department, this new model features only the most important components, which allows for a low simulation duration compared to simulation time. That is necessary to capture the long-term drift effects within reasonable time for a single simulation run. Proprietary, similar-to-experiment transfer functions for the control elements like the force-feedback control or amplitude control were used in the simulation. Nonetheless, the general trends of the simulation results are valid for a broad range of implementations of mode-matched, force-feedback gyroscopes. Figure A.11 in the appendix shows an overview of the Simulink model with subcomponents of white noise generation, MEMS element, drive controls, sense controls and output. To reduce simulation time and complexity, only one sense axis is modeled and a parametrization for the z-axis of the experimental devices from the next section is used from here on.

Noise in the $\Delta\Sigma$ force-feedback structure was carefully modeled to resemble the contributions within the actual, experimental devices. White noise sources were implemented for the drive CV thermal noise, the Brownian motion acting on the drive structure, thermal noise of the PLL output, thermal noise of the sense CV, Brownian motion acting on the sense structure, output noise of the quadrature DAC, output noise of the frequency tuning DAC and the dithers necessary for tone-free $\Delta\Sigma$ sense ADC and $\Delta\Sigma$ force-feedback DAC operation. Transfer functions for each noise type on the $\Delta\Sigma$ force control output spectrum were implemented, but are not directly relevant for the topic at hand. A result pane was created for the simulation, which plots time-series of relevant internal signals like quadrature and drive amplitude. It also provides the power spectral density of the force control output and the Allan deviation of the final rate output. If necessary, white noise sources - except the dithers - may be turned off, so that small influences of flicker noise producing bias instability can be observed without having to simulate for many hours until bias instability appears above angle random walk.

The flicker noise sources were modeled *additively* for the force-feedback, the quadrature control, the quadrature common-mode, the frequency tuning and the drive DACs as well as for the PLL. The drive and sense ADCs include flicker noise *multiplicatively*, i.e. their scale-factor changes slightly with a 1/f frequency characteristic. Figure A.11 in the appendix displays how the additive and multiplicative sources were implemented. Table 3.2 shows the assumed magnitude of flicker noise for each source. Where available, the values are aligned to the specification of the experimental ASIC in the next section. Flicker noise is typically specified by its level in a frequency spectrum at 1 Hz, and is given in units of μV/rtHz throughout this dissertation.

3.3.1. Offset Change by Detuning

The influence of accurate mode-matching on bias instability was mentioned in the state of the art section above. Here, the effects of detuning of the matched modes will be examined in detail. In practice, the natural, non-tuned frequency gap between drive and sense needs to be large enough so that even in the presence of fabrication variations all devices on a wafer have positive frequency splits $\Delta\omega_{\mathrm{split}} = \omega_{\mathrm{sn}} - \omega_{\mathrm{dr}}$. Since the negative electrostatic spring softening constant k_{ft} in our devices is accompanied by squared frequency tuning voltage, any negative split would not be removable. The simulation is parametrized so that the sense mode lies $\Delta\omega_{\mathrm{split}} \approx 600\,\mathrm{Hz}$ higher in frequency than the drive. With an electrostatic spring softening capability of $-11\,\mathrm{Hz/V^2}$, a frequency tuning voltage of 7.5 V is needed to match the sense mode to the drive mode.

The wide bandwidth of the closed-loop angular rate transfer function in Figure 3.3 makes the rate measurements relatively robust to smaller changes in frequency tuning. In fact, even if the frequency tuning voltage were to be increased by 1 V, resulting in a detuning of −170 Hz, the scale-factor of a measured rate signal would only be off by less then 4 %. Considering the minuscule voltage changes that originate from flicker noise as well as typical offsets that are less than 3 dps (see experiments in the next section), this path can hardly explain bias instabilities of e.g. 1 dph. In contrast, the closed-loop transfer function for cross-coupling to the CV converter in Figure 3.3 drastically changes signal amplitude and even more-so signal phase. Alternation of tuning voltage will therefore shift any cross-coupling signal in or out of rate or quadrature.

The simulation is employed to characterize the change of each type of offset when the sense mode is purposely detuned. The duffing behavior of the drive

Table 3.2.: Flicker noise magnitudes for each voltage in simulation. The values are aligned to the specification of the experimental ASIC. Dependence of flicker on the actual amount of output voltage was not modeled. High-voltage DACs exhibit higher flicker noise in general compared to low-voltage DACs.

Flicker Source	**Symbol**	**Value**
Units		[μV/rtHz]
Force-feedback DAC	$V_{\mathrm{FB,flic}}$	13
Quadrature control DAC	$V_{\mathrm{QC,flic}}$	350
Quadrature common-mode DAC	$V_{\mathrm{QCM,flic}}$	350
Frequency tuning DAC	$V_{\mathrm{FT,flic}}$	400
Drive DAC	$V_{\mathrm{DR,flic}}$	400
Analog PLL voltage	$V_{\mathrm{PLL,flic}}$	400
Scale-factor drive ADC	$S_{\mathrm{ADC,dr,flic}}$	13
Scale-factor sense ADC	$S_{\mathrm{ADC,sn,flic}}$	13

mode is disabled for these examinations. Assume an offset at perfect mode-matching, created by non-proportional damping of $\Omega_{\mathrm{np,sim1}} = 0.1\,\mathrm{dps}$. The necessary magnitude is $c_{xy} = 3.6 \cdot 10^{-11}\,\mathrm{Ns/m}$ in our implementation. A small detuning voltage of $\Delta \mathrm{V}_{\mathrm{FT}} = +10\,\mathrm{mV}$ is applied during a second simulation run, shifting the sense mode frequency by $-1.7\,\mathrm{Hz}$ and altering the offset to $\Omega_{\mathrm{np,sim2}} = 0.100035\,\mathrm{dps}$. The susceptibility of this type of offset, linearized at the ideal mode-matching, is thus

$$\begin{aligned} S_{V_{\mathrm{FT}},\Omega_{\mathrm{np}},\mathrm{sim}} &= \frac{\Omega_{\mathrm{np,sim2}} - \Omega_{\mathrm{np,sim1}}}{\Delta V_{\mathrm{FT}}} && (3.14) \\ &= \frac{0.100035\,\mathrm{dps} - 0.1\,\mathrm{dps}}{0.01\,\mathrm{V}} && (3.15) \\ &= 0.0035\,\mathrm{dps/V} && (3.16) \end{aligned}$$

in terms of rate offset change per amount of applied frequency detuning voltage. The same amount of offset originating from electrical cross-coupling to the CV converter, $\Omega_{\mathrm{ec,sim1}} = 0.1\,\mathrm{dps}$ via $k_{\mathrm{cvd}} = -11\,\mathrm{nm/V}$, prompts a much larger susceptibility to detuning of

$$\begin{aligned} S_{V_{\mathrm{FT}},\Omega_{\mathrm{ec}},\mathrm{sim}} &= \frac{\Omega_{\mathrm{ec,sim2}} - \Omega_{\mathrm{ec,sim1}}}{\Delta V_{\mathrm{FT}}} && (3.17) \\ &= \frac{0.132\,\mathrm{dps} - 0.1\,\mathrm{dps}}{0.01\,\mathrm{V}} && (3.18) \\ &= 3.2\,\mathrm{dps/V}. && (3.19) \end{aligned}$$

This offset type is thus almost a factor of 1000 more potent and even small tuning voltage changes result in significant offset drifts. The tiny voltage fluctuations from flicker noise may therefore create large amounts of bias instability, if some amount of electrical cross-coupling offset is present. Although offsets from (remaining) quadrature likely do not exist in our devices, they were modeled here as well. An artificial quadrature offset as depicted at the bottom of Figure 3.2 was introduced. About 24 dps of rate-equivalent quadrature offset was necessary to induce a rate offset of 0.1 dps due to non-perfect demodulation phase. Demodulation phase errors stem from slight differences of PLL phase and the phase of the actual mechanical movement or the closed-loop force-feedback transfer function not having precisely zero phase shift at ω_{pll}. Furthermore, an offset due to an additional mode was introduced with the mode having a Q-factor of 5000 at a frequency separation to drive of 12.7 kHz. During all these simulations, quadrature control as in Figure 3.2 was active. Detuning offset susceptibilities change somewhat when quadrature control is disabled.

Table 3.3 shows the result for all offset types that were presented above. The difference of impact between offsets experiencing the rate closed-loop transfer function (Ω_{np}, Ω_{fc}) versus the CV closed-loop transfer function (Ω_{ec}, Ω_{am}) can clearly be seen. Figure 3.5 shows the same offset changes but over a wider range

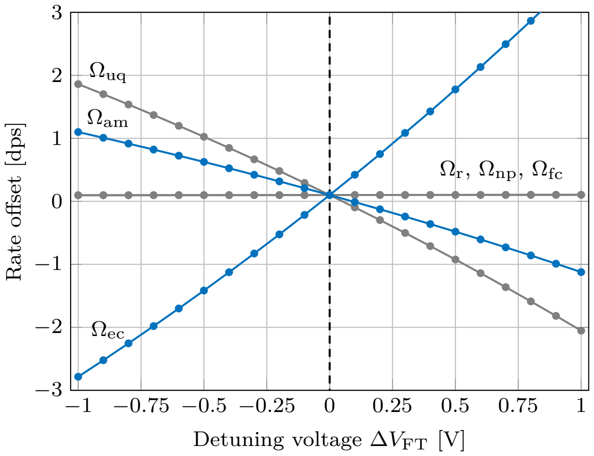

Figure 3.5.: Susceptibility of different types of offset to frequency detuning. All offsets were simulated with magnitude of 0.1 dps at perfect mode-matching, marked by the black, dashed line. Every dot indicates a separate simulation. Detuning voltage ΔV_{FT} drastically alters offset magnitude for the offsets that undergo the CV closed-loop transfer function (*blue*) but barely influences offsets that pass the rate closed-loop transfer function (*gray*), according to Figure 3.3.

of $\Delta V = \pm 1\,\mathrm{V}$ of detuning voltage. The analogous experimental characterization is presented in the next chapter. Note, that the sign of the susceptibility is arbitrary, since negative offsets are also possible. Drive force coupling offset is an exception and can only produce offsets of either positive *or* negative sign, depending on the sign convention of the output and the mechanical design. It is not easily possible to differentiate between offset types in experiment. Two

Table 3.3.: Susceptibility of different types of offset to frequency tuning changes. All offsets were simulated with magnitude of 0.1 dps in the perfectly mode-matched case. In a second simulation the sense mode was detuned by 10 mV, resulting in a −1.7 Hz frequency shift. The difference between offsets experiencing the rate closed-loop transfer function and the CV closed-loop transfer function from Figure 3.3 is striking.

Offset Type *Units*	**Symbol**	**Susc.** $S_{V_{\mathrm{FT}},\mathrm{sim}}$ [dps/V]
Applied angular rate	Ω_{r}	0.0035
Non-proportional damping	Ω_{np}	0.0035
Drive force coupling	Ω_{fc}	0.0033
Uncompensated quadrature	Ω_{uq}	-1.9
Electrical cross-coupling	Ω_{ec}	3.2
Additional mode	Ω_{am}	-1.1

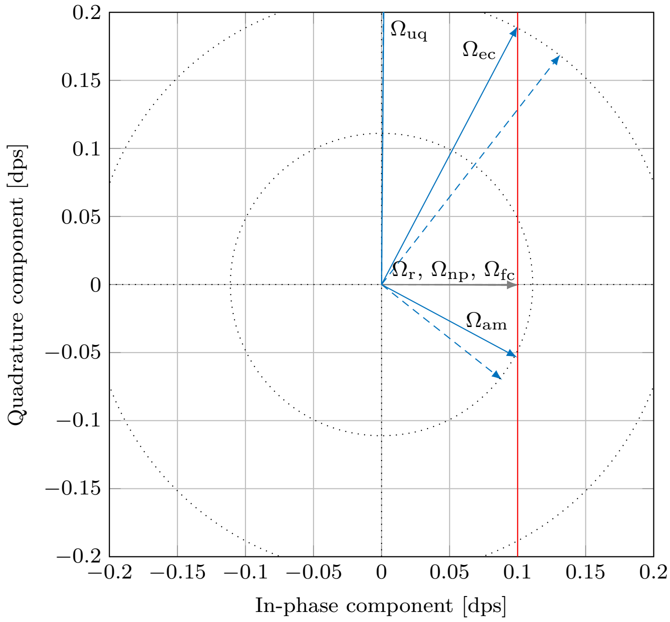

Figure 3.6.: In-phase and quadrature composition of different types of offsets with CV closed-loop transfer function (*blue*) and rate closed-loop transfer function (*gray*) with rate magnitudes of 0.1 dps (*red*). The offset from uncompensated quadrature is near vertical and not entirely visible in this plot, because the quadrature component amounts to a much larger 24 dps. When a detuning voltage of $\Delta V_{\mathrm{FT}} = 10\,\mathrm{mV}$ is applied, the pointers' magnitudes (*dashed*) remain about constant, as illustrated by the circles. However the phase angles of the offsets that undergo the CV closed-loop transfer function change significantly.

opposite-sign offsets may cancel each other, but a detuning susceptibility will still remain. Likewise, a device may exhibit a large offset of different origins, but their detuning susceptibility may cancel each other and total susceptibility becomes small.

A pointer diagram of in-phase, i.e. rate, and quadrature components of the six presented offset types is shown in Figure 3.6. The simulated offsets of 0.1 dps are accompanied by varying amounts of quadrature. Applied angular rate Ω_{r} and offsets Ω_{np}, Ω_{fc} that pass the rate closed-loop transfer function do not have a significant quadrature component. Furthermore, when a slight detuning voltage of $\Delta V_{\mathrm{FT}} = 10\,\mathrm{mV}$ is applied, the rate component does not change significantly, as detailed above. Since offsets Ω_{ec}, Ω_{am} undergo the CV closed-loop transfer function, even slight detuning alters their phases profoundly, as portrayed in Figure 3.3. The composition of in-phase and quadrature magnitudes therefore changes, however the total magnitude remains about the same. If larger detuning voltages are applied, then magnitude will begin to increase, according to the notch shape of the CV closed-loop transfer function.

3.3.2. Analytical Calculation of Bias Instability

The specified flicker noise parameter of the tuning voltage $V_{\mathrm{FT,flic}}$ from Table 3.2 and the offset susceptibilities towards tuning voltage variation $S_{V_{\mathrm{FT}},\mathrm{sim}}$ from Table 3.3 allow the direct, analytical calculation of the expected bias instability. Furthermore necessary is a factor of $\sqrt{2\ln 2}$ in units of rtHz, which comes from the definition of bias instability in equation (2.12). The full derivation is provided in Section A.10 of the appendix. Analytically predicted bias instability values are calculated here for offsets of 0.1 dps from uncompensated quadrature,

$$
\begin{aligned}
\sigma_{\mathrm{BIS},V_{\mathrm{FT}},\Omega_{\mathrm{uq}}} &= |S_{V_{\mathrm{FT}},\Omega_{\mathrm{uq}},\mathrm{sim}}| \cdot V_{\mathrm{FT,flic}} \cdot \sqrt{2\ln 2}\,\mathrm{rtHz} && (3.20)\\
&= 1.9\,\mathrm{dps/V} \cdot 400\,\mu\mathrm{V/rtHz} \cdot \sqrt{2\ln 2}\,\mathrm{rtHz} && (3.21)\\
&= 3.2\,\mathrm{dph}, && (3.22)
\end{aligned}
$$

for offsets from electrical cross-coupling,

$$
\begin{aligned}
\sigma_{\mathrm{BIS},V_{\mathrm{FT}},\Omega_{\mathrm{ec}}} &= |S_{V_{\mathrm{FT}},\Omega_{\mathrm{ec}},\mathrm{sim}}| \cdot V_{\mathrm{FT,flic}} \cdot \sqrt{2\ln 2}\,\mathrm{rtHz} && (3.23)\\
&= 3.2\,\mathrm{dps/V} \cdot 400\,\mu\mathrm{V/rtHz} \cdot \sqrt{2\ln 2}\,\mathrm{rtHz} && (3.24)\\
&= 5.4\,\mathrm{dph} && (3.25)
\end{aligned}
$$

and for offsets from the modeled additional mode,

$$
\begin{aligned}
\sigma_{\mathrm{BIS},V_{\mathrm{FT}},\Omega_{\mathrm{am}}} &= |S_{V_{\mathrm{FT}},\Omega_{\mathrm{am}},\mathrm{sim}}| \cdot V_{\mathrm{FT,flic}} \cdot \sqrt{2\ln 2}\,\mathrm{rtHz} && (3.26)\\
&= 1.1\,\mathrm{dps/V} \cdot 400\,\mu\mathrm{V/rtHz} \cdot \sqrt{2\ln 2}\,\mathrm{rtHz} && (3.27)\\
&= 1.9\,\mathrm{dph}. && (3.28)
\end{aligned}
$$

In the same manner, the influence of *any* other control voltage that produces a rate offset change may be examined for its impact on total bias instability. Section 3.4 below will demonstrate this using experimentally found voltage susceptibilities.

3.3.3. Simulation of Bias Instability

Next, offsets and flicker noise sources were simulated together, one by one. All white noise sources except the indispensable dithers were turned off, so that even very small bias instability values may be seen in the Allan deviation plot. The offsets passing the CV closed-loop transfer function were assumed to be 0.1 dps as above, but the rate closed-loop transfer function offsets were set to 1 dps. It was assumed that the vast majority of experimentally measured offset of a gyroscope is created by the latter type. Table 3.4 displays the simulation results. While most combinations did not yield detectably bias instability at all, flicker noise on the frequency tuning voltage in combination with CV closed-loop transfer function offsets did result in significant contributions. The results agree well with the analytically determined bias instability values above. Smaller influences were also found for the feedback DAC and the drive ADC. The former will be examined in more detail in Section 3.5.

The results explain for the first time the origins and mechanisms of bias instability as a combination of flicker noise on the frequency tuning DAC and offsets that are highly susceptible to detuning e.g. those that experience the CV closed-loop transfer function. It has become clear, why exactly in-run frequency tuning control improves bias instability as experimentally demonstrated in [93] [116] [143], because these control mechanisms counteract the small detuning changes and keep mode-matching ideal at all times. We demonstrate bias instability improvement using pilot tones firstly in simulation and then in experiment in the next section. Figure 3.7 presents a 10 h simulation of 0.1 dps of offset from an additional mode together with tuning voltage flicker. The first run prompts the result of Table 3.4, i.e. bias instability of 2.0 dph. In the second run, the pilot tone frequency tuning control is active and bias instability improves to 0.1 dph. At the same time angle random walk deteriorates, because white noise is swept into the rate output by the very same mechanism that bias instability is improved by. The effect is fortunately a bit less pronounced in the experimental implementation, because the typical voltage susceptibilities are much lower there.

Table 3.4.: Simulation results of bias instability due to a combination of offsets and flicker noise on the sensor's DACs and ADCs. Results were rounded to the first digit after the decimal point. Major contributions exist for the CV closed-loop transfer function offsets and the frequency tuning flicker.

Offset Type	Ω_{r}	Ω_{np}	Ω_{fc}	Ω_{uq}	Ω_{ec}	Ω_{am}
Magnitude	1 dps	1 dps	1 dps	0.1 dps	0.1 dps	0.1 dps
$V_{\mathrm{FB,flic}}$	<0.1	<0.1	<0.1	0	0	0
$V_{\mathrm{QC,flic}}$	0	0	0	0	0	0
$V_{\mathrm{QCM,flic}}$	0	0	0	0	0	0
$V_{\mathrm{FT,flic}}$	<0.1	<0.1	<0.1	**3.0**	**5.3**	**2.0**
$V_{\mathrm{DR,flic}}$	0	0	0	0	0	0
$V_{\mathrm{PLL,flic}}$	0	0	0	0	0	0
$S_{\mathrm{dr,ADC,flic}}$	<0.1	<0.1	<0.1	0	0	0
$S_{\mathrm{sn,ADC,flic}}$	0	0	0	0	0	0
Units	[dph]	[dph]	[dph]	[dph]	[dph]	[dph]

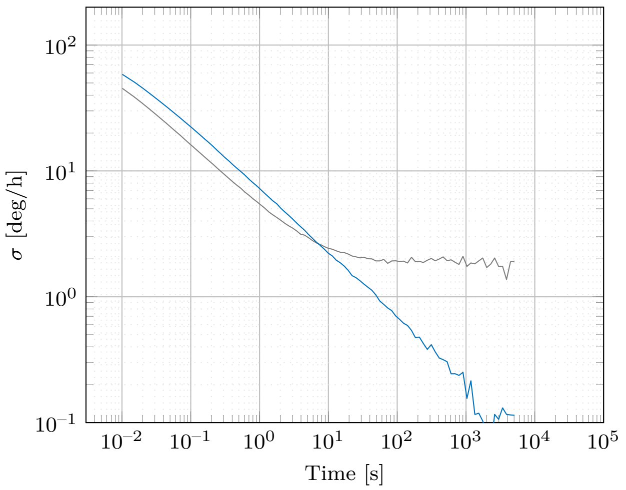

Figure 3.7.: Simulated bias instability (*gray*) of 2.0 dph with 0.1 dps of offset from an additional mode and frequency tuning voltage flicker. An improvement by a factor of 20 to 0.1 dph (*blue*) is facilitated by continuous frequency tuning control using pilot tones. The simulation time was 10 h in both cases.

3.4. Experimental Analysis

Simultaneously to mathematical modeling and simulation, extensive experimental investigations on fully-functional, triaxial research gyroscopes were performed. Well over 5000 hours of measurement data for Allan deviation analysis were recorded with many different devices, settings and laboratory conditions. This section presents only the most relevant outcomes.

3.4.1. Setup

The experimental setup consists of a field programmable gate array (FPGA) board, which runs the digital part of the sensor control system, see Figure 3.2. In its center, the board houses a ceramic leaded chip carrier (CLCC) on which an analog front-end research ASIC transfers the FPGA's actuation and readout signals to and from the actual triaxial MEMS gyroscope via bond-wires. Figure 3.8 shows such a device. The gyroscope dies were manufactured in-house at Bosch in Reutlingen with an advanced bulk micro-machining process which was previously presented in [98]. As opposed to operation exclusively via an ASIC like in a production device, the FPGA permits reprogramming of the controls as well as real-time examination and recording of most digital signals.

Ideal measurement conditions for Allan deviation have been described above. Passive insulation chambers within an air-conditioned laboratory were used to keep temperature as constant as possible. One such chamber is presented in Figure 3.8. The measurements shown here were sampled with 200 Hz using an internal, digital filter bandwidth of 80 Hz.

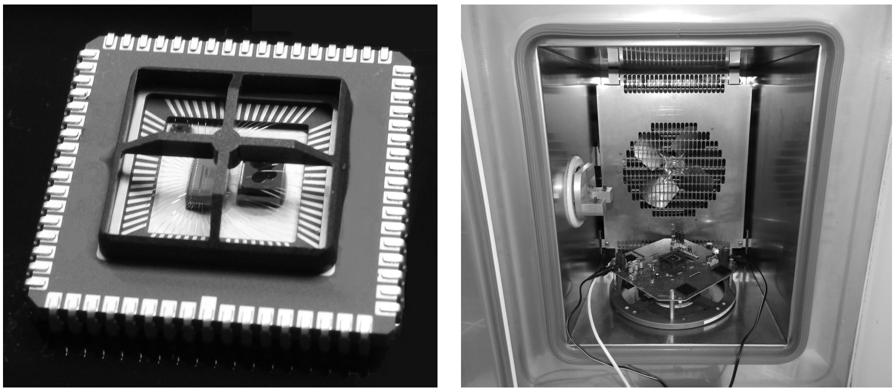

Figure 3.8.: *Left:* Sensor build-up on ceramic chip carrier with triaxial MEMS research gyroscope and an ASIC front-end connected by bond wires. *Right:* Setup of the FPGA board within a test chamber [2]. The chambers act as insulation from external disturbances, without any active climate control. © 2019 IEEE.

3.4.2. Allan Deviation Characterization

Five different sensor samples labeled A to F with similar mechanical designs are examined throughout this chapter. Devices A, B and C were recorded for a minimum of 48 h each and their Allan deviation characterized as presented in Figure 3.9. For all three axes in each device, the horizontal bias instability component is visible, but not always uniform in the out-of-plane axes. Angle random walk and bias instability parameters are shown in Table 3.5, together with the amount of offset, quadrature and tuning voltage needed for mode-matching. Certainly, three samples do not allow to draw any definitive statistical conclusions. Nonetheless, the amount of offset, quadrature or tuning voltage does not seem to directly correlate with bias instability levels. For the amount of offset in particular, no correlation was expected, as discussed above. With bias instabilities ranging from 0.15 to 1.2 dph in regular operation without any additional correction mechanisms, the devices exhibit exceptionally good long-term stability. Compared to other contributions in the state of the art, the devices here include axes for all three spacial dimensions on a single die within a very small area of less than 5 mm^2. White noise is very low as well, testament to the consequent $\Delta\Sigma$ implementation and good mechanical designs.

It was previously reported by the author, that the quadrature signal did not show significant correlation with the rate offset using another, related sensor design [1]. Employing the chance to access almost all digital control signals with the FPGA, extended correlation analyses were performed. It was found, that none of the rate offsets of different axes correlate with each other, meaning each axis has unique 1/f noise behavior. Furthermore, no other significant correlation of an axis' rate offset to one of the three quadratures, the drive amplitude, the drive input signal, the PLL signal or the drive frequency was found.

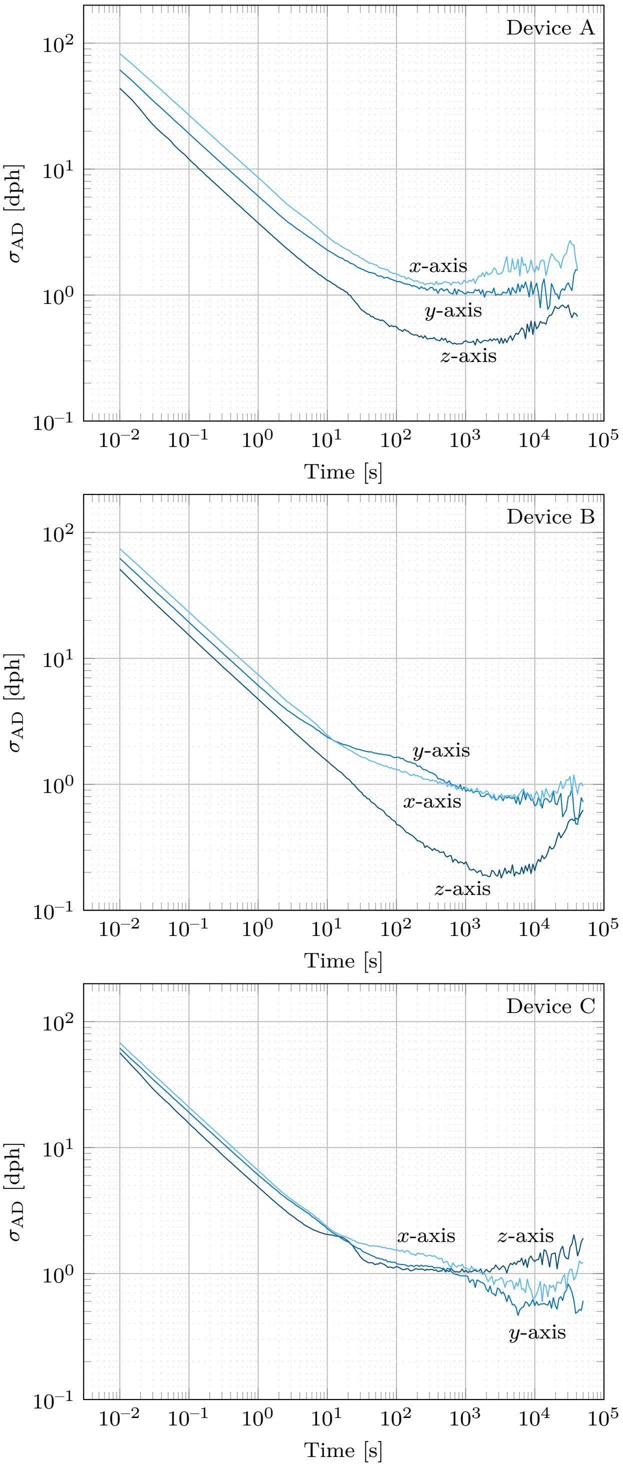

Figure 3.9.: Allan deviation of regular operation for at least 48 hours of devices A, B and C [2]. Resulting parameters are listed in Table 3.5. © 2019 IEEE.

Table 3.5.: Allan deviation parameters and general characteristics of devices A, B and C [2]. No direct correlation between the amount of quadrature, rate offset or tuning voltage to bias instability can be observed. Tuning voltage is given as the ratio of applied voltage divided by the full-scale range of the frequency tuning DAC, $V_{\mathrm{FT,max}}$. © 2019 IEEE.

x-Axis	**Sensor A**	**Sensor B**	**Sensor C**	*Units*
Rate offset	1.08	1.32	0.17	[dps]
Quadrature	6630	2440	-2500	[dps]
Tuning voltage	0.12	0.14	0.21	[$\mathrm{V/V_{FT,max}}$]
Angle random walk	2.4	2.1	1.8	[mdps/rtHz]
Bias instability	1.2	0.8	0.9	[dph]
y-Axis				
Rate offset	-0.14	0.21	0.24	[dps]
Quadrature	-2860	-1060	-350	[dps]
Tuning voltage	0.32	0.33	0.40	[$\mathrm{V/V_{FT,max}}$]
Angle random walk	1.7	1.7	1.7	[mdps/rtHz]
Bias instability	1.1	0.7	0.8	[dph]
z-Axis				
Rate offset	0.24	0.31	0.34	[dps]
Quadrature	-240	-130	-60	[dps]
Tuning voltage	0.48	0.46	0.50	[$\mathrm{V/V_{FT,max}}$]
Angle random walk	1.1	1.3	1.4	[mdps/rtHz]
Bias instability	0.4	0.15	1.0	[dph]

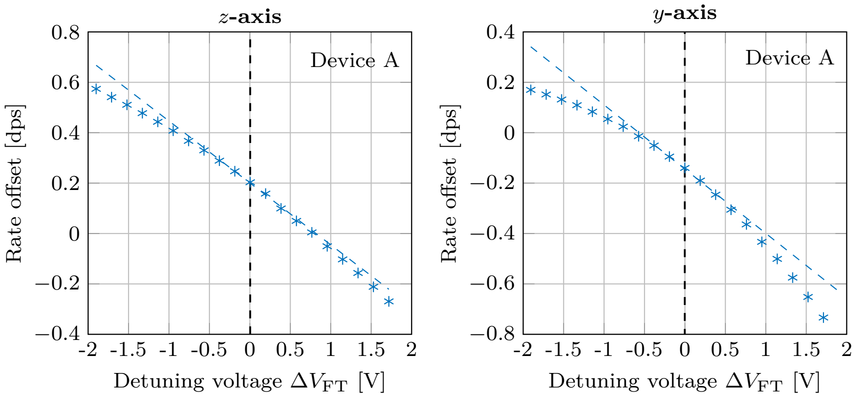

Figure 3.10.: Rate offset (*stars*) of sensor A at different detuning voltages in the z-axis (*left*) and y-axis (*right*) [2]. The vertical black lines mark ideal mode-matching with zero frequency split. A linear slope (*dashed, blue*) is fitted to this operating point. By chance, the susceptibilities are −0.25 dps/V in both cases here. © 2019 IEEE.

3.4.3. Variation of Voltages

In the simulation analysis above, different offset effects were examined. In experiment, it is however exceedingly difficult to separate and identify individual offset sources, if the total offset magnitudes are as small as they are here, see Table 3.5. Nonetheless, the effect of detuning on the total offset change can be examined. Exemplary, Figure 3.10 shows results from the z and y-axes of device A. The x-axis is omitted for the sake of brevity, because it is assumed that the two out-of-plane sensing axes will have similar bias instability mechanisms. A linear fit can be approximated to the experimentally found offset change and susceptibilities of

$$S_{V_{\mathrm{FT}},\Omega_z,\mathrm{exp}} = -0.25\,\mathrm{dps/V} \tag{3.29}$$

and

$$S_{V_{\mathrm{FT}},\Omega_y,\mathrm{exp}} = -0.25\,\mathrm{dps/V} \tag{3.30}$$

were determined. Both axes exhibit the same susceptibility only coincidentally here. For the other devices or the x-axis, voltage susceptibilities are different.

One can now make assumptions about what type of offset could create this particular amount of susceptibility. If non-proportional damping were the source, then, based on the susceptibility for 0.1 dps in Table 3.3, the experimental offset would have to be about 7 dps. That would be 30 times the measured offset amount for the z-axis and 50 times that of the y-axis. It is therefore reasoned, that instead, the experimentally measured susceptibilities are created by one of the CV closed-loop transfer function offsets, like electrical cross-coupling. Assuming electrical cross-coupling were the culprit, its magnitude would be

$$\Omega_{\mathrm{ec}} = 0.0078\,\mathrm{dps}. \tag{3.31}$$

Note that [2] shows different results, because the simulation parametrization has been adjusted since the submission of the paper. The general conclusion remains valid, of course. As in simulation, the resulting bias instability from flicker noise on the tuning voltage can be analytically calculated here as well. One receives for the z-axis

$$\sigma_{\mathrm{z,BIS},V_{\mathrm{FT}}} = |S_{V_{\mathrm{FT}},\Omega_z,\mathrm{exp}}| \cdot V_{\mathrm{FT,flic}} \cdot \sqrt{2\ln 2}\,\mathrm{rtHz} \tag{3.32}$$

$$= 0.25\,\mathrm{dps/V} \cdot 370\,\mu\mathrm{V/rtHz} \cdot \sqrt{2\ln 2}\,\mathrm{rtHz} \tag{3.33}$$

$$= 0.380\,\mathrm{dph}. \tag{3.34}$$

In this manner, *any* control voltage of the gyroscope may be examined and its contribution to the total bias instability level calculated. Beyond tuning voltage, significant influences were furthermore found for the quadrature common mode voltage. Unavoidably, quadrature voltage also causes some amount of electrostatic spring softening. The mechanism is therefore likely the same as the one of tuning voltage. Further voltages but with minor influences are the feedback voltage V_{FB} and the common-mode voltage V_{CM}. Table 3.6 contains the results for the z-axis of device A, i.e. the measured susceptibilities, the specified, worst-case flicker noise of the ASIC, the calculated bias instability components and their total. The flicker sources were assumed to be non-correlated here. Figure 3.11 shows the calculated levels for the z and y-axis of all three devices A, B and C. For the z-axis, the experimentally measured bias instability level from Table 3.5 can be explained very well by the presented mechanism of tuning voltage flicker. The prediction for device C is somewhat too large. One

Table 3.6.: Measured offset susceptibilities by voltage change, specified flicker noise of the employed research ASIC and calculated bias instability components [2]. Here, results for the z-axis of device A are shown. © 2019 IEEE.

	Suscept. $\lvert S_{V,\Omega_z},\mathrm{exp}\rvert$	**Voltage flicker** V_{flic}	**Bias instab.** $\sigma_{z,\mathrm{BIS},V}$
Units	[dps/V]	[μV/rtHz]	[dph]
$\mathbf{V_{FT}}$	0.25	370	0.380
$\mathbf{V_{QCM}}$	0.04	360	0.062
$\mathbf{V_{CM}}$	0.18	14	0.011
$\mathbf{V_{FB}}$	0.29	13	0.016
Total	-	-	0.390

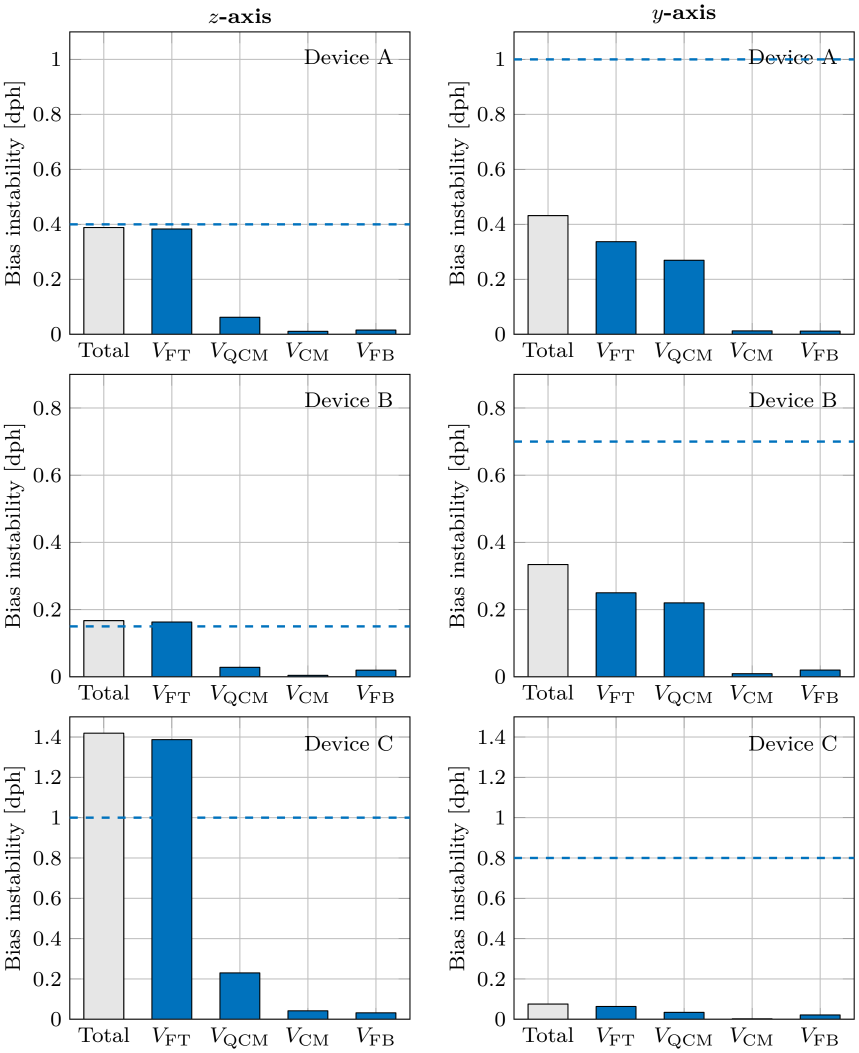

Figure 3.11.: Calculated bias instability components from variation of voltages (*blue bars*) and measured level (*dashed lines*) [2]. *Left:* z-axis levels are explained entirely by the proposed mechanism. While devices A and B match well, bias instability in device C is somewhat overestimated. *Right:* All y-axes show large discrepancies of 0.9, 0.6 and 0.8 dph for devices A, B and C. © 2019 IEEE.

reason might be, that the actual flicker noise level is lower than the worst-case specification for this device. The sensor build with bond-wires open to the air is also very delicate. Changes in the offset susceptibility could also have occurred between the Allan deviation and voltage variation measurement, which where actually more than four months apart for this device. As the noise components are added as the root of the sum of squares, a large contribution is yet unexplained in the y-axis. The x-axis behaves similarly. A discussion on

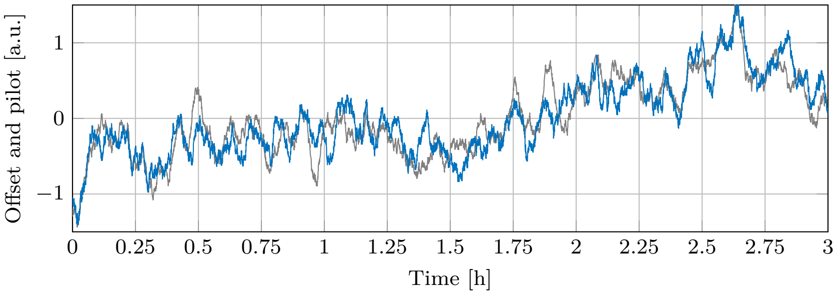

Figure 3.12.: Comparison of a pilot tone readout (*blue*) and angular rate (*gray*) of device A. The Pearson correlation coefficient between the two signals shown here is 0.87. Both signals were low-pass filtered and normalized for this figure. The pilot tone readout can be used to either immediately correct the frequency tuning of the sensor or to simply *digitally* correct the rate output.

bias instability in the out-of-plane axes is provided in Section 3.6.

3.4.4. Reduction of Bias Instability

Having confirmed, that bias instability on the z-axes is created by tuning voltage flicker, the pilot tones were used to facilitate a reduction in experiment for all three devices. Rate offset and pilot tone output signal were recorded for some hours, without closing the frequency tuning control loop yet. Figure 3.12 shows a comparison of both signals after low-pass filtering with a 150 s moving average and subsequent normalization scaling. A Pearson correlation coefficient of 0.87 signifies, that the pilot tone readout can in fact measure the slow drift of the rate offset. Two methods of improving bias instability are possible.

The first method would be to use the pilot tone output to digitally correct the rate signal without actually improving the slightly faulty frequency split. The advantages of this method are simple implementation and lower safety criticality, since the frequency split is not actively influenced. Disadvantageous is the presumed need for part-individual calibration of the scaling factor from pilot tone output to the correction signal that can be subtracted from the rate output. The extremely low-frequency low-pass filter will also inevitably have swing-in transients on the order of minutes, which prevent bias instability compensation right after start-up of the device.

The second possibility is to employ a frequency tuning control loop, that continuously compensates the small changes of tuning voltage and keeps ideal mode-matching at all times. A simple integral control is used to translate the pilot tone output into a regulating tuning voltage. Figure 3.13 displays the achieved bias instability improvement. All three devices show significant improvement and Allan deviation minima are reduced to 0.1 dph. Due to the distinct V-shape, the actual bias instability component is even lower, around 0.07 dph. Table 3.7 summarizes the results. For device C, which had the highest

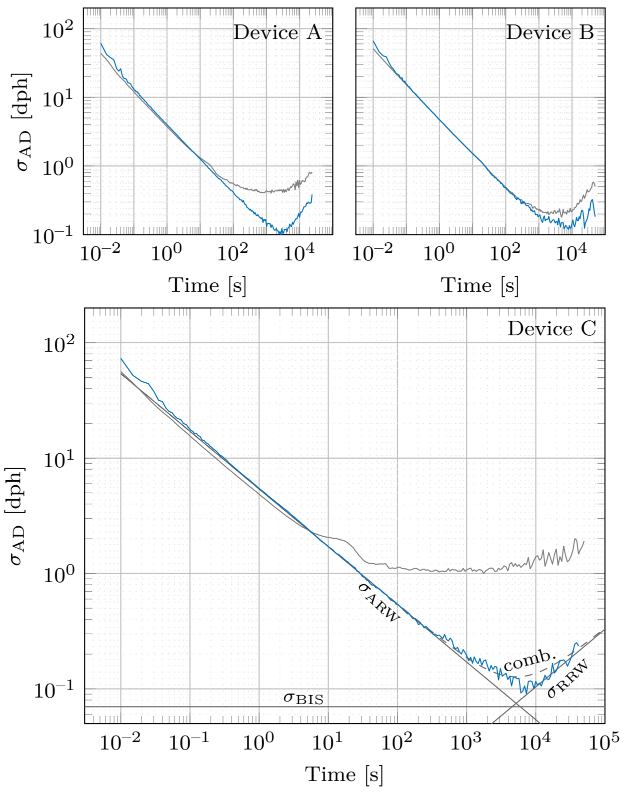

Figure 3.13.: Bias instability reduction by continuous frequency tuning control using pilot tones of the z-axes of sensor A, B and C (*blue*) for at least 24 h, compared to their regular operation (*gray*) [2]. Minima as low as 0.1 dph are achieved, an improvement by a factor of 10 for sensor C. © 2019 IEEE.

bias instability in regular performance, an improvement by more than a factor of 10 was achieved. The tuning voltage hypothesis was thus substantiated further.

At this level, bias instability is not a dominant contribution any more and other effects like rate random walk and temperature ramp would need to be improved to reduce the Allan deviation minimum further. Figure 3.13 also shows the appearance of a small ripple at short Allan cluster times, because the pilot

Table 3.7.: Regular operation and improvement by frequency tuning control [2]. Z-axis bias instability of all three devices decreases below 0.1 dph. © 2019 IEEE.

Z-axis	**Device A**	**Device B**	**Device C**	*Units*
Angle random walk	1.1 → 1.1	1.3 → 1.3	1.4 → 1.5	[mdps/rtHz]
Bias instability	0.4 → <0.1	0.15 → <0.1	1.0 → <0.1	[dph]
Bias instability	-75 %	-30 %	-90 %	[rel. change]

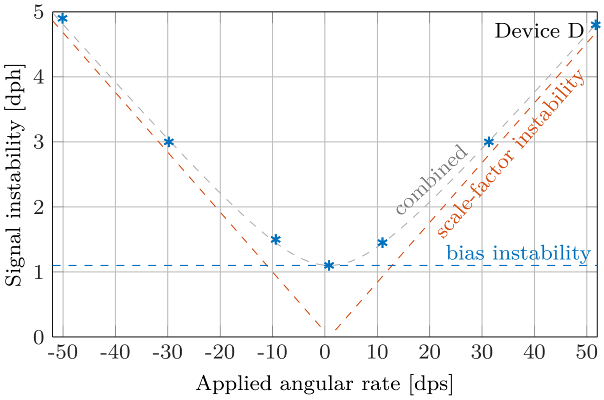

Figure 3.14.: 1/f signal instability levels at different angular rates lie on a combined curve (*gray*) of *bias* instability (*blue*) and *scale-factor* instability (*red*) [2]. Each blue star corresponds to a separate Allan deviation measurement of the y-axis of device D with a duration of at least 24 h. Scale-factor instability surpasses bias instability at angular rates larger than 13 dps. © 2019 IEEE.

tone was not entirely filtered out of the rate output. Device C also had a slight increase in angle random walk. Due to the higher voltage susceptibility in this sensor, the noise on the pilot tone signal counter-productively influenced the angle random walk by the very same mechanism that it improves bias instability. General advantages and disadvantages of tone-based and tone-free methods for measuring frequency detuning are discussed in the next chapter. As the results in Figure 3.11 predicted, stabilizing frequency tuning did *not* result in any improvement of the x and y axes. It is therefore reasoned, that the still-missing amount of bias instability of out-of-plane axes is unrelated to mode-matching.

3.5. Scale-Factor Instability

The denotation "bias instability" implies, that the drift is carried by the bias, i.e. the offset. This notion was challenged to further investigate the missing bias instability contributions in the x and y-axes. A series of experiments was conducted that examined if it is not rather the *scale-factor* that carries the instability. The constant offset would then just amplify that drift behavior. The FPGA board setup was mounted in an ultra-high precision rate chamber, see Figure A.13 in the appendix. Due to absolute angle measurement on the chamber, the machine is able to produce extremely constant angular rates. These are inherently bias instability free, according to the manufacturer.

Allan deviation measurements were performed at various positive and negative angular rates for at least 24 h for each experiment. Figure 3.14 reveals the "bias" instabilities measured on device D. It was found, that applied angular rate does in fact create significant additional signal instability with the typical 1/f

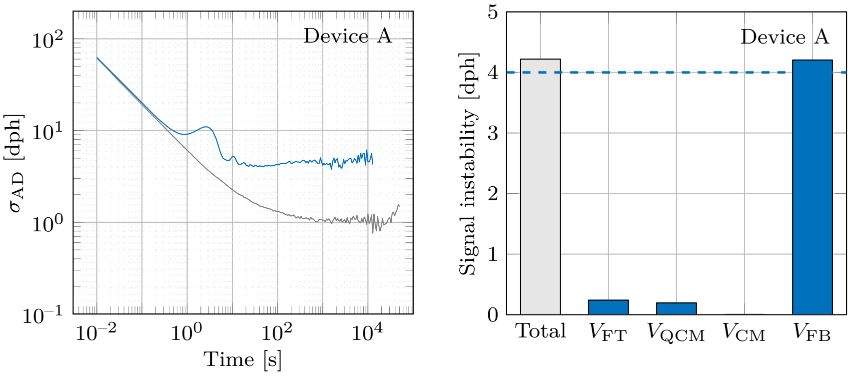

Figure 3.15.: *Left:* Allan deviation of the y-axis of sensor A measured for 22 h at a rotation of 50 dps (*blue*). In gray, the comparison with the measurement at rest is shown. The 1/f instability in the rate signal grows to 4 dph. *Right:* Contributions from voltage variation during the same rotation of 50 dps. The dashed, blue line marks the measured instability level of the experiment on the left. Force-feedback voltage V_{FB} forms the largest share by far and fully explains the observed signal instability [2]. © 2019 IEEE.

characteristic. The findings were furthermore confirmed with a number of other devices, that all exhibited the same behavior. The individual measurements are adequately explained by a combination of a true *bias* instability of about 1 dph and *scale-factor* instability (SIS) of

$$\sigma_{\mathrm{SIS}}(\Omega) = 2.6 \cdot 10^{-5} \cdot |\Omega|, \tag{3.35}$$

Note, that the effects are added as the square root of the sum of squares. The results imply, that bias instability ceases to be the dominant error component at angular rates as low as 13 dps. The implications of this result on the accuracy of purely inertial navigation in different applications is addressed in the discussion section below. The experiments also confirm, that a true bias instability *does* exist in the out-of-plane axes, and that measurements at rest contain only very little scale-factor instability. If the devices would have larger offsets of e.g. 20 dps - which is absolutely common for MEMS gyroscopes in general - then bias instability at rest would actually be dominated by scale-factor instability multiplied by the amount of offset according to equation 3.35.

Scale-factor instability effects are examined further in Fig. 3.15. A comparison between an Allan deviation measurement at rest and at 50 dps of applied rotation is shown for the y-axis of device A. During rotation, the Allan deviation shows a signal instability of 4 dph compared to 1.1 dph at zero-rate. In the same manner, that the sources of bias instability were examined by varying the control voltages, the sources of scale-factor instability can be calculated. For the same rotation of 50 dps, frequency tuning voltage flicker has a slightly decreased influence and is thus far from being the dominant component. In fact, continuous frequency tuning did not improve scale-factor instability. The once irrelevant share from the force-feedback voltage in bias instability has now become the largest contributor. Its rate output susceptibility is experimentally determined,

$$S_{y,V_{\mathrm{FB}},50\mathrm{dps,exp}} = -77.5\,\mathrm{dps/V}, \tag{3.36}$$

which gives a scale-factor instability amount of

$$\begin{aligned}\sigma_{\mathrm{y,SIS},V_{\mathrm{FB}},50\mathrm{dps}} &= |S_{y,V_{\mathrm{FB}},50\,\mathrm{dps,exp}}| \cdot V_{\mathrm{FB,flic}} \cdot \sqrt{2\ln 2}\,\mathrm{rtHz} && (3.37)\\ &= 77.5\,\mathrm{dps/V} \cdot 12.8\,\mu\mathrm{V/rtHz} \cdot \sqrt{2\ln 2}\,\mathrm{rtHz} && (3.38)\\ &= 4.2\,\mathrm{dph}. && (3.39)\end{aligned}$$

The measured signal instability can therefore be explained entirely by flicker noise on the force-feedback voltage. The same conclusion can be reached entirely by analytic calculation, without needing to measure the susceptibilities. As presented in Figure 3.2, the control structure employs a single-bit, $\Delta\Sigma$ force-feedback with *constant* positive or negative voltage V_{FB}. The scale-factor SF depends on small changes of force-feedback voltage ΔV_{FB} according to

$$\mathrm{SF}_{V_{\mathrm{FB}}} \approx \frac{V_{\mathrm{FB}}^2}{(\Delta V_{\mathrm{FB}} + V_{\mathrm{FB}})^2}. \tag{3.40}$$

The derivation is provided in Section A.11 of the appendix. The scale-factor difference to the ideal value of 1 is reached by linearization around $\Delta_{\mathrm{FB}} = 0$

$$\Delta\mathrm{SF}_{V_{\mathrm{FB}}} \approx 1 - \frac{V_{\mathrm{FB}}^2}{(\Delta V_{\mathrm{FB}} + V_{\mathrm{FB}})^2} \overset{\mathrm{lin.}}{\approx} 2\frac{\Delta V_{\mathrm{FB}}}{V_{\mathrm{FB}}}. \tag{3.41}$$

Using the ASIC's specified force-feedback voltage flicker noise of $V_{\mathrm{FB,flic}}$ scale-factor instability is then calculated according to equation (A.80) as

$$\begin{aligned}\sigma_{\mathrm{AD,SIS},V_{\mathrm{FB}\text{-}50\mathrm{dps}}} &\approx |\Omega| \cdot 2\frac{V_{\mathrm{FB,flic}}}{V_{\mathrm{FB}}} \cdot \sqrt{2\ln 2}\,\mathrm{rtHz} && (3.42)\\ &\approx 50\,\mathrm{dps} \cdot 2\frac{12.8\,\mu\mathrm{V/rtHz}}{1.23\,\mathrm{V}} \cdot \sqrt{2\ln 2}\,\mathrm{rtHz} && (3.43)\\ &\approx 4.4\,\mathrm{dph}, && (3.44)\end{aligned}$$

which is in good agreement with the value of 4.2 dph above. The minor differences between measured value, outcome from voltage variation and analytic results are attributed to deviations from the expected specification value of either the flicker noise or the force-feedback voltage magnitude. The scale-factor instability effect applies to all axes. It has been observed in all performed rotation experiments for many different devices. Due to the nature of the mechanism, the effect is

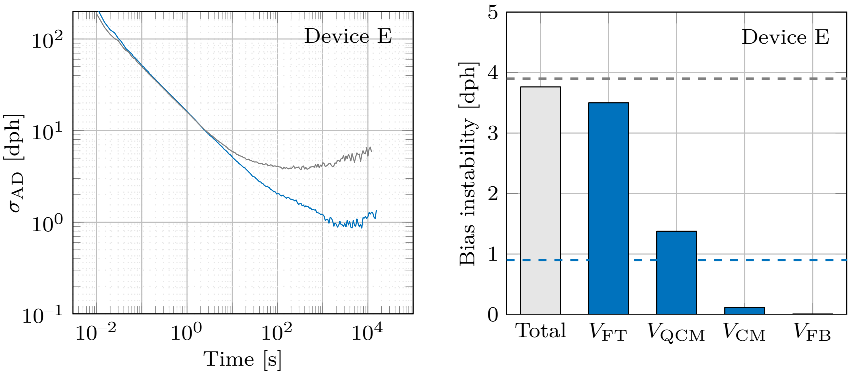

Figure 3.16.: *Left:* Allan deviation of regular operation of the out-of-plane y-axis of device E measured for 24 h (*gray*). Bias instability is reduced to 0.9 dph by continuous frequency tuning control using pilot tones (*blue*). *Right:* Calculated bias instability components from variation of voltages in regular operation (*bars*), measured bias instability level in regular operation (*gray, dashed line*) and after improvement by continuous frequency tuning (*blue, dashed line*).

inherent to all force-feedback type gyroscopes. Figure A.10 in the appendix examined scale-factor instability in open-loop MEMS gyroscopes and found no such effect, as the bias instability level remained the same at 200 dps of constant rotation. Naturally, more research is necessary for a definitive verdict on the existence of scale-factor instability within open-loop gyroscopes.

3.6. Out-of-Plane Axes

The voltage variation experiments above were not able to explain the measured bias instability level for the out-of-plane axes and large unknown shares remained for all three devices. This section is concerned with additional experiments and assessment. The goal is to provide an exemplary procedure on how to approach the root-cause analysis of bias instability beyond voltage variation.

Before delving into that, bias instability improvement by continuous frequency tuning control is demonstrated in an out-of-plane axis. One device was found to exhibit an exceptionally large offset susceptibility by frequency tuning of −2.2 dps/V. The resulting bias instability was around 3.9 dph as shown in Figure 3.16. Continuous frequency tuning control was able to reduce bias instability by a factor of four to 0.9 dph, but not lower, consistent with the analysis in the section above. As the bias instability components acting on detuning V_{FT} and V_{QCM} are removed, there is no further, large-enough component from variation of voltages that might explain the level of 0.9 dph.

The previous section has shown, that scale-factor instability does exist in the devices, but that the effect measured at rest is in fact true *bias* instability. One can therefore exclude any instability in the drive movement or the phase of the cosine demodulation signal that produces the rate signal, as both would act on scale-factor and not on bias. Both are even more implausible, because the z-axis would receive the same erroneous signal. Also, these effects would create correlations between the axes.

Table 3.8 shows the Pearson correlation coefficient of the low-pass filtered angular rate signal between the axes of devices A, B and C. No significant figures were found, with the exception of the y/z-axes of device A. Upon closer look, however, this slight correlation only appeared due to a similar temperature drift. Non-correlation of the 1/f noise in the out-of-plane axes rate outputs allows the exclusion of a whole slew of possible effects. Under assumption, that the two out-of-plane axes have the same bias instability mechanism, it can be reasoned, that no single source within the drive loop can be the origin. This includes effects of the PLL, the amplitude control or coupling of the drive voltage. The gyroscopically effective mass for the two out-of-plane axes is physically the same structure. Therefore even more complex effects like drifting phase-differences in the two counter-moving masses are dismissed.

A number of experiments have been conducted to learn more about the unknown bias instability component. Figure 3.17 presents two of them. Firstly, drive amplitude of device A was reduced without rescaling for correct scale-factor. It was found, that the bias instability level was then reduced accordingly. Bias instability stayed at roughly the same level if scale-factor was adjusted to the correct level. It is therefore argued, that the unknown bias instability share cannot originate solely from the sense read-out electronics or any other drive-independent or otherwise constant source, as higher drive amplitudes would then improve signal-to-noise ratios. In contrast, the small bias instability component from frequency tuning flicker as portrayed in Figure 3.11 stayed at about the same level without scale-factor correction. That means, that at least for this effect, higher drive amplitudes are beneficial. We can also follow, that the underlying offset is more likely to arise from electrical cross-coupling and not from effects related to higher-modes stimulated by the drive movement.

Secondly, the force-feedback voltage was doubled. Without rescaling for the correct scale-factor, bias instability was reduced by a factor of four. It thus

Table 3.8.: Pearson correlation coefficient of the axes of devices A, B and C, taken from the measurements in Figure 3.9. A moving average filter of 150 s was used to suppress angle random walk in the correlation calculation. No significant correlations were found.

Correl. Axes	**Device A**	**Device B**	**Device C**	*Units*
x/y	-0.14	-0.11	-0.18	[1]
x/z	0.06	0.24	0.17	[1]
y/z	0.45	0.28	-0.12	[1]

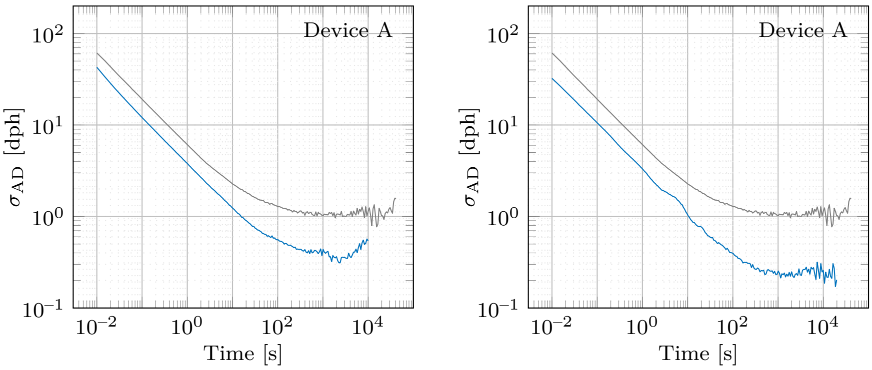

Figure 3.17.: Allan deviation analysis of the y-axis of device A with different settings (*blue*) compared to the regular operation (*gray*). *Left:* Drive amplitude was reduced to 25 % of its regular value. The resulting scale-factor change was not adjusted in this graph. The Allan deviation minimum is limited by the bias instability due to frequency tuning flicker of 0.4 dph as calculated in Figure 3.11. *Right:* Force-feedback voltage was doubled, resulting in a bias instability of 0.23 dph if scale-factor was not adjusted, i.e. about a fourth of regular operation.

behaves like measured angular rate according to equation (3.40). With corrected scale-factor, bias instability is largely independent of the amount of the single-bit force-feedback voltage. This result allows to dismiss effects where the force-feedback voltage would in some way birth bias instability, which has also been negated already by the voltage variation experiment in Figure 3.11.

For devices B and C in Figure 3.9, the out-of-plane bias instability level was not perfectly horizontal but more of a bump with a further minimum at even longer cluster times. This could be an indication, that the unknown bias instability component is not created by actual 1/f noise from flicker, but by correlated (Markov) noise [50], which creates a horizontal behavior in the Allan deviation plot only for a limited span of cluster times, as discussed above. The typical mathematical model for Markov noise is white noise being shaped by a first-order low-pass filter. The noise in the frequency range around the bandwidth of the filter becomes the 1/f component. The bandwidths would have to be around 5 to 1 mHz. If that mechanism exists, the next question would be if it applies to noise at or near DC. There, one would rather expect flicker noise instead of white noise, so this explanation seems implausible.

It my be observed, that in Table 3.5 the higher quadrature values in the out-of-plane axes of device A were associated with slightly higher bias instability. It could be, that the two out-of-plane channel quadrature feedback controls influence each other cross-wise and are therefore not fully capable of removing the flicker noise of their own quadrature voltages. A solution may be the implementation of a common multi-variate feedback control for both out-of-plane channels. This approach may be worked on in the future, but will not

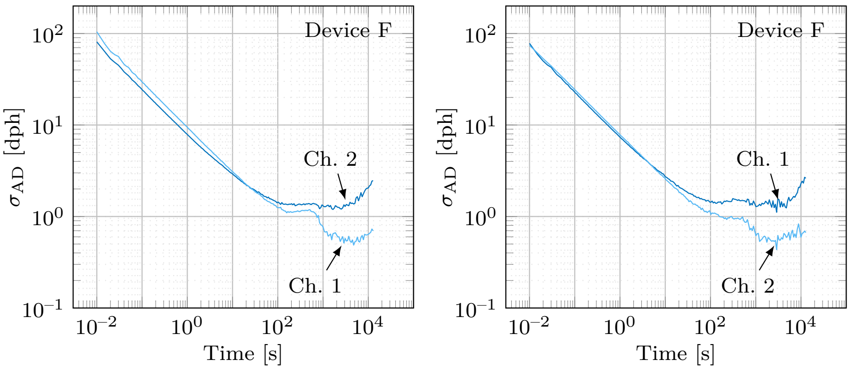

Figure 3.18.: Allan deviation analysis of the x-axis (*light blue*) and y-axis (*blue*) of device F using a new ASIC with reduced flicker noise on the quadrature and tuning voltage DACs. *Left:* Regular operation of the initial build-up of the device. *Right:* The same device but with a cross-swap of the wire-bonds connecting MEMS and ASIC for channels 1 and 2. The bias instability levels remain the same for the MEMS axes, not the ASIC channels.

be included in this dissertation. In opposition to this idea it was furthermore found, that when completely deactivating one out-of-plane channel and all its DACs, the other channel did not improve.

During the course of this dissertation, another analog front-end research ASIC was developed at Robert Bosch GmbH in succession to the ASIC used above. Heeding the advice of this dissertation, the flicker noise on the quadrature and tuning voltage DACs was significantly reduced by traditional circuit design measures. Any bias instability from offset susceptibility by voltages is consequently improved even without continuous frequency tuning control. Figure 3.18 shows the x- and y-axes of device F, a more recent MEMS design than devices A to E, using the new analog front-end ASIC. Interestingly, the bias instability of the two out-of-plane axes are not similar any more, with the x-axis reaching down to values of 0.6 dph and the y-axis staying at values similar to those of the previous ASIC model.

Now that the x- and y-axis actually exhibit a significant difference a cross-swap experiment was conducted. The wire-bonds connecting the MEMS pads to the ASIC pads were disconnected and then rebuilt in a way that the two channels were switched. That means, that all DACs of channel 1 that were previously serving the x-axis were then connected to the y-axis and vice versa. Figure 3.18 displays the Allan deviation afterwards. The bias instability level stayed very much the same for the axes and not for the channels. With a large likelihood, the root-causes of the bias instability difference are therefore to be found in the MEMS element, and not the ASIC.

So far, it was always assumed that flicker noise will only appear in the ASIC. The cross-swap experiment suggests, that the out-of-plane axes may perhaps produce flicker noise within the MEMS element. This idea will be investigated in the future, but not pursued here any further.

Table 3.9.: Methods for analyzing possible origins of bias instability.

Method	**Description**
Voltage variation	Vary all sensor control voltages, measure the resulting offset susceptibility, calculate the expected bias instability and compare to the measured level as described in Section 3.4.3.
Scale-factor instability	Measure the bias instability level at constant rotation of the sensor and assess if the level at rest is actually a true bias instability as demonstrated in Section 3.5. If no highly accurate rate table is available, one may allow some quadrature to be present and measure the bias instability of the quadrature signal.
Correlation between axes	Calculate the correlation of the low-pass filtered rate signals to each other and to any other available signal within the sensor as in Table 3.8. If no significant correlation is found, then a single source for several channels is unlikely.
Drive amplitude reduction	Measure the bias instability level with reduced drive amplitude as in Figure 3.17. If - after rescaling scale-factor - the bias instability level remains the same, one can likely exclude any effect that would originate solely in the read-out electronics.
Feedback voltage variation	Measure the bias instability level with reduced or increased feedback voltage as in Figure 3.17. If the bias instability level behaves like applied angular rate, then it is unlikely, that it originates from the feedback voltage.
Temperature variation	Flicker noise is typically lower at high temperatures, contrary to white noise [165] [166]. One may therefore analyze if flicker noise is actually the root-cause of the measured bias instability by running an Allan deviation experiment at e.g. -40°C.
Deactivating one axis	Disturbances from one axis to the other may be found by completely deactivating the DACs of one or two channels and measuring the remaining one.
Drive DC voltage variation	Vary the composition of drive DC and resulting AC voltage as in equation (3.5) and remeasure bias instability. It can then be deducted, if one of the two may be a root-cause.
Bandwidth variation	Measure the bias instability with increased or decreased bandwidth of e.g. the PLL, the drive amplitude control or the quadrature control.

Even though the sources of the unknown bias instability component in the out-of-plane axes could not be resolved in this dissertation, the excluded possibilities as well as the methodical approach will be of value for any reader trying to understand bias instability mechanisms in their devices. Table 3.9 summarizes the presented methods. The last four methods were not discussed in detail, but may be of avail to the reader nonetheless.

3.7. Discussion

Instead of using complex compensation mechanisms like pilot tones, an easier approach to improving bias instability would be to either reduce the susceptibility to voltage changes or to reduce the flicker noise [167] occurring on the voltage DACs. The latter is associated with trade-offs of increased ASIC area, higher power consumption or reduced full-scale voltage range. Naturally, an analog circuit designer will already have aimed at reducing the flicker noise as much as possible within the given boundary conditions. Nonetheless, low flicker noise must be prioritized in the conception phase of MEMS gyroscopes when inertial navigation is the use case. Another useful approach would be selective binning of devices on a waver with low frequency split. Those devices could be matched with an ASIC with lower full-scale voltage range, therefore lower flicker noise, and marketed separately from the other devices with regular performance.

Susceptibility of the offset to tuning voltage changes can be reduced by diminishing the offset paths that undergo the CV closed-loop transfer function. Offsets from additional modes may be decreased by adjusting the mechanical design. Moving their resonance frequency further away from the drive mode is beneficial. Best-as-possible symmetrization of the mechanical design is prudent, as it is for many other error effects. Wiring inside the MEMS element should be done in a way that reduces electrical cross-coupling. Furthermore, it is expedient to reduce the spring softening capability k_{ft}, so that if an offset susceptibility exists, it is less pronounced per amount of tuning voltage change. A trade-off exists however, since higher voltage output is associated with somewhat higher flicker noise. Another, approach is investigated in Section A.8 of the appendix. An artificial quadrature offset signal is used to compensate the susceptibility of other types of offsets. Due to deterministic disturbances this method would however deteriorate sensor performance even though it would improve bias instability. It was therefore not pursued further.

In comparison to the state-of-the-art noise performance of MEMS gyroscopes provided in Chapter 2, the devices here achieve much better merits in regular operation already. In fact, the same combined angle error after integration that is reached in Figure 2.10 within 10 s is met in the presented devices after 60 s of integration. Figure 3.19 compares the angle error for the z-axis of device C in regular operation with the continuous frequency tuning operation. A further

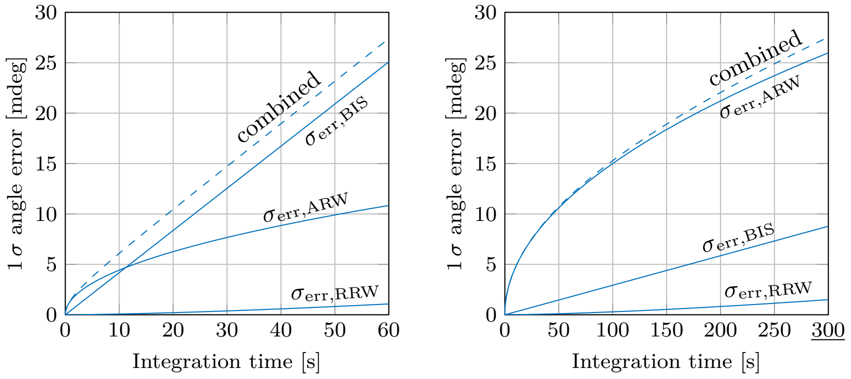

Figure 3.19.: *Left:* $1\,\sigma$ error angle of device C in regular operation with angle random walk of 1.4 mdps/rtHz, bias instability of 1.0 dph and rate random walk of $4\,\mu$dps/rts. *Right:* $1\,\sigma$ error angle of device C after improvement with continuous frequency tuning control using pilot tones, see Figure 3.13. Allan deviation parameters were a slightly increased angle random walk of 1.5 mdps/rtHz, much reduced bias instability and rate random walk of 0.07 dph and $0.5\,\mu$dps/rts, respectively. The dashed line shows the combination of all three noise terms. The time span to reach a similar angle error compared to the regular operation increased fivefold from 60 s to 300 s [2]. © 2019 IEEE.

factor of five in integration time is accomplished until the same error angle is reached. Due to the drastic bias instability reduction, angle random walk is now the dominant error source. Affirming our findings, an experimental study in [168] demonstrated, that GNSS-aided navigation accuracy was better for a gyroscope with low bias instability but higher angle random walk compared to a gyroscope with converse properties.

Although it was established in the introduction chapter that rate random walk is not a true device-intrinsic noise source, continuous frequency tuning also greatly reduced its level. Device C improved by a factor of eight from 4 to $0.5\,\mu$dps/rts. Keeping mode-matching ideal might therefore also improve the small temperature or stress influences that occurred despite the setup being in an insulation chamber.

Evidence and underlying theory for scale-factor instability has so far not been presented in the scientific community to the knowledge of the author. Highly-accurate rate tables may not always be available. A simple way to get a rough estimate of scale-factor instability is to disable the quadrature control and to measure the Allan deviation of the quadrature signal. Since the feedback mechanism is the same for quadrature and angular rate, the scale-factor instability level is also similar. In the z-axis of device A, an uncompensated quadrature of -330 dps was accompanied by a signal instability of about 30 dph, which agrees well with equation (3.35) above.

For the devices shown in this dissertation, scale-factor instability outgrew bias instability with rotation rates larger than about 10 dps. In automated driving applications, scale-factor influence may become relevant in certain scenarios. Angular rates are smaller than 10 dps most of the time, particularly so in highway driving or the presented emergency-stop maneuver. For vehicle navigation applications with longer times scales, the amount of left and right turns may also even out over time and thus naturally reduce the effect of scale-factor instability. Corner-cases like making a U-turn or driving on the spiral ramp of a parking garage may however be accompanied by large angular rates and therefore high scale-factor instability noise. Scale-factor instability may also be relevant in consumer devices and applications like indoor navigation or augmented/virtual reality because hand-held or body-mounted gyroscopes will experience much larger angular rates than what is typical in automotive applications.

The considerations on sensor redundancy are revisited again briefly. This chapter showed improvement in bias instability up to a factor of ten in one device. If the same accomplishment was to be achieved by using redundant devices, not correlated to each other, then the $\sqrt{N}$ law would apply and an excessive 100 sensors would have been necessary. This example illustrates the benefits of proper system understanding and consequential correction mechanisms.

4. A Novel Measure for Frequency Tuning and Scale-Factor

The previous chapter revealed the role of flicker noise occurring on the tuning voltage in the creation of bias instability. Likewise, flicker noise on the feedback voltage was demonstrated to produce scale-factor instability. Within this chapter, a novel, unified method for measuring, simultaneously, both detuning and scale-factor changes is presented and its performance analyzed. The main objective is to expand the prevailing solution space and to offer starting points, on which future research may be built. The first section provides an in-depth review of the state of the art on measuring detuning of the sense mode as well as existing methods for quantifying scale-factor. Next, the new measure is developed. A simulation study demonstrates the method's effectiveness. Lastly, benefits and limitations of the approach are discussed.

4.1. State of the Art

Matching of the drive and sense mode of commercial MEMS vibratory gyroscopes is in most cases performed only once, at the factory, and then kept at that value for the device's lifetime - up to 15 years. It was shown above, how small fluctuations off of ideal mode-matching can produce offset changes. Apart from the investigated flicker noise on the tuning voltage, fluctuations in mode-matching may appear in the field due to temperature, surface charges, bending stress or other types of voltage variations. Real-time, continuous frequency tuning control can drastically improve bias instability and rate random walk as shown in this dissertation, as well as stress susceptibility [143]. Electrostatic spring softening is an established and commonly employed technique to alter mode mismatch. However methods for *measuring* the mismatch are quite diverse and constitute an area of active research [116].

Methods for quantifying detuning may be differentiated in tone-based algorithms, that inject a calibration signal into the sensor system, and non-invasive approaches that measure by other means. Injecting tones into the quadrature compensation control loop outside of the sensor's bandwidth was demonstrated in [28] [93] [143] [169]. The latter contribution reached an Allan deviation minimum of 0.2 dph using this method. As it was demonstrated above, another reliable method is to apply pilot tones to the force-feedback loop, e.g. at the

CV converter [77] [151] [164] [170] [171]. Using a single tone *within* the signal bandwidth directly at the demodulation frequency was shown as well [92] [172]. Yet, limitations in the presence of larger quadrature signals or actually applied angular rate are most likely unavoidable. Pseudo-random sequences were used to identify stiffness and therefore natural frequency as well as damping in [173] [174]. The method is unfortunately not compatible with simultaneous angular rate measurement.

Tone-based methods share the disadvantage, that it is difficult to completely remove the tones from the angular rate output. The reason is not only imperfect filter suppression but also interference with other control circuits (e.g. quadrature nulling), electrical and mechanical nonlinearities, unavoidable higher modes, phase noise [28] and cross-coupling, which all may fold the tones or noise produced by it to many, unforeseeable frequencies. Especially in navigation applications, even very small cyclic signals in the rate output may not be acceptable for the Kalman filters that follow in the signal processing chain. Tone-based methods are furthermore susceptible to external vibration, if those coincide with the tone's frequency. On the other side, tone-based methods allow for highly precise readout, practically only limited by the admissible tone amplitude above the noise background.

Similarly to quantifying detuning, scale-factor has also been measured by the use of injected tones. In [106] a constant, "virtual" input rate is applied to the read-out electronics outside of the angular rate bandwidth. The measured amplitude of this artificial signal is proportional to the actual angular rate scale-factor and a scale-factor precision of 1 ppm was reached. The idea is extended in patent [175] to non-uniform signals that may lie within the angular rate bandwidth. Further methods exist, where interference with rate measurement is circumvented by applying a tone in quadrature phase to the drive circuit [140]. A twenty-fold improvement down to 130 ppm was demonstrated. The method stands out from the others, because it is also able to track scale-factor changes that originate in the drive loop. Lastly, scale-factor may be determined by putting the entire sensor on micro-stages for external calibration, see e.g. [176] [177]. These types of systems must however always justify why the sensor itself could not have been built in the first place with the same precision that is required for the micro-stage to provide an accurate reference to the sensor.

Non-invasive approaches have been examined less in literature. In-run mode-matching was achieved by a dual architecture where both modes are driven and sensed at the same time with significant reduction of unwanted temperature influences [114]. In certain devices the rate offset will have its maximum at perfect mode-matching [122]. Using this phenomenon does however not allow concurrent rate read-out. An adaptive control scheme was able to estimate stiffness and other sensor parameters in a simulation study [178] [179]. Instead of tuning the mechanical sense mode, a scheme was presented in [180] where two analog filters were periodically switched. A filter was either in usage within the force-feedback loop or outside of it where it was recalibrated. Recently, a method was demonstrated in experiment where the noise power of the $\Delta\Sigma$ modulator notch was evaluated left and right of the drive frequency [116] [181]. Some amount of robustness to external vibration influences as well as an Allan deviation minimum of 0.7 dph was shown.

4.2. Method Design

In this dissertation, a non-invasive approach is developed as well. The main challenge consists in whether a tone-free method can be devised, whose detuning and scale-factor measure is precise enough, i.e. of low noise, to allow reduction of the presented flicker noise effects. The basic principle is a system identification of the sense mode's natural frequency and low-frequency "DC"-gain that runs simultaneously to the regular, rate-measuring operation of the gyroscope. In order to do so, the existing noise in the $\Delta\Sigma$ force-feedback control is exploited. The method is called sense mode identification (SMID) in the following. Figure 4.1 shows again the mode-matched, closed-loop gyroscope structure that was introduced in Section 3.2. The same Matlab/Simulink simulation environment from the previous chapter is employed.

The different white noise components in the $\Delta\Sigma$ structure result in a noise composition that realistically resembles the experimental devices, in the rate in-band as well as in frequencies below and above. The major contributors for rate noise are in descending order: Voltage noise of the CV converter, voltage noise of the quadrature electrodes and Brownian motion of gas molecules acting on the sense mass. Noise influences from the drive as well as PLL phase noise are modeled to be negligibly small. Furthermore, the quantization noises as well as the dithers of the sense's $\Delta\Sigma$ ADC and DAC contribute less than one percent to the in-band noise around ω_{pll}, but form - facilitated by $\Delta\Sigma$ noise shaping - by far the largest noise share at frequencies left and right of the noise notch outside of the in-band. In this simulation the gyroscope's full-scale range is around ±300 dps and the digital bandwidth of the rate output, i.e. half the width of the in-band, is 100 Hz.

In an idealized case, the change of the force-feedback DAC bitstream to the sense ADC bitstream would contain the full spectral information of the sense mode. This view is untrue for a closed-loop system, however, because the plant input will be correlated in some way to the plant output through the feedback control, no matter the exact characteristic of the plant that is to be identified. System identification techniques for elements of a closed-loop system require particular care and are affiliated with significant limitations compared to regular, open-loop identification [182]. Nonetheless, simply treating a plant under closed-loop excitation as open-loop will oftentimes render acceptable results and therefore constitutes a legitimate approach, see [182] [183] [184].

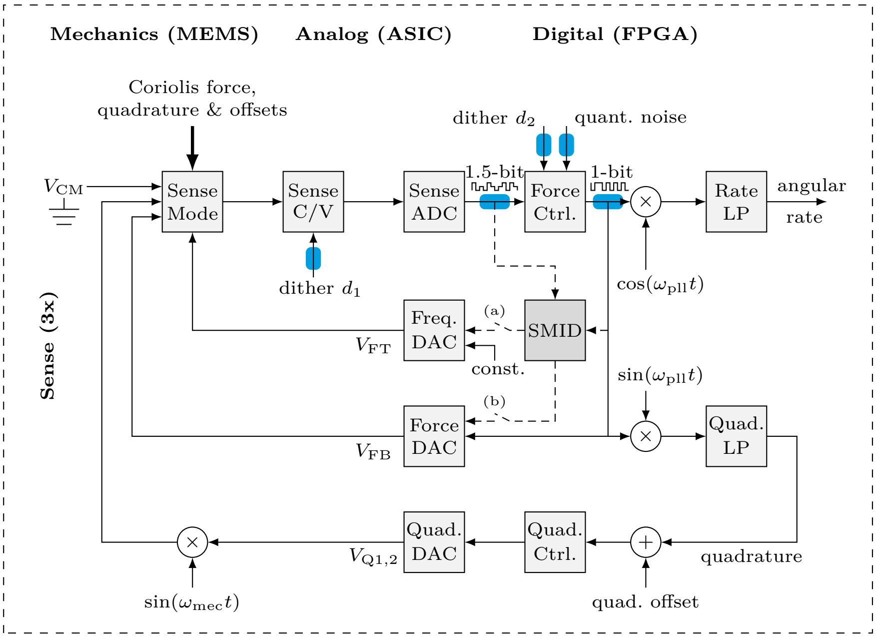

Figure 4.1.: *Top:* Gyroscope sense control structure as presented in Section 3.2. The drive control loops are omitted in this schematic. The resonance frequency and DC gain of the sense mode is to be estimated with the proposed SMID methods, using the known bitstreams (*blue*) of 1-bit force DAC and 1.5-bit sense ADC as well as the dither d_1 for exciting the ΔΣ ADC and the dither d_2 for the ΔΣ DAC within the force control block. Since the control is realized entirely in the digital domain, the quantization noise of the ΔΣ DAC is fully known. The SMID methods may output a detuning measure (a) that can be used to close a frequency-tuning control loop or a scale-factor measure (b) to close a scale-factor control loop by adjusting the force-feedback voltage.

Therefore, our first approach will examine the system identification in the open-loop point of view (SMID-OL), also called direct approach [182]. Since the feedback control at hand is entirely digital and therefore perfectly known to us, we will also construct a second, indirect [182] scheme (SMID-CL) that models the sense mode as part of the closed-loop, force-feedback control.

Another limitation regarding system identification of plants under closed-loop control is, that feedback systems typically aim at stabilizing the plant, i.e. reducing the plant's excitation, see [185]. Low excitation however stands in direct opposition to the needs of precise identification estimates. In our case, this notion is particularly true, because the excitation at the most relevant frequencies, i.e. the bottom of the noise notch, is the noise of the sensor output after demodulation. Sensor noise should of course always be as low as possible. The proposed methods will therefore have to rely on the stronger noise excitation further to the left and the right of the in-band, at the flanks of the noise notch.

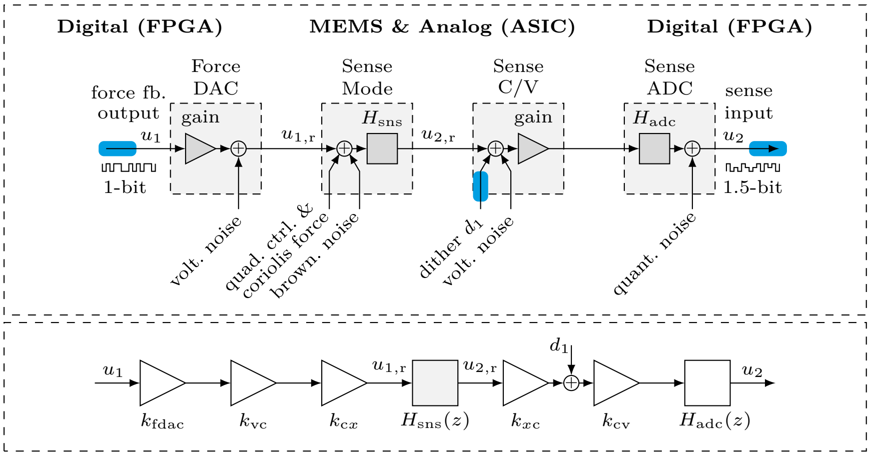

Figure 4.2.: Signal flow diagrams for SMID-OL. *Top:* Detailed view of unknown noise and signal disturbances acting on the sense mode with the only three known digital signals in blue. *Bottom:* Simplified view with gains and linear transfer functions.

In practice, a number of additional non-idealities and unknown disturbances exacerbate the extraction of the sense mode transfer function H_{sns} in both methods. Figure 4.2 includes a disturbance model of the signal path from force-feedback ΔΣ DAC bitstream to sense ΔΣ ADC bitstream. Voltage noise is inescapable when converting the digital LSB-value to a voltage inside the force DAC, alongside with the quadratic relationship of the voltage to force conversion, see equation (3.2). Furthermore, the quadrature control, offsets, the actual Coriolis force, as well as forces from Brownian motion acting on the sense mass influence the sense mode. The sense CV converter also inserts voltage noise. Quantization noise is added by the sense ΔΣ ADC and its transfer function alters the signal. A pseudo-random dither enters the CV front-end via switchable capacitor arrays to prevent toning in the ΔΣ ADC.

The core challenge is to acquire a precise frequency mismatch measure despite the presence of the listed influences. Merely the dither sequence, the gains of the DAC and CV front-end, and the transfer function of H_{ADC} are known. The SMID-OL method treats the signal $u_{1,\mathrm{r}}$ in Figure 4.2 as the open-loop input to H_{sns} and $u_{2,\mathrm{r}}$ as the output. Using the known signals and elements, the sense ADC bitstream can be rectified in z-transform notation with

$$U_{2,\mathrm{r}}(z) = k_{x\mathrm{c}}^{-1}\left(H_{\mathrm{adc}}^{-1}(z)k_{\mathrm{cv}}^{-1}U_2(z) - D_1(z)\right), \qquad (4.1)$$

where $U_2(z)$ is the sense ADC bitstream, $D_1(z)$ the ADC dither, k_{cv} the CV gain, $k_{x\mathrm{c}}$ the relationship of sense mode displacement to capacitance and $H_{\mathrm{ADC}}(z)$ the ADC transfer function. Under omission of unknown electrical CV noise and quantization, $U_{2,\mathrm{r}}(z)$ can be assumed as the output of the sense mode. The sense mode input $X_{\mathrm{r}}(z)$ is related to the force DAC bitstream $U_1(z)$ by

$$U_{1,\mathrm{r}}(z) = k_{\mathrm{c}x} k_{\mathrm{vc}} k_{\mathrm{fdac}} U_1(z). \tag{4.2}$$

where k_{fDAC} is the gain of the force-feedback DAC producing a constant positive or negative voltage according to the 1-bit bitstream, k_{vc} the voltage to capacitance and $k_{\mathrm{c}x}$ the capacitance to displacement relationship. The sense mode can then be estimated by providing input $U_{1,\mathrm{r}}(z)$ and output $U_{2,\mathrm{r}}(z)$ to a suitable system identification algorithm.

$$H_{\mathrm{sns,SMID\text{-}OL}}(z) = \frac{U_{2,\mathrm{r}}(z)}{U_{1,\mathrm{r}}(z)} = \frac{k_{\mathrm{xc}}^{-1} H_{\mathrm{adc}}^{-1}(z) k_{\mathrm{cv}}^{-1} U_2(z) - D_1(z)}{k_{\mathrm{cx}} k_{\mathrm{vc}} k_{\mathrm{fdac}} U_1(z)} \tag{4.3}$$

Simulation results of the spectra of the rectified signals $U_{1,\mathrm{r}}(z)$ and $U_{2,\mathrm{r}}(z)$ are displayed in Figure 4.3. The $\Delta\Sigma$ DAC force-feedback creates the typical noise notch at the drive frequency as the inverse of the sense mode, see equation (3.12). The low excitation of $H_{\mathrm{sns}}(z)$ at the resonance frequency becomes apparent.

The construction of the SMID-CL method is a bit more complex. First off, input signals to the closed-loop system need to be found and a suitable output selected. In our specific sensor implementation three input signals exist that are digitally known to us. There are two dither signals d_1 and d_2 which are essential for the correct and non-toning operation of the $\Delta\Sigma$ ADC and DAC converters. In a way, d_1 can be seen as a set-point excitation of the closed-loop control. Furthermore, the quantization noise that appears in the $\Delta\Sigma$ DAC is perfectly known, because everything happens in the digital domain, as opposed to the $\Delta\Sigma$ ADC, where the quantization noise cannot be known in the real device. The output of the $\Delta\Sigma$ DAC, y, i.e. the not-yet demodulated sensor output, has been selected as the output of the closed-loop transfer function. Figure 4.4 shows the closed-loop structure with additional disturbances. Note, that the $\Delta\Sigma$ DAC that generates the 1-bit bitstream is located inside the force control block. Within the force DAC block, those digital values are then simply translated directly to a stream of constant, positive and negative voltages V_{FB}.

The $\Delta\Sigma$ DAC requires further treatment. The non-linear quantizer can be modeled as a linear gain, whose value is determined by

$$k_{\mathrm{q}} = \frac{s^{\mathrm{T}} y}{s^{\mathrm{T}} s}, \tag{4.4}$$

see [186]. Here, s is the input to the quantizer and y the output. Note, that we do not use the typical $\Delta\Sigma$ notation as in [186]. It is important to remember, that the exact value may change by several percent depending on the signal and noise load of the quantizer. In principle, k_{q} may also be calculated and updated continuously within the SMID-CL scheme. Figure 4.4 shows a first-order $\Delta\Sigma$ for reasons of simplicity. The actual simulation uses a higher-order $\Delta\Sigma$, but the principle remains the same. Once the quantizer is linearized, the signal transfer

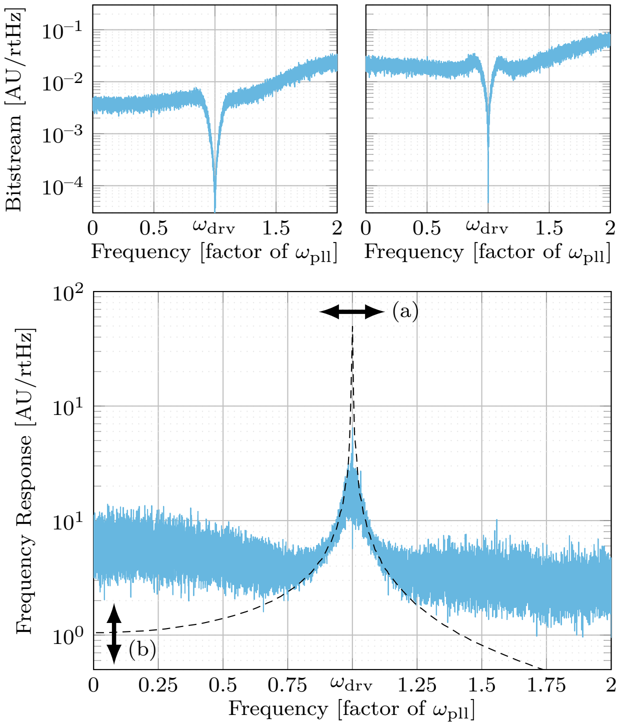

Figure 4.3.: *Top:* Spectral densities of rectified signals $u_{1,\mathrm{r}}$ (*left*) and $u_{2,\mathrm{r}}$ (*right*) from equation (4.3) of SMID-OL. *Bottom:* Frequency response function obtained from Matlab's `modalfrf()` from $u_{1,\mathrm{r}}$ to $u_{2,\mathrm{r}}$ (*light blue*) with the analytically calculated sense mode (*black, dashed*). The mode peak is well distinguishable from the quantization noise background. If the sense mode is detuned, the mode peak moves relative to ω_{pll} as symbolized by arrow (a). If the scale-factor changes, then the DC-gain moves, as indicated by arrow (b).

function (STF) from the $\Delta\Sigma$ input u to the output y, as well as noise transfer functions (NTF) from the dither d_2 and quantization noise q to the output y can be derived. One receives

$$H_{\mathrm{stf}} = \frac{Y(z)}{U(z)} = \frac{k_{\mathrm{q}} H_{\Delta\Sigma\text{-dac}}(z)}{1 + k_{\mathrm{q}} z^{-1} H_{\Delta\Sigma\text{-dac}}(z)} \approx \textit{const. i.b.i.} \tag{4.5}$$

$$H_{\mathrm{ntf},1} = \frac{Y(z)}{D_2(z)} = \frac{k_{\mathrm{q}}}{1 + k_{\mathrm{q}} z^{-1} H_{\Delta\Sigma\text{-dac}}(z)} \tag{4.6}$$

$$H_{\mathrm{ntf},2} = \frac{Y(z)}{Q(z)} = \frac{1}{1 + k_{\mathrm{q}} z^{-1} H_{\Delta\Sigma\text{-dac}}(z)}. \tag{4.7}$$

The importance of an accurate assessment of k_{q} becomes clear. The STF may be approximated as a linear gain in the band of interest, while the design of $H_{\Delta\Sigma\text{-dac}}(z)$ makes sure that the NTFs have a notch-shape, thereby pushing the noise away from the signal frequency [186]. In this band-pass $\Delta\Sigma$ configuration,

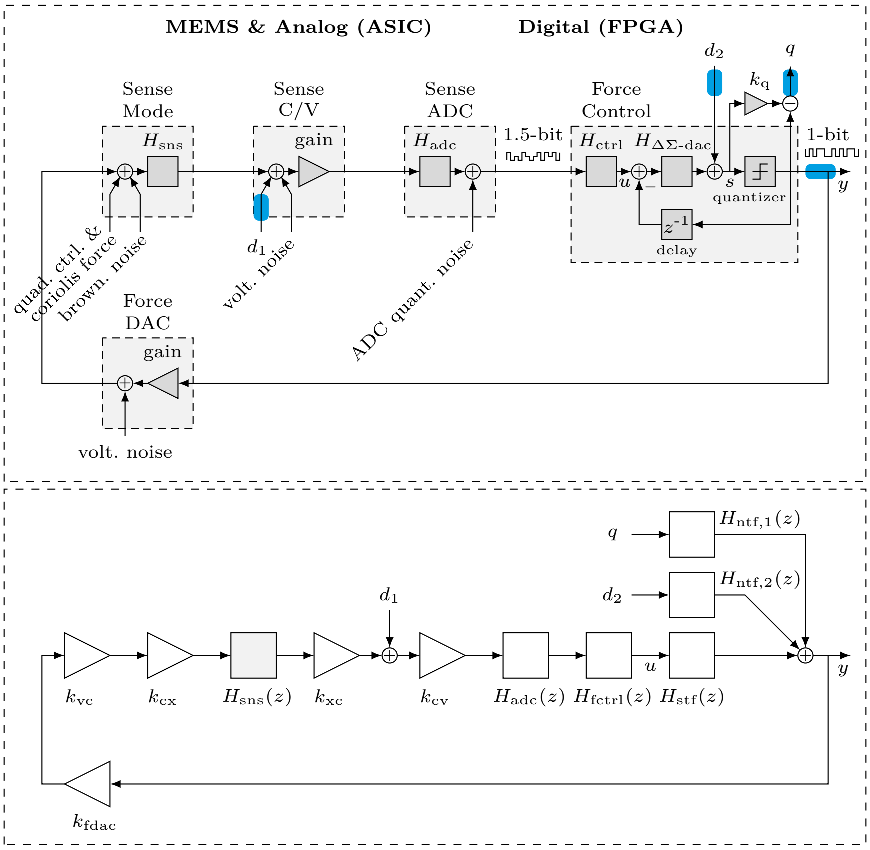

Figure 4.4.: Signal flow diagrams for SMID-CL. *Top:* Detailed view of unknown noise and signal disturbances acting on the sense mode with the three known input signals d_1, d_2, q and the output y in blue. The quantization noise appearing at the ΔΣ DAC 1-bit quantizer can be calculated by taking the difference of the signal before and after the quantizer under consideration of the linearized quantizer gain. *Bottom:* Simplified view with gains and linear transfer functions. The ΔΣ DAC has been partitioned into a signal transfer function $H_{\mathrm{stf}}(z)$ and two noise transfer functions $H_{\mathrm{ntf},1}(z)$ and $H_{\mathrm{ntf},2}(z)$.

the noise is shaped to higher *and* lower frequencies as shown e.g. in [28]. The closed-loop transfer function can now be compiled and the sense mode isolated so that one receives

$$H_{\mathrm{sns,SMID\text{-}CL}}(z) = \frac{U_2(z)}{U_1(z)} = \tag{4.8}$$
$$\frac{Y(z) - H_{\mathrm{ntf},1}(z)Q(z) - H_{\mathrm{ntf},2}(z)D_2(z) - H_{\mathrm{stf}}(z)H_{\mathrm{fctrl}}(z)H_{\mathrm{adc}}(z)k_{\mathrm{cv}}D_1(z)}{H_{\mathrm{stf}}(z)H_{\mathrm{fctrl}}(z)H_{\mathrm{adc}}(z)k_{\mathrm{cv}}k_{\mathrm{xc}}k_{\mathrm{vc}}k_{\mathrm{cx}}k_{\mathrm{fdac}}Y(z)}.$$

Here, $U_1(z)$ and $U_2(z)$ are the input and output signals presented to the system identification algorithm. Each are produced by the denominator and numerator of the transfer function, respectively.

]

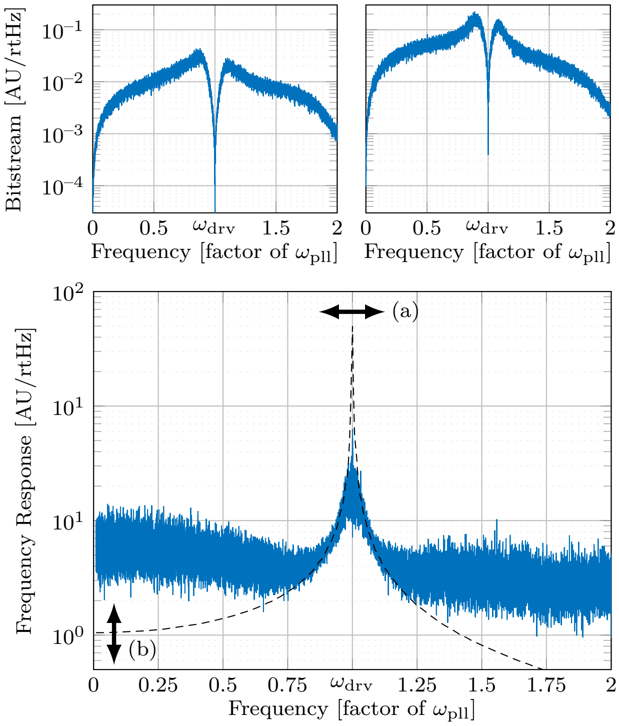

Figure 4.5.: *Top:* Spectral densities of signals u_1 (*left*) and u_2 (*right*) from equation (4.8) of SMID-CL. *Bottom:* Frequency response function obtained from Matlab's `modalfrf()` from u_1 to u_2 (*blue*) with the analytically calculated sense mode (*black, dashed*). The mode peak is well distinguishable from the quantization noise background. If the sense mode is detuned, the mode peak moves relative to ω_{pll} as symbolized by arrow (a). If the scale-factor changes, then the DC-gain moves, as indicated by arrow (b).

4.3. System Identification

The sense mode can be recovered by different means. One possibility is using Matlab's frequency response function for modal analysis, `modalfrf()` [187]. Figure 4.5 compares the resulting frequency response function of the SMID-CL method with the analytical transfer function of the sense mode modeled as a second-order mass-spring-damper system. Evidently, a reliable estimate is only attainable within close proximity of the drive frequency. Noise further off contains very little recoverable information about the sense mode, since it originates mainly from ADC quantization noise. Identical noise seeds for both simulations in Figures 4.3 and 4.5 have been used, so the quantization noise away from the peak look basically identical in both methods. The center of the frequency response peak is not accurately estimated, because of the unknown noise sources described above. If these are turned off, then the frequency response plot would have a peak as sharp as the analytical transfer function.

The modal analysis is helpful for visualization and it would in itself be a viable detuning measure. A time-domain approach is preferred however, because it does not require the elaborate calculation of frequency-domain spectra. A polynomial model estimation was therefore chosen. The past values of the rectified signals $u_{1,\mathrm{r}}$ and $u_{2,\mathrm{r}}$ for SMID-OL, or the closed-loop signals u_1 and u_2 for SMID-CL are saved within a buffer for 250 ms. The SMID measure's update rate is thus 4 Hz. These datasets are sufficient to compute a reliable estimate of the sense mode. The output-error (oe) estimation structure [182] [188]

$$y'(t) = \frac{B(q)}{F(q)} x'(t - n_k) + e(t) \tag{4.9}$$

was found to be suited best over the course of numerous different implementations. Other AR(MA)X or Box-Jenkins models are also feasible, but did not give quite the same performance and had longer computation times. Prediction-error estimation (pem) with a gray-box model of the sense mode was found to be similar to the output-error estimation in performance and may be used as well. Within the output-error estimation, an iterative Gauss-Newton (gn) search solves the nonlinear least-square minimization problem. A weighting filter allows only information in the vicinity of ω_{pll} to be considered. Table 4.1 includes more details on the parametrization of the output-error function.

4.4. Simulation Results

The effectiveness and precision of the detuning and scale-factor measures of the proposed SMID-OL and SMID-CL methods are analyzed in simulation in this section. The frequency tuning and scale-factor control loops seen in Figure 4.1 were *not* closed for this examination. As a comparison for the detuning measure, the pilot tone (PT) method was also simulated. Figure 4.6 shows separate simulation runs at different detuning voltages ΔV_{FT} for detuning estimation and at different feedback voltage changes $\Delta \mathrm{V}_{\mathrm{FB}}$ for scale-factor estimation. In both cases and for both open-loop and closed-loop methods, the measure resembles the actual analytical values well. The constant offset of the pilot tone output can also be observed, as predicted by Section A.9 in the appendix.

Table 4.1.: Properties of Matlab's output-error estimation function `oe()` used for the simulations shown in Figures 4.6, 4.7 and 4.8.

Specification	Value
Regularization	none
Initial condition	'zero'
Weighting filter	$\omega_{\mathrm{pll}} \pm 6$ kHz

Specification	Value
Focus	'simulation'
Search method	'gn'
Model order	[2 2 1]

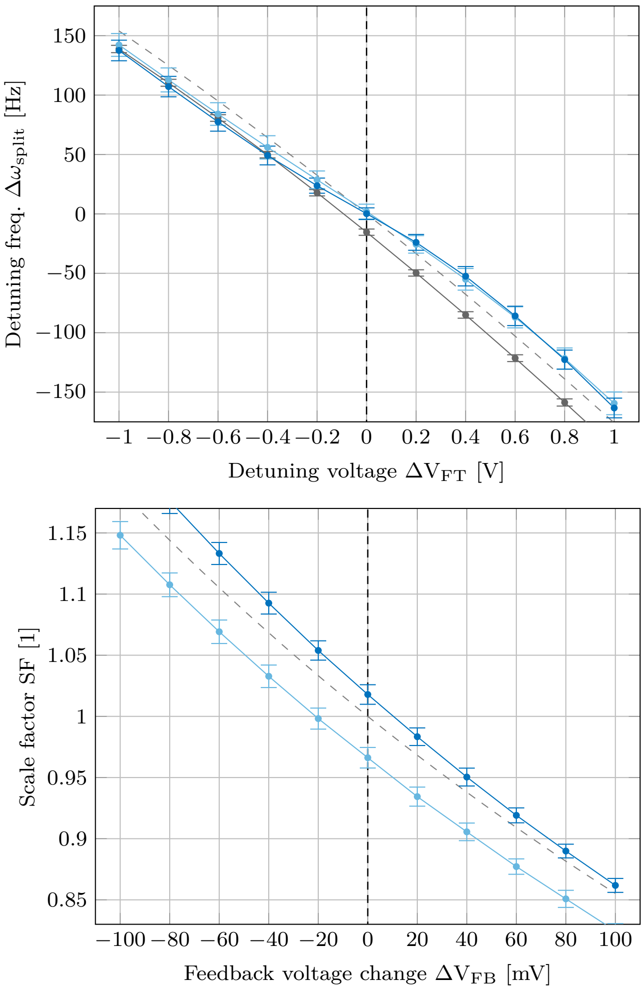

Figure 4.6.: *Top:* Simulation of detuning measure with pilot tone (*gray*), SMID-OL (*light blue*) and SMID-CL (*blue*) methods. The gray, dashed line marks the actual, analytical detuning of the sense mode and the vertical black line perfect mode-matching at $\Delta V_{\text{FT}} = 0\,V$. Error bars show the 1-$\sigma$ standard deviation during a 60 s simulation run for each data point. *Bottom:* Simulation of scale-factor measure with SMID-OL (*light blue*) and SMID-CL methods (*blue*). The gray, dashed line marks the actual, analytical scale-factor of the sensor and the vertical black line the undisturbed scale-factor of 1. Error bars mark the 1-σ standard deviation during a 60 s simulation run for each data point.

Indicated by the 1σ-error bars, the SMID-OL and SMID-CL readout has a much higher noise compared to the pilot tone measure. The SMID scale-factor measures need some offset adjustments but are otherwise of about the same slope as the actual scale-factor change. In contrast, both SMID detuning measures show some additional non-linearity that was found to originate mostly from the unknown CV converter voltage noise.

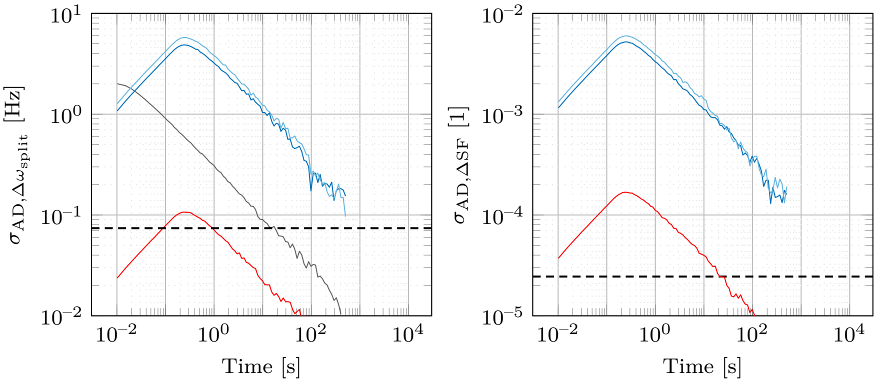

Figure 4.7.: *Left:* Comparison by Allan deviation of pilot tone (*gray*), SMID-OL (*light blue*) and SMID-CL (*blue*) methods for detuning estimation. The dashed, horizontal line marks the effect of typical frequency tuning voltage flicker noise (here: 380 μV/rtHz) on detuning frequency $\Delta\omega_{\mathrm{split}}$. *Right:* Comparison by Allan deviation of SMID-OL (*light blue*) and SMID-CL (*blue*) methods for scale-factor estimation in terms of difference ΔSF to the ideal scale factor of 1. The dashed, horizontal line marks the effect of typical feedback voltage flicker noise (here: 13 μV/rtHz) in the form of scale-factor instability. The SMID-CL results using an ARX model with just the ΔΣ force-feedback DAC and dither d_2 active, all non-idealities and noise sources deactivated, is shown in red. Simulation time for all methods was one hour.

The noise level of both SMID methods for detuning and scale-factor estimation is examined by Allan deviation in Figure 4.7. The bumps at 0.25 s appear because the measures' update rate is 4 Hz. It is found that all measures contain white noise for larger cluster times. Therefore, the longer the measurement period, the more precisely the underlying, true detuning frequency or scale-factor can be determined. Note, that the Allan deviation is in units of Hz for detuning estimation and unitless for scale-factor estimation. For actual compensation of flicker noise on the frequency tuning or feedback voltage, the estimate must be more precise than the influence of flicker on detuning or scale-factor. The averaging time from which on forward closed-loop frequency tuning or scale-factor control actually improves the flicker noise effect is thus the intersection of the white noise slope with the horizontal flicker level, which is modeled here to be 380 μV/rtHz for the frequency tuning voltage and 13 μV/rtHz for the feedback voltage. The pilot tone method intersects the horizontal flicker level at about 15 s, meaning a bias instability compensation as shown in the previous chapter in Figure 3.7 is possible on time scales of 15 s and longer. The white noise levels of the SMID-OL and SMID-CL methods are similar and much higher than that of the pilot tones. Their intersection with the horizontal flicker level occurs at above 2000 s. Both methods are therefore not noise-free enough to allow practical usage of a closed-loop frequency tuning control. For the

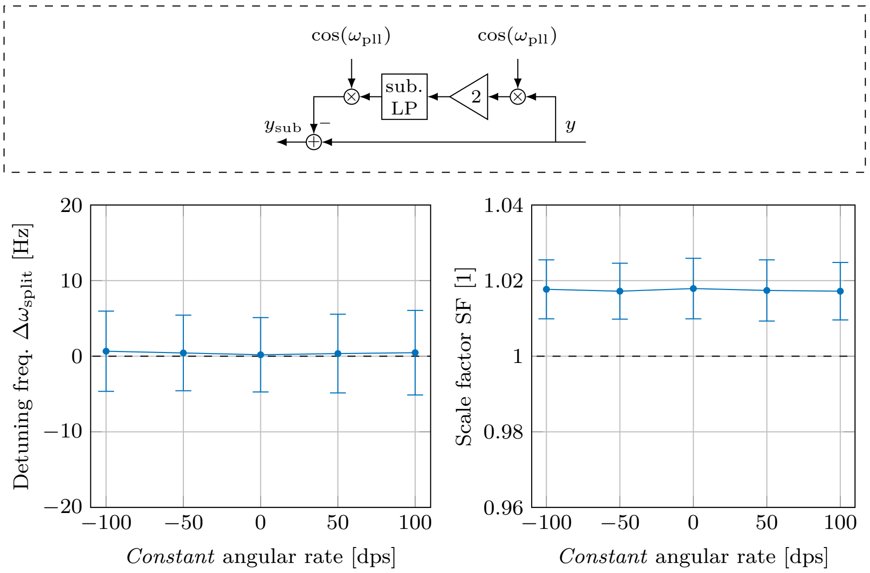

Figure 4.8.: *Top:* In-band, rate-phase signal removal by demodulation, low-pass (LP) filtering, modulation and subtraction from the original signal. *Bottom:* Invariance of the SMID-CL frequency detuning (*left*) and scale-factor (*right*) measures at the ideal operating point, see Figure 4.6, to constant angular rate.

scale-factor estimation the intersection is at even longer time scales, around 10000 s. Compensating scale-factor instability using the presented methods is thus out of the question. As a sanity check, all modeled non-idealities and noise sources except the force-feedback ΔΣ DAC and its dither d_2 were turned off in the simulation. The best performing method was found to be SMID-CL employing an ARX model, as shown with the red entries in Figure 4.7.

Table 4.2.: Performance of the SMID methods for detuning and scale-factor estimation in comparison to the pilot tones (PT), as well as their intersection with the tuning voltage and feedback voltage flicker noise level from Table 3.6.

FT Meas.	$\sigma_{\mathbf{AD},\Delta\omega_{\mathbf{split}}}\|_{\tau_{\mathbf{AD}}=1s}$	$\sigma_{\mathbf{AD},\Delta\omega_{\mathbf{split}}}\|_{\tau_{\mathbf{AD}}=10s}$	**Intersec. w/ flicker**
Units	[Hz]	[Hz]	[s]
PT	0.31	0.09	15
SMID-OL	3.8	1.2	ca. 2000
SMID-CL	3.2	1.0	ca. 2000
SF Meas.	$\sigma_{\mathbf{AD},\Delta\mathbf{SF}}\|_{\tau_{\mathbf{AD}}=1s}$	$\sigma_{\mathbf{AD},\Delta\mathbf{SF}}\|_{\tau_{\mathbf{AD}}=10s}$	**Intersec. w/ flicker**
Units	[%]	[%]	[s]
SMID-OL	0.39	0.14	ca. 10000
SMID-CL	0.33	0.11	ca. 10000

Then, the measure was precise enough to - in principle - allow a closed-loop compensation of bias instability and scale-factor instability. It was therefore demonstrated, that the presence of non-idealities and unknown noise is what prevents the methods from performing better. Even though the two SMID methods in the presence of non-idealities and unknown noise sources might not be precise enough to improve the flicker influence, the SMID-CL measure can nonetheless estimate the detuning frequency to a remarkable precision of $\sigma_{\mathrm{AD},\Delta\omega_{\mathrm{split}}} = 3.2\,\mathrm{Hz}$ and scale-factor to $\sigma_{\mathrm{AD},\Delta\mathrm{SF}} = 0.33\,\%$ within 1 s. Table 4.2 summarizes the performance of the examined methods.

The presented disturbances in Figures 4.2 and 4.4 are assumed to be mostly static, so if they should induce an offset in the SMID measure, it may be calibrated out. That is not true for the actually applied angular rate, however. Since the signal strength from applied angular rate exceeds the employed noise in the method by far, it would render the SMID method defunct if not treated properly. The same would be true for quadrature, however the quadrature control already suppresses any signal in quadrature-phase in the in-band. Figure 4.8 shows one possible approach for the SMID-CL method to render the estimation algorithms invariant to applied angular rate. The in-band, rate-phase signal is removed from the sensor output y before equation (4.8) is applied. After demodulating and receiving the angular rate signal with a certain bandwidth though a low-pass, it is again modulated onto the same carrier ω_{pll} and then subtracted from the original signal. Figure 4.8 shows that offset and noise of the SMID-CL method change only slightly when large, constant angular rates are applied. However, severe limitations of this approach emerge when angular rates with even low frequencies are applied. The subtraction low-pass needs to be limited to roughly the typical in-band width of the sensor, e.g. 200 Hz so as to leave some noise for the SMID methods to work with. At the same time it is not possible to design a low-pass filter with equally flat amplitude *and* phase response up to the corner frequency. A discussion of further limitations, a summary and an outlook are provided in the following.

4.5. Discussion

Concluding this chapter, it is found that estimating the natural frequency and the DC-gain of the sense mode purely by the already-existing noise from quantization and $\Delta\Sigma$ dithers in the force-feedback loop is possible. However, several challenges arose in this investigation, which prevented the novel SMID-OL and SMID-CL measures from reaching precisions comparable to the pilot tone scheme. Firstly, the region of interest around the drive frequency is also the one excited by the least amount of noise at the bottom of the $\Delta\Sigma$ notch, because that is where angular rate is measured and low noise is imperative. Secondly, the control complexity might not have been high enough at the frequencies of interest, see Table 4.2, even when the control design had more complexity overall at other frequencies compared to the simple mass-spring-damper model of the sense mode. Lastly and most importantly is the plurality of disturbing noise sources and non-idealities, as well as their diverse entry points into the closed-loop system, which are challenging to adequately represent by simple polynomial models. In practice, some transfer functions and gains will also not behave ideally, like the CV gain, which will change with temperature.

When all “unknown” noise sources and non-linearities were turned off in the simulation, an ARX model within SMID-CL provided precisions for detuning about 40 times better and for scale-factor estimation about 30 times better than in the regular case. With this perfect system, compensating flicker noise on tuning and feedback voltage would be possible in simulation, but of course of little relevance for an experimental device.

A further way of reducing the noise of the SMID estimates is to inject tones to excite the closed-loop system more. That would however undermine the goal of designing a tone-free method and one might as well just use the much simpler pilot tones then. Complexity is also a further issue that the SMID approaches face. A lot of effort would be necessary to reduce the computation load of the polynomial estimation algorithms down to a level where they could be implemented on a sensor chip and provide results in real-time. More limitations for truly continuous estimation exist in the presence of higher-frequency applied angular rate, as described above.

External vibration on the sensor, appearing as a peak in the output spectrum of y, is also handled poorly by the SMID methods. There, robustness has been found to be much worse than what erroneous signal the pilot tones would generate if the vibration coincided directly with one tone frequency. At least, the SMID methods are able to output a covariance measure alongside with their estimate, warning about strong disturbances in the event of external vibration on the sensor.

On the plus side, the novel methods feature a large capture range, i.e. they can identify even large frequency splits, and may be used for a variety of different sensor implementations e.g. with regard to quality factors, loop gain or feedback control designs. Even though flicker noise compensation was shown not to be feasible, the SMID methods may be used for factory calibration of a fixed tuning value, as absolute accuracy is not as much of a concern there. It may also find use in a much slower frequency tuning or scale-factor control scheme that aims at compensating temperature or stress influences as well as aging effects instead of flicker noise.

In this chapter, a lack of scientific publications on tone-free methods for measuring detuning or scale-factor was found. The developed SMID methods represent one of many possible approaches to this topic. Only the existing quantization noise and $\Delta\Sigma$ dithers were used. Other sensor implementations may not use dither signals and similar methods may therefore have to rely solely on the known output quantization noise. Closed-loop system identification proved to be challenging with the indirect SMID-CL method performing moderately better than the direct SMID-OL method. The third possibility of a joint input-output approach as described in [182] was not investigated. Possibly, other methods than polynomial model system identification may bring further improvement to precision or lower computational effort. Methods similar to the ones in this chapter might be used more successfully on sensors where there is one dominant disturbance source as opposed to many, roughly equally contributing sources.

5. Conclusion

In this chapter, the dissertation findings are summarized and reflected. The author's contribution in relation to the existing state-of-the-art is delineated. Lastly, prospects for future work on related topics are illustrated.

5.1. Dissertation Summary

High and fully automated vehicles will transform individual mobility as we know it. The first chapter outlined the current state of discourse and the classification of vehicle automation in six levels. For public roads, level 2 - partial automation in *both* the longitudinal and lateral motion - is at least in a legal sense to date the highest level offered by major car manufacturers. The fallback responsibility in level 3 automated driving is placed on the driver. However, humans performs notoriously poorly when tasked with complex situation assessment after long durations of mental absence. Manufacturers may therefore move straight to level 4 and 5, where the vehicle is responsible for bringing itself into a minimal risk condition, should the system's automated driving capability deteriorate. That condition is typically an emergency stop maneuver, which was chosen in this dissertation as an exemplary use-case for inertial sensors in automated vehicles. The previous achievements of MEMS inertial sensors in automotive applications like electronic stability control were presented and performance-limiting deterministic and stochastic error effects were discussed. Bias instability noise was identified as a key performance parameter in literature.

The second chapter dealt in detail with the influences of sensor noise on inertial navigation under omission of any possible deterministic error sources. Allan deviation was elucidated as the primal method to differentiate between noise types in MEMS gyroscopes or accelerometers. Out of the many noise types, angle random walk, which is white noise, and bias instability were found to be both typically present in the sensor signals and relevant for navigation precision. In a strap-down mechanism, the gyroscopes' signals are integrated once for relative attitude and thrice for relative position. Analytical descriptions of the accumulating sensor error for angle random walk and bias instability were derived and visualized using realistic noise parameters. It was found that although bias instability is typically portrayed as a long-term effect, its error influence surpasses that of angle random walk as early as five seconds of integration time for attitude and ten seconds for position. The results were corroborated by iterative simulations of two emergency stop maneuver scenarios. It was established, that in order to reach a viable 3-sigma end-point precision for these maneuvers, the amount of angle random walk and bias instability needed to be reduced considerably, compared to what was assumed as typical MEMS gyroscope performance.

Chapter 3 delved deep into the inner workings of triaxial MEMS gyroscopes operated in mode-matched and force-feedback configuration. An in-depth state of the art revealed, that although some methods of improving bias instability have been demonstrated in the past, the underlying origins and mechanism of bias instability were yet unknown. Using a model-based simulation approach, different offset effects that were reported in literature were combined with flicker noise on the sensor's control voltages. Certain types of offset, that did not pass the sense mode, but enter at the capacitance-voltage converter, were demonstrated to produce bias instability. Necessary condition was the presence of flicker noise on the frequency tuning voltage which electrostatically softens the sense mode, ensuring mode-matching to the drive mode. Formulas were derived from which the bias instability component of each of the sensor's control voltage could be calculated. Agreement between the simulation results and extensive measurements on triaxial, future-generation, automotive MEMS gyroscopes was demonstrated. In order to compensate bias instability, the frequency detuning was measured with pilot tones and continuously compensated in a feedback control loop. A factor ten improvement in both simulation and experiment was demonstrated and bias instabilities of lower than 0.1 dph were reached. The newly-discovered effect is superimposed by another, unknown source of bias instability for the two out-of-plane sensing axes. The unknown effect could not be resolved within the creation of the dissertation. Active frequency tuning control did therefore not improve the out-of-plane sensing axes. While examining the unknown contribution, a further drift effect was discovered and termed scale-factor instability. Since the voltage stage of the force-feedback DAC determines the scale-factor, any flicker noise on this voltage will create small variation in sensitivity. It was demonstrated, that for use-cases where high angular rates are common, this effect will surpass the drift induced by bias instability.

In the fourth chapter, a simulation study was conducted to develop a novel method that can potentially replace the pilot tone scheme and estimate scale-factor instability at the same time. The pilot tones offer high signal-to-noise ratios when measuring frequency detuning. However, they inject additional tones into the control structure that are challenging to remove from the rate output. They are furthermore susceptible to external vibrations if those happen to coincide with the pilot tones. The novel method aims at continuously estimating the sense mode's resonance frequency and DC gain by using solely the existing noise in the force-feedback $\Delta\Sigma$ control. The novel method was shown to be feasible, but was accompanied by too much measurement noise. A compensation of flicker noise on the tuning and feedback voltages was therefore not possible.

5.2. Author Contributions

This section distinguishes the contributions of the author from the existing state of the art. Although bias instability was formally described as a noise type by Allan, it was commonly not regarded as one in many inertial MEMS publications. Instead it is oftentimes seen only as the minimum-point between angle and rate random walk. Moreover, the role of the latter was frequently overemphasized, when it was in fact caused only by non-ideal measurement setups with larger temperature gradients. The author demonstrated, that the Allan deviation curve consists almost entirely of angle random walk and a horizontal bias instability component, when good care is taken in the experiments.

Bias instability was sometimes modeled as Markov noise at certain frequency bands, leading to vastly different results in the navigation precision prediction. This dissertation demonstrated that a constant 1/f noise over all frequencies exists, with flicker noise at its origin. The different behavior in integration of bias instability, growing approximately linearly in time, versus the angle random walk's square-root of time growth, was not commonly known before. Particularly the short time span until bias instability becomes dominant in integration above angle random walk was not considered. While equation (2.21) was published in [30] recently, the actual analytical description was provided in Section A.3 for the first time. To the knowledge of the author, bias instability influences on emergency stop maneuvers have not been publicized before. The distinction between deterministic errors like temperature gradients and stochastic errors like bias instability noise was also seldom drawn.

The literature review revealed a number of successful efforts to reduce bias instability in MEMS gyroscopes, but no detailed understanding. An improvement by frequency tuning control had been shown in [143] on the same conference than the author's first contribution [1]. Scientific knowledge was advanced by the in-depth explanation of origins and mechanisms of bias instability in all of Chapter 3. Especially the control voltage variation, the calculation of the resulting bias instability in equation (3.32) and the methodical experimental approach as in Table 3.9 will be useful for other researchers, along with the new understanding of the role of different types of rate offsets. The discovery and explanation of scale-factor instability in force-feedback MEMS gyroscopes is entirely novel, as far as the author is aware of. The findings are important for applications where high angular rates are common, because there scale-factor instability will create drifts much higher than bias instability.

Lastly, the SMID algorithm consequently promoted the state of the art by not relying on injected signals like others have before, but by employing only the existing noise within the control architecture.

The ultra-low angle random walk of the presented devices also bears novelty, but is not credited to the author, as he was not involved with the actual MEMS and ASIC design and fabrication. It shall also be noted, that the modeling of offset sources and flicker noise was the author's, along with all of the analysis work, but that the transfer functions for the control elements and filters were taken from existing models at Robert Bosch GmbH.

5.3. Future Prospects

The dissertation's results give rise to a number of questions that may be investigated in the future. This work assumed purely inertial navigation during emergency stop maneuvers. The inclusion of wheel speed and steering angle sensors (odometry) and their non-idealities and noise might bring about additional requirements for the inertial sensors. Another research area would be the interaction of inertial sensors with GNSS signals in cases of alternating low and high vehicle dynamics, which is not optimally solved by the classical Kalman filter approach in the opinion of the author, compare also with [189]. With the availability of highly precise MEMS inertial sensors, the efficiency or energy consumption of tight coupling GNSS receivers may be optimized, because longer navigation durations can be bridged without a GNSS position fix. Fixes may also be found quicker.

Another topic that seems promising to the author is optimized navigation in a two-dimensional plane, like a factory floor or shopping center. Many highly-relevant use cases do not require full, three-dimensional navigation. Relative navigation might be rendered long-term stable by optical sensors performing visual-inertial odometry, which would sidestep the need for triple integration of the gyroscope signal within a full strap-down mechanism.

Concerning bias instability, the origins of the unknown components in the out-of-plane sensing axes are still open for further investigation. Since open-loop gyroscopes typically have a mode-split of several hundred Hz, the question arises if bias instability in these devices is also related to frequency tuning of the sense mode. In any case, keeping the mode split constant will likely be beneficial for temperature and stress induced drifts, so methods similar to the pilot tones may be developed for open-loop devices. Scale-factor instability may be removed by some form of continuous scale-factor estimation mechanism. The next steps for the SMID algorithm could include optimization for operation on sensor-internal integrated circuits or optimization of the precision of the estimate. In a similar way, other non-idealities within the sensor could be estimated continuously.

Sensor redundancy, primarily by low-price, consumer-type MEMS inertial sensors, was examined by some of the supervised students. Section A.6 of the appendix gives an overview of their findings. Optimal fusion of MEMS gyroscopes during external vibrations was examined within our group [190]. A number of continuative research questions remains, like possible cancellation of PCB stress effects, estimation of misalignments and scale-factor errors or a framework for fusing signals with different group and phase delays.

Bibliography

[1] T. Hiller, B. Kuhlmann, A. Buhmann, and H. Roth, "Noise contributions in a closed-loop MEMS gyroscope for automotive applications," in *IEEE International Symposium on Inertial Sensors and Systems*. IEEE, March 2017, pp. 62–65.

[2] T. Hiller, Z. Pentek, J.-T. Liewald, A. Buhmann, and H. Roth, "Origins and mechanisms of bias instability noise in a three-axis mode-matched MEMS gyroscope," *IEEE Journal of Microelectromechanical Systems*, vol. 28, no. 4, pp. 586–596, Aug. 2019.

[3] J. Van Brummelen, M. O'Brien, D. Gruyer, and H. Najjaran, "Autonomous vehicle perception: The technology of today and tomorrow," *Transportation research part C: Emerging technologies*, vol. 89, pp. 384–406, 2018.

[4] National Highway Traffic Safety Administration, "Preliminary statement of policy concerning automated vehicles," National Highway Traffic Safety Administration, Tech. Rep., 2013.

[5] S. Parida, M. Franz, S. Abanteriba, and S. Mallavarapu, "Autonomous driving cars: Future prospects, obstacles, user acceptance and public opinion," in *International Conference on Applied Human Factors and Ergonomics*. Springer, 2018, pp. 318–328.

[6] W. Brenner and A. Herrmann, "An overview of technology, benefits and impact of automated and autonomous driving on the automotive industry," in *Digital Marketplaces Unleashed*. Springer, 2018, pp. 427–442.

[7] S. Singh, "Critical reasons for crashes investigated in the national motor vehicle crash causation survey," National Highway Traffic Safety Administration, Tech. Rep., 2015.

[8] World Health Organization, *Global status report on road safety 2018*. WHO, 2018.

[9] SAE international, "Taxonomy and definitions for terms related to driving automation systems for on-road motor vehicles," *SAE Standard J3016*, 2016.

[10] T. M. Gasser, C. Arzt, M. Ayoubi, A. Bartels, L. Bürkle, J. Eier, F. Flemisch, D. Häcker, T. Hesse, W. Huber *et al.*, "Rechtsfolgen

zunehmender Fahrzeugautomatisierung," *Berichte der Bundesanstalt für Straßenwesen. Unterreihe Fahrzeugtechnik*, no. 83, 2012.

[11] N. Merat, H. Jamson, F. Lai, and O. Carsten, "Automated driving, secondary task performance and situation awareness," *Human Factors: A system view of human, technology, and organisation*, pp. 41–53, 2010.

[12] V. A. Banks, A. Eriksson, J. O'Donoghue, and N. A. Stanton, "Is partially automated driving a bad idea? Observations from an on-road study," *Applied Ergonomics*, vol. 68, pp. 138–145, 2018.

[13] S. M. Casner, E. L. Hutchins, and D. Norman, "The challenges of partially automated driving," *Communications of the ACM, 59(5)*, 2016.

[14] K. Zeeb, A. Buchner, and M. Schrauf, "What determines the take-over time? An integrated model approach of driver take-over after automated driving," *Accident Analysis & Prevention*, vol. 78, pp. 212–221, 2015.

[15] P. Bigelow, "Why level 3 automated technology has failed to take hold," July 2019. Accessed on: Jan. 2020. [Online]. Available: https://www.autonews.com/shift/why-level-3-automated-technology-has-failed-take-hold

[16] T. Raste, "Fallback strategy for automated driving using STPA," *3rd European STAMP Workshop, Amsterdam*, 2015.

[17] M. Aeberhard, S. Rauch, M. Bahram, G. Tanzmeister, J. Thomas, Y. Pilat, F. Homm, W. Huber, and N. Kaempchen, "Experience, results and lessons learned from automated driving on Germany's highways," *IEEE Intelligent Transportation Systems Magazine*, vol. 7, no. 1, pp. 42–57, 2015.

[18] J. Becker, S. Kammel, O. Pink, and M. Fausten, "Bosch's approach toward automated driving," *at-Automatisierungstechnik*, vol. 63, no. 3, pp. 180–190, 2015.

[19] J. Weber and F. Kröger, "Introduction: Autonomous driving and the transformation of car cultures," *Transfers Interdisciplinary Journal of Mobility Studies*, vol. 8, no. 1, pp. 15–23, 2018.

[20] G. Dixon, P. S. Hart, C. Clarke, N. H. O'Donnell, and J. Hmielowski, "What drives support for self-driving car technology in the United States?" *Journal of Risk Research*, pp. 1–13, 2018.

[21] M. Maurer, J. C. Gerdes, B. Lenz, H. Winner *et al.*, *Autonomous driving - Technical, Legal and Social Aspects.* Springer Open, 2016.

[22] K. Heineke, P. Kampshoff, A. Mkrtchyan, and E. Shao, "Self-driving car technology: When will the robots hit the road?" McKinsey Global Institute, Tech. Rep., 2017.

[23] R. P. D. Vivacqua, M. Bertozzi, P. Cerri, F. N. Martins, and R. F. Vassallo, "Self-localization based on visual lane marking maps: An accurate low-cost approach for autonomous driving," *IEEE Transactions on Intelligent Transportation Systems*, vol. 19, no. 2, pp. 582–597, 2018.

[24] Z. Sun, G. Bebis, and R. Miller, "On-road vehicle detection: A review," *IEEE Transactions on Pattern Analysis & Machine Intelligence*, no. 5, pp. 694–711, 2006.

[25] M. S. Grewal, L. R. Weill, and A. P. Andrews, *Global positioning systems, inertial navigation, and integration.* John Wiley & Sons, 2007.

[26] M. Barjenbruch, D. Kellner, K. Dietmayer, J. Klappstein, and J. Dickmann, "A method for interference cancellation in automotive radar," in *2015 IEEE MTT-S International Conference on Microwaves for Intelligent Mobility (ICMIM).* IEEE, 2015, pp. 1–4.

[27] E. T. Benser, "Trends in inertial sensors and applications," in *IEEE International Symposium on Inertial Sensors and Systems 2015.* IEEE, 2015, pp. 1–4.

[28] G. K. Balachandran, V. P. Petkov, T. Mayer, and T. Balslink, "A 3-axis gyroscope for electronic stability control with continuous self-test," *IEEE Journal of Solid-State Circuits*, vol. 51, no. 1, pp. 177–186, 2016.

[29] R. Neul, U.-M. Gómez, K. Kehr, W. Bauer, J. Classen, C. Doring, E. Esch, S. Gotz, J. Hauer, B. Kuhlmann *et al.*, "Micromachined angular rate sensors for automotive applications," *IEEE Sensors Journal*, vol. 7, no. 2, pp. 302–309, 2007.

[30] I. P. Prikhodko, B. Bearss, C. Merritt, J. Bergeron, and C. Blackmer, "Towards self-navigating cars using MEMS IMU: Challenges and opportunities," in *IEEE International Symposium on Inertial Sensors and Systems 2018.* IEEE, 2018.

[31] A. Mikov, A. Panyov, V. Kosyanchuk, and I. Prikhodko, "Sensor fusion for land vehicle localization using inertial MEMS and odometry," in *IEEE International Symposium on Inertial Sensors and Systems 2019.* IEEE, 2019, pp. 45–46.

[32] D. K. Shaeffer, "MEMS inertial sensors: A tutorial overview," *IEEE Communications Magazine*, vol. 51, no. 4, pp. 100–109, 2013.

[33] S. D. Senturia, *Microsystem design.* Springer Science & Business Media, 2007.

[34] W. Geiger, J. Bartholomeyczik, U. Breng, W. Gutmann, M. Hafen, E. Handrich, M. Huber, A. Jackle, U. Kempfer, H. Kopmann *et al.*, "MEMS IMU

for AHRS applications," in *Position, Location and Navigation Symposium, 2008 IEEE/ION.* IEEE, 2008, pp. 225–231.

[35] F. Laermer, A. Schilp, K. Funk, and M. Offenberg, "Bosch deep silicon etching: Improving uniformity and etch rate for advanced MEMS applications," in *Twelfth IEEE International Conference on Micro Electro Mechanical Systems.* IEEE, 1999, pp. 211–216.

[36] F. Laermer, S. Franssila, L. Sainiemi, and K. Kolari, "Deep reactive ion etching," in *Handbook of Silicon Based MEMS Materials and Technologiesw.* Elsevier, 2015, pp. 444–469.

[37] S. A. Campbell, *Fabrication Engineering at the Micro-and Nanoscale (Third Edition).* Oxford University Press Oxford, 2008.

[38] A. M. Shkel, "Precision navigation and timing enabled by microtechnology: Are we there yet?" in *SPIE Defense, Security, and Sensing.* International Society for Optics and Photonics, 2011, pp. 803 118–803 118.

[39] G. T. Schmidt, "INS/GPS technology trends," DTIC Document, Tech. Rep., 2010.

[40] KVH industries, "Guide to comparing gyro and IMU technologies," 2014.

[41] V. Passaro, A. Cuccovillo, L. Vaiani, M. De Carlo, and C. E. Campanella, "Gyroscope technology and applications: A review in the industrial perspective," *MDPI Sensors*, vol. 17, no. 10, p. 2284, 2017.

[42] P. B. Ruffin, "Progress in the development of gyroscopes for use in tactical weapon systems," in *SPIE's 7th Annual International Symposium on Smart Structures and Materials.* International Society for Optics and Photonics, 2000, pp. 2–12.

[43] N. El-Sheimy and A. Youssef, "Inertial sensors technologies for navigation applications: State of the art and future trends," *Satellite Navigation*, vol. 1, no. 1, p. 2, 2020.

[44] C. Goodall, S. Carmichael, and B. Scannell, "The battle between MEMS and FOGs for precision guidance," *Analog Devices Technical Article MS-2432*, 2013.

[45] H. Martin, P. Groves, and M. Newman, "The limits of in-run calibration of MEMS inertial sensors and sensor arrays," *NAVIGATION: Journal of The Institute of Navigation*, vol. 63, no. 2, pp. 127–143, 2016.

[46] J. Hidalgo-Carrió, S. Arnold, and P. Poulakis, "On the design of attitude-heading reference systems using the Allan variance," *IEEE Transactions on Ultrasonics, Ferroelectrics, and Frequency Control*, vol. 63, no. 4, pp. 656–665, 2016.

[47] E. Hinueber, “If you want to use an inertial measurement system,” Oct. 2018. Accessed on: Jan. 2020. [Online]. Available: https://www.imar-navigation.de/downloads/Decision_assistant-Dateien/Decision_assistant.pdf

[48] M. S. Grewal, V. D. Henderson, and R. S. Miyasako, “Application of Kalman filtering to the calibration and alignment of inertial navigation systems,” *IEEE Transactions on Automatic Control*, vol. 36, no. 1, pp. 3–13, 1991.

[49] M. Glueck, D. Oshinubi, and Y. Manoli, “Automatic real-time offset calibration of gyroscopes,” *Microsystem Technologies*, vol. 21, no. 2, pp. 429–443, 2015.

[50] N. El-Sheimy, H. Hou, and X. Niu, “Analysis and modeling of inertial sensors using Allan variance,” *Instrumentation and Measurement, IEEE Transactions on*, vol. 57, no. 1, pp. 140–149, 2008.

[51] S. Nasiri, “A critical review of MEMS gyroscopes technology and commercialization status,” 2010. Accessed on: Jan. 2020. [Online]. Available: https://pdfs.semanticscholar.org/1a8a/86811627629ae3c2da5d04a41cf94c5e6b1e.pdf

[52] E. Edwan, “Novel approaches for improved performance of inertial sensors and integrated navigation systems,” Ph.D. dissertation, Universität Siegen, 2013.

[53] Z. Chen, Q. Zhu, and Y. C. Soh, “Smartphone inertial sensor-based indoor localization and tracking with iBeacon corrections,” *IEEE Transactions on Industrial Informatics*, vol. 12, no. 4, pp. 1540–1549, 2016.

[54] Robert Bosch GmbH, “Ten billion superheroes in chip format,” Accessed on: Jan. 2020. [Online]. Available: https://www.bosch-mobility-solutions.com/en/highlights/connected-mobility/mems-jubilee/

[55] R. F. Brena, J. P. García-Vázquez, C. E. Galván-Tejada, D. Muñoz-Rodriguez, C. Vargas-Rosales, and J. Fangmeyer, “Evolution of indoor positioning technologies: A survey,” *Journal of Sensors*, vol. 2017, 2017.

[56] F. Zafari, A. Gkelias, and K. K. Leung, “A survey of indoor localization systems and technologies,” *IEEE Communications Surveys & Tutorials*, 2019.

[57] P. Davidson and R. Piché, “A survey of selected indoor positioning methods for smartphones,” *IEEE Comm. Surveys & Tutorials*, vol. 19, no. 2, pp. 1347–1370, 2017.

[58] M. Billinghurst, A. Clark, G. Lee *et al.*, “A survey of augmented reality,” *Foundations and Trends in Human–Computer Interaction*, vol. 8, no. 2-3, pp. 73–272, 2015.

[59] S. Welsner, “MEMS-Inertialsensoren für High-End Navigationsanwendungen,” Master’s thesis, Hochschule Reutlingen, August 2015.

[60] T. Koldbæk, “Improving MEMS gyroscope performance using homogeneous sensor fusion,” Master’s thesis, Aalborg University, 2011.

[61] IEEE, “IEEE standard specification format guide and test procedure for single-axis interferometric fiber optic gyros,” *IEEE Std 952-1997 (R2008)*, 2008.

[62] D. Gebre-Egziabher, “Design and performance analysis of a low-cost aided dead reckoning navigator,” Ph.D. dissertation, Citeseer, 2004.

[63] M. Wis and I. Colomina, “Dynamic dependent IMU stochastic modeling for enhanced INS/GNSS navigation,” in *Satellite Navigation Technologies and European Workshop on GNSS Signals and Signal Processing (NAVITEC), 2010 5th ESA Workshop on.* IEEE, 2010, pp. 1–5.

[64] D. W. Allan, “Historicity strengths and weaknesses of Allan variances and their general applications,” *Saint-Petersburg: CSRI Elektropribor JSC*, pp. 507–524, 2015.

[65] R. J. Vaccaro and A. S. Zaki, “Statistical modeling of rate gyros,” *Instrumentation and Measurement, IEEE Transactions on*, vol. 61, no. 3, pp. 673–684, 2012.

[66] IEEE, “IEEE standard specification format guide and test procedure for linear, single-axis, non-gyroscopic accelerometers,” *IEEE Std 1293-1998 (R2008)*, pp. 1–249, July 2011.

[67] C. Jiang, L. Xue, H. Chang, G. Yuan, and W. Yuan, “Signal processing of MEMS gyroscope arrays to improve accuracy using a 1st order Markov for rate signal modeling,” *Sensors*, vol. 12, no. 2, pp. 1720–1737, 2012.

[68] D. W. Allan *et al.*, “Time and frequency (time-domain) characterization, estimation, and prediction of precision clocks and oscillators,” *IEEE Transactions on Ultrasonics, Ferroelectrics, and Frequency Control*, vol. 34, no. 6, pp. 647–654, 1987.

[69] H. Hou, “Modeling inertial sensors errors using Allan variance,” Master’s thesis, University of Calgary, Department of Geomatics Engineering, 2004.

[70] M. M. Tehrani, “Ring laser gyro data analysis with cluster sampling technique,” in *Fiber Optic and Laser Sensors I*, vol. 412. International Society for Optics and Photonics, 1983, pp. 207–221.

[71] MathWorks, "pwelch: Welch's power spectral density estimate," Accessed on: Jan. 2020. [Online]. Available: https://de.mathworks.com/help/signal/ref/pwelch.html

[72] H. Schmid, "How to use the FFT and Matlab's pwelch function for signal and noise simulations and measurements," *Institute of Microelectronics, University of Applied Sciences NW Switzerland*, 2012.

[73] B. Djebali, "Characterization, modelling and data fusion of MEMS inertial sensors for high performance applications," Master's thesis, Technical University of Munich, 2017.

[74] A. A. Trusov, "Allan variance analysis of random noise modes in gyroscopes," MicroSystems Laboratory, University of California, Irvine, Tech. Rep., 2011.

[75] D. Kim and R. M'Closkey, "Noise analysis of closed-loop vibratory rate gyros," in *American Control Conference (ACC), 2012.* IEEE, 2012, pp. 92–97.

[76] R. P. Leland, "Mechanical-thermal noise in MEMS gyroscopes," *IEEE Sensors Journal*, vol. 5, no. 3, pp. 493–500, 2005.

[77] C. D. Ezekwe and B. E. Boser, "A mode-matching $\Sigma\Delta$ closed-loop vibratory gyroscope readout interface with a $0.004°/s/\sqrt{}$hz noise floor over a 50 Hz band," *IEEE Journal of solid-state circuits*, vol. 43, no. 12, pp. 3039–3048, 2008.

[78] M. S. Keshner, "1/f noise," *Proceedings of the IEEE*, vol. 70, no. 3, pp. 212–218, 1982.

[79] B. Lenoir, "Predicting the variance of a measurement with 1/f noise," *Fluctuation and Noise Letters*, vol. 12, no. 1, May 2013.

[80] E. Milotti, "1/f noise: A pedagogical review," *arXiv preprint physics/0204033*, 2002.

[81] H. Schmid, "Offset, flicker noise, and ways to deal with them," in *Circuits at the Nanoscale: Communications, Imaging, and Sensing.* CRC Press, 2008, pp. 95–115.

[82] H. Zhivomirov, "Pink, red, blue and violet noise generation with matlab," Matlab File Exchange, Feb. 2018. Accessed on: Jan. 2020. [Online]. Available: https://de.mathworks.com/matlabcentral/fileexchange/42919-pink-red-blue-and-violet-noise-generation-with-matlab

[83] P. Bak, C. Tang, and K. Wiesenfeld, "Self-organized criticality: An explanation of the 1/f noise," *Physical review letters*, vol. 59, no. 4, p. 381, 1987.

[84] D. Titterton and J. L. Weston, *Strapdown inertial navigation technology.* IET, 2004, vol. 17.

[85] A. Noureldin, T. B. Karamat, and J. Georgy, *Fundamentals of inertial navigation, satellite-based positioning and their integration.* Springer Science & Business Media, 2012.

[86] W. Fichter and W. Grimm, *Flugmechanik.* Shaker Verlag GmbH, 2009.

[87] MathWorks, “Model and simulate vehicle dynamics in a virtual 3D environment,” Accessed on: Jan. 2020. [Online]. Available: https://de.mathworks.com/products/vehicle-dynamics.html

[88] ——, “Double-lane change maneuver,” Accessed on: Jan. 2020. [Online]. Available: https://de.mathworks.com/help/vdynblks/ug/double-lane-change-maneuver.html

[89] ——, “Slowly increasing steering maneuver,” Accessed on: Jan. 2020. [Online]. Available: https://de.mathworks.com/help/vdynblks/ug/slowly-increasing-steering-maneuver.html

[90] N. El-Sheimy and X. Niu, “The promise of MEMS to the navigation community,” *Inside GNSS*, vol. 2, no. 2, pp. 46–56, 2007.

[91] L. Blocher, F. Baklanov, T. Hiller, M. Rocznik, J. Gerlach, and O. Bringmann, “An experimental localization sensor platform for enhanced initial heading estimation,” in *IEEE International Symposium on Inertial Sensors and Systems.* IEEE, March 2020.

[92] F. Bu, D. Xu, H. Zhao, B. Fan, and M. Cheng, “MEMS gyroscope automatic real-time mode-matching method based on phase-shifted 45° additional force demodulation,” *Sensors*, vol. 18, no. 9, p. 3001, 2018.

[93] I. P. Prikhodko, J. A. Gregory, W. A. Clark, J. A. Geen, M. W. Judy, C. H. Ahn, and T. W. Kenny, “Mode-matched MEMS coriolis vibratory gyroscopes: Myth or reality?” in *Position, Location and Navigation Symposium (PLANS), 2016 IEEE/ION.* IEEE, 2016, pp. 1–4.

[94] S. Askari, M. Asadian, K. Kakavand, and A. Shkel, “Near-navigation grade quad mass gyroscope with Q-factor limited by thermo-elastic damping,” *Solid-State Sensors, Actuators and Microsystems Workshop Hilton Head Island, South Carolina*, 2016.

[95] IEEE, “IEEE standard specification format guide and test procedure for coriolis vibratory gyros,” *IEEE Std 1431-2004*, pp. 1–78, Dec 2004.

[96] A. A. Trusov, I. P. Prikhodko, S. A. Zotov, A. R. Schofield, and A. M. Shkel, “Ultra-high Q silicon gyroscopes with interchangeable rate and

whole angle modes of operation," in *IEEE SENSORS 2010*. IEEE, 2010, pp. 864–867.

[97] S. A. Zotov, I. P. Prikhodko, A. A. Trusov, and A. M. Shkel, "Frequency modulation based angular rate sensor," in *Micro Electro Mechanical Systems (MEMS), 2011 IEEE 24th International Conference on*. IEEE, 2011, pp. 577–580.

[98] J. Classen, J. Reinmuth, A. Kälberer, A. Scheurle, S. Günther, S. Kiesel, B. Schellin, J. Bräuer, and L. Eicher, "Advanced surface micromachining process - A first step towards 3D MEMS," in *Micro Electro Mechanical Systems (MEMS), 2017 IEEE 30th International Conference on*. IEEE, 2017, pp. 314–318.

[99] A. Izadian, J. Dawson, and P. Famouri, "Input-output synchronization for bias drift reduction of MEMS gyroscopes," in *American Control Conference, 2008*. IEEE, 2008, pp. 3751–3754.

[100] A. R. Schofield, A. A. Trusov, C. Acar, and A. M. Shkel, "Anti-phase driven rate gyroscope with multi-degree of freedom sense mode," in *TRANSDUCERS 2007-2007 International Solid-State Sensors, Actuators and Microsystems Conference*. IEEE, 2007, pp. 1199–1202.

[101] R. E. Stewart and S. F. Wyse, "Bias and quadrature reduction in class II coriolis vibratory gyros," July 2009, US Patent 7,565,839.

[102] G. Casinovi, W. Sung, M. Dalal, A. Shirazi, and F. Ayazi, "Electrostatic self-calibration of vibratory gyroscopes," in *2012 IEEE 25th International Conference on Micro Electro Mechanical Systems (MEMS)*. IEEE, 2012, pp. 559–562.

[103] A. A. Trusov, I. P. Prikhodko, S. A. Zotov, and A. M. Shkel, "High-Q and wide dynamic range inertial MEMS for north-finding and tracking applications," in *Position Location and Navigation Symposium (PLANS), 2012 IEEE/ION*. IEEE, 2012, pp. 247–251.

[104] P. Taheri-Tehrani, A. D. Challoner, O. Izyumin, B. Boser, and D. Horsley, "A new electronic feedback compensation method for rate integrating gyroscopes," in *IEEE International Symposium on Inertial Sensors and Systems 2015*. IEEE, 2016, pp. 9–12.

[105] I. P. Prikhodko, J. A. Gregory, D. I. Bugrov, and M. W. Judy, "Overcoming limitations of rate integrating gyroscopes by virtual rotation," in *IEEE International Symposium on Inertial Sensors and Systems 2016*. IEEE, 2016, pp. 5–8.

[106] A. Trusov, I. Prikhodko, D. Rozelle, A. Meyer, and A. Shkel, "1 ppm precision self-calibration of scale factor in MEMS coriolis vibratory gyroscopes," in *2013 Transducers & Eurosensors XXVII: The 17th International Conference on Solid-State Sensors, Actuators and Microsystems (TRANSDUCERS & EUROSENSORS XXVII).* IEEE, 2013, pp. 2531–2534.

[107] A. Trusov, D. Rozelle, G. Atikyan, S. Zotov, B. Simon, A. Shkel, and A. Meyer, "Non-axisymmetric coriolis vibratory gyroscope with whole angle, force rebalance, and self-calibration," in *Proceedings of the Technical Digest of IEEE Solid State Sensors, Actuators and Microsystems Workshop, Hilton Head Island, SC, USA*, 2014, pp. 8–12.

[108] V. Zega, C. Comi, E. Bordiga, G. Langfelder, L. Falorni, and A. Corigliano, "Towards 3-axis FM MEMS gyroscopes: Mechanical design and experimental validation," in *2019 20th International Conference on Solid-State Sensors, Actuators and Microsystems & Eurosensors XXXIII (TRANSDUCERS & EUROSENSORS XXXIII).* IEEE, 2019, pp. 1933–1936.

[109] H. G. Howard, J. Y. Liu, and B. Buchanan, "Bias self-calibration techniques using silicon disc resonator gyroscope," in *IEEE International Symposium on Inertial Sensors and Systems 2015.* IEEE, 2015, pp. 1–4.

[110] M. Kline, Y.-C. Yeh, B. Eminoglu, I. Izyumin, M. Daneman, D. Horsley, and B. Boser, "MEMS gyroscope bias drift cancellation using continuous-time mode reversal," in *2013 Transducers & Eurosensors XXVII: The 17th International Conference on Solid-State Sensors, Actuators and Microsystems (TRANSDUCERS & EUROSENSORS XXVII).* IEEE, 2013, pp. 1855–1858.

[111] J. A. Gregory, J. Cho, and K. Najafi, "Novel mismatch compensation methods for rate-integrating gyroscopes," in *Position Location and Navigation Symposium (PLANS), 2012 IEEE/ION.* IEEE, 2012, pp. 252–258.

[112] C. C. Painter and A. M. Shkel, "Active structural error suppression in MEMS vibratory rate integrating gyroscopes," *IEEE Sensors Journal*, vol. 3, no. 5, pp. 595–606, 2003.

[113] S. Zotov, I. Prikhodko, B. Simon, A. Trusov, and A. Shkel, "Self-calibrated MEMS gyroscope with AM/FM operational modes, dynamic range of 180 dB and in-run bias stability of 0.1 deg/hr," in *DGON Inertial Sensors and Systems Symposium (ISS) 2014.* IEEE, 2014, pp. 1–17.

[114] A. Norouzpour-Shirazi, D. Serrano, M. Zaman, G. Casinovi, and F. Ayazi, "A dual-mode gyroscope architecture with in-run mode-matching capability and inherent bias cancellation," in *2015 Transducers-2015 18th*

Intl. Conference on Solid-State Sensors, Actuators and Microsystems (TRANSDUCERS). IEEE, 2015, pp. 23–26.

[115] A. Norouz Pour Shirazi, "Advanced interface systems for readout, control, and self-calibration of MEMS resonant gyroscopes," Ph.D. dissertation, Georgia Institute of Technology, 2016.

[116] M. Marx, D. De Dorigo, S. Nessler, S. Rombach, and Y. Manoli, "A 27 μW 0.06 mm^2 background resonance frequency tuning circuit based on noise observation for a 1.71 mW CT-$\Delta\Sigma$ MEMS gyroscope readout system with 0.9°/h bias instability," *IEEE Journal of Solid-State Circuits*, 2018.

[117] Y. Zhao, J. Zhao, X. Wang, G. M. Xia, Q. Shi, A. P. Qiu, and Y. P. Xu, "A sub-0.1°/h bias-instability split-mode MEMS gyroscope with CMOS readout circuit," *IEEE Journal of Solid-State Circuits*, vol. 53, no. 9, pp. 2636–2650, 2018.

[118] S. Koenig, S. Rombach, W. Gutmann, A. Jaeckle, C. Weber, M. Ruf, D. Grolle, and J. Rende, "Towards a navigation grade Si-MEMS gyroscope," in *DGON Inertial Sensors and Systems Symposium (ISS) 2019*, Sep. 2019, pp. 1–18.

[119] J. Raman, E. Cretu, P. Rombouts, and L. Weyten, "A closed-loop digitally controlled MEMS gyroscope with unconstrained sigma-delta force-feedback," *Sensors Journal, IEEE*, vol. 9, no. 3, pp. 297–305, 2009.

[120] M. Saukoski, L. Aaltonen, T. Salo, and K. Halonen, "Readout and control electronics for a microelectromechanical gyroscope," in *2006 IEEE Instrumentation and Measurement Technology Conference Proceedings*. IEEE, 2006, pp. 1741–1746.

[121] M. Saukoski *et al.*, "System and circuit design for a capacitive MEMS gyroscope," Ph.D. dissertation, Helsinki University of Technology, 2008.

[122] A. Sharma, M. F. Zaman, M. Zucher, and F. Ayazi, "A 0.1°/hr bias drift electronically matched tuning fork microgyroscope," in *Micro Electro Mechanical Systems, 2008. MEMS 2008. IEEE 21st International Conference on.* IEEE, 2008, pp. 6–9.

[123] E. Tatar, S. E. Alper, and T. Akin, "Quadrature-error compensation and corresponding effects on the performance of fully decoupled MEMS gyroscopes," *Journal of Microelectromechanical Systems*, vol. 21, no. 3, pp. 656–667, 2012.

[124] E. Tatar, S. Alper, and T. Akin, "Effect of quadrature error on the performance of a fully-decoupled MEMS gyroscope," in *Micro Electro Mechanical Systems (MEMS), 2011 IEEE 24th International Conference on.* IEEE, 2011, pp. 569–572.

[125] A. Trusov, G. Atikyan, D. Rozelle, A. Meyer, S. Zotov, B. Simon, and A. Shkel, “Force rebalance, whole angle, and self-calibration mechanization of silicon MEMS quad mass gyro,” in *IEEE International Symposium on Inertial Sensors and Systems 2014*. IEEE, 2014, pp. 1–2.

[126] A. A. Trusov, G. Atikyan, D. Rozelle, A. Meyer, S. Zotov, B. Simon, and A. Shkel, “Flat is not dead: Current and future performance of Si-MEMS quad mass gyro (QMG) system,” in *2014 IEEE/ION Position, Location and Navigation Symposium-PLANS 2014*. IEEE, 2014, pp. 252–258.

[127] M. Descharles, J. Guérard, H. Kokabi, and O. Le Traon, “Closed-loop compensation of the cross-coupling error in a quartz coriolis vibrating gyro,” *Sensors and Actuators A: Physical*, vol. 181, pp. 25–32, 2012.

[128] S. A. Zotov, B. R. Simon, G. Sharma, A. A. Trusov, and A. M. Shkel, “Utilization of mechanical quadrature in silicon MEMS vibratory gyroscope to increase and expand the long term in-run bias stability,” in *IEEE International Symposium on Inertial Sensors and Systems 2014*. IEEE, 2014, pp. 1–4.

[129] S. A. Zotov, B. R. Simon, I. P. Prikhodko, and A. A. Trusov, “Utilization of mechanical quadrature in silicon MEMS vibratory gyroscope to increase and expand the long term in-run bias stability,” October 2015, US Patent 20,150,285,658.

[130] B. Eminoglu, M. H. Kline, I. Izyumin, Y.-C. Yeh, and B. E. Boser, “Background calibrated MEMS gyroscope,” in *IEEE SENSORS 2014 Proceedings*. IEEE, 2014, pp. 922–925.

[131] I. Prikhodko, A. Trusov, and A. Shkel, “Achieving long-term bias stability in high-Q inertial MEMS by temperature self-sensing with a 0.5 millicelcius precision,” in *Proc. of Solid-State Sensors, Actuators, and Microsystems Workshop, Hilton Head Island, South Carolina*, vol. 1, 2012, p. 1.

[132] I. P. Prikhodko, A. A. Trusov, and A. M. Shkel, “Compensation of drifts in high-Q MEMS gyroscopes using temperature self-sensing,” *Sensors and Actuators A: Physical*, vol. 201, pp. 517–524, 2013.

[133] E. Tatar, T. Mukherjee, and G. K. Fedder, “Stress effects and compensation of bias drift in a MEMS vibratory-rate gyroscope,” *Journal of Microelectromechanical Systems*, vol. 26, no. 3, pp. 569–579, 2017.

[134] ——, “On-chip stress compensation on the ZRO of a mode-matched MEMS gyroscope,” in *IEEE International Symposium on Inertial Sensors and Systems 2016*. IEEE, 2016, pp. 128–131.

[135] I. P. Prikhodko, J. A. Gregory, C. Merritt, J. A. Geen, J. Chang, J. Bergeron, W. Clark, and M. W. Judy, “In-run bias self-calibration for low-cost MEMS vibratory gyroscopes,” in *2014 IEEE/ION Position, Location and Navigation Symposium-PLANS 2014*. IEEE, 2014, pp. 515–518.

[136] J. A. Geen and J. F. Chang, “MEMS gyroscopes with reduced errors,” December 2015, US Patent 9,212,908.

[137] W. A. Clark and J. A. Geen, “Offset detection and compensation for micromachined inertial sensors,” July 2014, US Patent 8,783,103.

[138] D. M. Rozelle, “Self calibrating gyroscope system,” March 2011, US Patent 7,912,664.

[139] I. P. Prikhodko, C. Merritt, J. A. Gregory, J. A. Geen, J. Chang, J. Bergeron, W. Clark, and M. W. Judy, “Continuous self-calibration canceling drive-induced errors in MEMS vibratory gyroscopes,” in *2015 Transducers-2015 18th International Conference on Solid-State Sensors, Actuators and Microsystems (TRANSDUCERS)*. IEEE, 2015, pp. 35–38.

[140] B. Eminoglu, M. H. Kline, I. Izyumin, Y.-C. Yeh, and B. E. Boser, “Ratiometric readout technique for MEMS gyroscopes with force feedback,” in *2014 IEEE/ION Position, Location and Navigation Symposium-PLANS 2014*. IEEE, 2014, pp. 1203–1208.

[141] F. Yesil, S. Alper, and T. Akin, “An automatic mode matching system for a high Q-factor MEMS gyroscope using a decoupled perturbation signal,” in *18th International Conference on Solid-State Sensors, Actuators and Microsystems (TRANSDUCERS)*. IEEE, 2015, pp. 1148–1151.

[142] D. Kim and R. T. M’closkey, “Dissecting tuned MEMS vibratory gyros,” *Feedback Control of MEMS to Atoms*, p. 211, 2011.

[143] I. P. Prikhodko, S. Nadig, J. A. Gregory, W. A. Clark, and M. W. Judy, “Half-a-month stable 0.2 degree-per-hour mode-matched MEMS gyroscope,” in *IEEE International Symposium on Inertial Sensors and Systems 2017*. IEEE, 2017.

[144] S. Sonmezoglu, P. Taheri-Tehrani, C. Valzasina, L. G. Falorni, S. Zerbini, S. Nitzan, and D. A. Horsley, “Single-structure micromachined three-axis gyroscope with reduced drive-force coupling,” *IEEE Electron Device Letters*, vol. 36, no. 9, pp. 953–956, 2015.

[145] D. Endean, K. Christ, P. Duffy, E. Freeman, M. Glenn, M. Gnerlich, B. Johnson, and J. Weinmann, “Near-navigation grade tuning fork MEMS gyroscope,” in *IEEE International Symposium on Inertial Sensors and Systems 2019*. IEEE, 2019, pp. 171–174.

[146] B. Johnson, K. Christ, D. Endean, B. Mohr, R. Supino, H. French, and E. Cabuz, “Tuning fork MEMS gyroscope for precision northfinding,” in *DGON Inertial Sensors and Systems Symposium (ISS) 2015*. IEEE, 2015, pp. 1–10.

[147] I. P. Prikhodko, S. A. Zotov, A. A. Trusov, and A. M. Shkel, “What is MEMS gyrocompassing? Comparative analysis of maytagging and carouseling,” *Journal of Microelectromechanical Systems*, vol. 22, no. 6, pp. 1257–1266, 2013.

[148] Y. Zhao, J. Zhao, G. M. Xia, A. P. Qiu, Y. Su, X. Wang, and Y. P. Xu, “A 0.57 deg/h bias instability 0.067deg/rthz angle random walk MEMS gyroscope with CMOS readout circuit,” in *IEEE Asian Solid-State Circuits Conference (A-SSCC)*. IEEE, 2015, pp. 1–4.

[149] O. Deppe, G. Dorner, S. Koenig, T. Martin, S. Voigt, and S. Zimmermann, “MEMS and FOG technologies for tactical and navigation grade inertial sensors—recent improvements and comparison,” *Sensors*, vol. 17, no. 3, p. 567, 2017.

[150] M. Saukoski, L. Aaltonen, and K. A. Halonen, “Zero-rate output and quadrature compensation in vibratory MEMS gyroscopes,” *IEEE Sensors Journal*, vol. 7, no. 12, pp. 1639–1652, 2007.

[151] C. D. Ezekwe, *Readout techniques for high-Q micromachined vibratory rate gyroscopes*. ProQuest, 2007.

[152] H. Wen, *Toward Inertial-Navigation-on-Chip: The Physics and Performance Scaling of Multi-Degree-of-Freedom Resonant MEMS Gyroscopes*. Springer Nature, 2019.

[153] J. Bernstein *et al.*, “An overview of MEMS inertial sensing technology,” *Sensors - The Journal of Applied Sensing Technology*, vol. 20, no. 2, pp. 14–21, Feb. 2003.

[154] N. Yazdi, F. Ayazi, and K. Najafi, “Micromachined inertial sensors,” *Proceedings of the IEEE*, vol. 86, no. 8, pp. 1640–1659, 1998.

[155] M. Lobur and A. Holovatyy, “Overview and analysis of readout circuits for capacitive sensing in MEMS gyroscopes (MEMS angular velocity sensors),” in *2009 5th International Conference on Perspective Technologies and Methods in MEMS Design*. IEEE, 2009, pp. 161–163.

[156] R. Legtenberg, A. Groeneveld, and M. Elwenspoek, “Comb-drive actuators for large displacements,” *Journal of Micromechanics and microengineering*, vol. 6, no. 3, p. 320, 1996.

[157] A. Walther, C. Le Blanc, N. Delorme, Y. Deimerly, R. Anciant, and J. Willemin, “Bias contributions in a MEMS tuning fork gyroscope,” *Journal of Microelectromechanical Systems*, vol. 22, no. 2, pp. 303–308, 2013.

[158] Q. Shen, H. Li, Y. Hao, W. Yuan, and H. Chang, “Bias contribution modeling for a symmetrical micromachined coriolis vibratory gyroscope,” *IEEE Sensors Journal*, vol. 16, no. 3, pp. 723–733, Feb 2016.

[159] M. S. Weinberg and A. Kourepenis, “Error sources in in-plane silicon tuning-fork MEMS gyroscopes,” *Journal of Microelectromechanical Systems*, vol. 15, no. 3, pp. 479–491, 2006.

[160] L. Meyer, A. Buhmann, R. Eid, and J. G. Korvink, “Root cause analysis of zero-rate output sources in an MEMS gyroscope,” *IEEE Sensors Journal*, vol. 17, no. 4, pp. 959–966, Feb 2017.

[161] U. Nabholz, M. Curcic, J. E. Mehner, and P. Degenfeld-Schonburg, “Nonlinear dynamical system model for drive mode amplitude instabilities in MEMS gyroscopes,” in *IEEE International Symposium on Inertial Sensors and Systems 2019.* IEEE, 2019, pp. 9–12.

[162] M. Putnik, S. Cardanobile, M. Sniegucki, S. Kehrberg, M. Kuehnel, P. Degenfeld-Schonburg, C. Nagel, and J. Mehner, “Simulation methods for generating reduced order models of MEMS sensors with geometric nonlinear drive motion,” in *IEEE International Symposium on Inertial Sensors and Systems 2018.* IEEE, 2018, pp. 1–4.

[163] A. G. Quinchia, G. Falco, E. Falletti, F. Dovis, and C. Ferrer, “A comparison between different error modeling of MEMS applied to GPS/INS integrated systems,” *Sensors*, vol. 13, no. 8, pp. 9549–9588, 2013.

[164] A. Thomae, J. Artzner, R. Neul, G. Bischopink, K. Funk, and M. Lutz, “Method and device for tuning a first oscillator with a second oscillator and rotation rate sensor,” November 2003, US Patent 6,654,424.

[165] W. C. Pflanzl and E. Seebacher, “1/f noise temperature behaviour of poly resistors,” in *Proceedings of the 19th International Conference Mixed Design of Integrated Circuits and Systems-MIXDES 2012.* IEEE, 2012, pp. 297–299.

[166] N. K. Rajan, D. A. Routenberg, J. Chen, and M. A. Reed, “Temperature dependence of 1/f noise mechanisms in silicon nanowire biochemical field effect transistors,” *Applied Physics Letters*, vol. 97, no. 24, p. 243501, 2010.

[167] Y. Zhao, G.-M. Xia, Q. Shi, and A.-P. Qiu, “A low flicker noise automatic amplitude control ASIC for a split-mode MEMS gyroscope,” in *2018 14th IEEE International Conference on Solid-State and Integrated Circuit Technology (ICSICT)*. IEEE, 2018, pp. 1–3.

[168] R. Gonzalez and P. Dabove, “Performance assessment of an ultra low-cost inertial measurement unit for ground vehicle navigation,” *Sensors*, vol. 19, no. 18, p. 3865, 2019.

[169] J. Jia, X. Ding, Y. Gao, and H. Li, “Automatic frequency tuning technology for dual-mass MEMS gyroscope based on a quadrature modulation signal,” *MDPI Micromachines*, vol. 9, no. 10, p. 511, 2018.

[170] M. Maurer, S. Rombach, and Y. Manoli, “Resonance frequency control and digital correction for capacitive MEMS gyroscopes within electromechanical bandpass delta-sigma-modulatorss,” in *IEEE International Symposium on Inertial Sensors and Systems 2018*. IEEE, 2018, pp. 1–4.

[171] D.-I. M. Maurer, “System dimensioning, digital postprocessing, and nonideality control for electromechanical delta-sigma-modulator based angular rate detection,” Ph.D. dissertation, Albert-Ludwigs-University Freiburg, 2018.

[172] A. R. Duggal, S. Sonkusale, and J. Lachapelle, “Calibration of delta-sigma data converters in synchronous demodulation sensing applications,” *IEEE Sensors Journal*, vol. 11, no. 1, pp. 16–22, 2011.

[173] E. H. Sarraf, A. Kansal, M. Sharma, and E. Cretu, “FPGA-based novel adaptive scheme using PN sequences for self-calibration and self-testing of MEMS-based inertial sensors,” *Journal of Electronic Testing*, vol. 28, no. 5, pp. 599–614, 2012.

[174] A. Kansal, E. H. Sarraf, M. Sharma, and E. Cretu, “Novel adaptive FPGA-based self-calibration and self-testing scheme with PN sequences for MEMS-based inertial sensors,” in *17th International Mixed-Signals, Sensors and Systems Test Workshop (IMS3TW)*. IEEE, 2011, pp. 120–126.

[175] D. M. Rozelle, “Closed loop scale factor estimation,” December 2009, US Patent 7,628,069.

[176] E. E. Aktakka and K. Najafi, “A six-axis micro platform for in situ calibration of MEMS inertial sensors,” in *IEEE 29th International Conference on Micro Electro Mechanical Systems (MEMS) 2016*. IEEE, 2016, pp. 243–246.

[177] S. Nadig, V. Pinrod, S. Ardanuç, and A. Lal, "In-run scale factor and drift calibration of MEMS gyroscopes with rejection of acceleration sensitivities," in *IEEE International Symposium on Inertial Sensors and Systems 2016*. IEEE, 2016, pp. 144–145.

[178] S. Park and R. Horowitz, "Adaptive control for the conventional mode of operation of MEMS gyroscopes," *Journal of Microelectromechanical Systems*, vol. 12, no. 1, pp. 101–108, 2003.

[179] ——, "New adaptive mode of operation for MEMS gyroscopes," *Journal of Dynamic Systems, Measurement, and Control*, vol. 126, no. 4, pp. 800–810, 2004.

[180] M. Afifi, M. Maurer, T. Hehn, A. Taschwer, and Y. Manoli, "An automatic tuning technique for background frequency calibration in gyroscope interfaces based on high order bandpass delta-sigma modulators," in *Circuits and Systems (ISCAS), 2015 IEEE International Symposium on*. IEEE, 2015, pp. 1730–1733.

[181] M. Marx, X. Cuignet, S. Nessler, D. De Dorigo, and Y. Manoli, "An automatic MEMS gyroscope mode matching circuit based on noise observation," *IEEE Transactions on Circuits and Systems II: Express Briefs*, vol. 66, no. 5, pp. 743–747, 2019.

[182] L. Ljung, "System identification," in *Signal analysis and prediction*. Springer, 1998, pp. 163–173.

[183] U. Forssell, "Closed-loop identification: Methods, theory, and applications," Ph.D. dissertation, Linköping University Electronic Press, 1999.

[184] U. Forssell and L. Ljung, "Closed-loop identification revisited," *Automatica*, vol. 35, no. 7, pp. 1215–1241, 1999.

[185] B. Heimann, A. Albert, T. Ortmaier, and L. Rissing, *Mechatronik: Komponenten-Methoden-Beispiele*. Carl Hanser Verlag GmbH Co KG, 2015.

[186] R. Schreier, G. C. Temes *et al.*, *Understanding delta-sigma data converters*. IEEE press Piscataway, NJ, 2005, vol. 74.

[187] MathWorks, "modalfrf: Frequency-response functions for modal analysis," Accessed on: Jan. 2020. [Online]. Available: https://de.mathworks.com/help/signal/ref/modalfrf.html

[188] ——, "oe: Estimate output-error polynomial model using time or frequency domain data," Accessed on: Jan. 2020. [Online]. Available: https://de.mathworks.com/help/ident/ref/oe.html

[189] N. El-Sheimy, K.-W. Chiang, and A. Noureldin, “The utilization of artificial neural networks for multisensor system integration in navigation and positioning instruments,” *IEEE Transactions on Instrumentation and Measurement*, vol. 55, no. 5, pp. 1606–1615, 2006.

[190] Z. Pentek, T. Hiller, and A. Czmerk, “Algorithmic enhancement of automotive MEMS inertial sensors with consumer-type redundancy,” *IEEE Sensors Journal*, submitted 2020.

[191] F. Vernotte and E. Lantz, “Metrology and 1/f noise: Linear regressions and confidence intervals in flicker noise context,” *Metrologia*, vol. 52, no. 2, p. 222, 2015.

[192] Y. M. Ding, D. D. Misra, and P. Srinivasan, “Flicker noise performance on thick and thin oxide FinFETs,” *IEEE Transactions on Electron Devices*, vol. 64, no. 5, pp. 2321–2325, 2017.

[193] D. W. Ricker, *Echo signal processing.* Springer Science & Business Media, 2012, vol. 725.

[194] M. A. Sturza, “Navigation system integrity monitoring using redundant measurements,” *Navigation*, vol. 35, no. 4, pp. 483–501, 1988.

[195] A. Waegli, S. Guerrier, and J. Skaloud, “Redundant MEMS-IMU integrated with GPS for performance assessment in sports,” in *Position, Location and Navigation Symposium, 2008 IEEE/ION.* IEEE, 2008, pp. 1260–1268.

[196] M. E. Pittelkau, “Cascaded and decoupled RIMU calibration filters,” *Journal of the Astronautical Sciences*, vol. 54, no. 3-4, pp. 449–466, 2006.

[197] I. Colomina, M. Giménez, J. Rosales, M. Wis, A. Gomez, and P. Miguelsanz, “Redundant IMUs for precise trajectory determination,” in *Proceedings of the 20th ISPRS Congress, Istanbul, Turkey*, vol. 1223. Citeseer, 2004, p. 17.

[198] D. Bayard and S. Ploen, “Foundations of virtual gyroscope synthesis,” *NASA-JPL Internal Document JPL D-21656*, 2002.

[199] L. Xue, C.-Y. Jiang, H.-L. Chang, Y. Yang, W. Qin, and W.-Z. Yuan, “A novel Kalman filter for combining outputs of MEMS gyroscope array,” *Measurement*, vol. 45, no. 4, pp. 745–754, 2012.

[200] X. Ji, “Research on signal processing of MEMS gyro array,” *Mathematical Problems in Engineering*, vol. 2015, 2015.

[201] Q. Shen, W. Yuan, B. Qu, J. Xie, and H. Chang, "A virtual gyroscope based-on a single-chip four-microgyroscope array," in *Nano/Micro Engineered and Molecular Systems (NEMS), 2014 9th IEEE International Conference on.* IEEE, 2014, pp. 195–198.

[202] S. David and R. Scott, "Combining multiple gyroscope outputs for increased accuracy," NASA JPL New Technology Report NPO-30533, Tech. Rep., 2003.

[203] J. Wang and E. Olson, "High-performance inertial measurements using a redundant array of inexpensive gyroscopes (RAIG)," in *Multisensor Fusion and Integration for Intelligent Systems (MFI), 2015 IEEE International Conference on.* IEEE, 2015, pp. 71–76.

[204] Y. Yuksel and N. El-Sheimy, "An optimal sensor fusion method for skew-redundant inertial measurement units," *Journal of applied Geodesy*, vol. 5, no. 2, pp. 99–115, 2011.

[205] T. Haering, "Redundant MEMS inertial sensors for high-performance navigation application," Bachelor's thesis, Eberhard-Karls-University of Tuebingen, 2017.

[206] H. Martin, P. Groves, M. Newman, and R. Faragher, "A new approach to better low-cost MEMS IMU performance using sensor arrays," *The Institute of Navigation*, 2013.

[207] J. Nilsson and I. Skog, "Inertial sensor arrays - A literature review," in *2016 European Navigation Conference (ENC)*, May 2016, pp. 1–10.

[208] J. B. Bancroft and G. Lachapelle, "Data fusion algorithms for multiple inertial measurement units," *Sensors*, vol. 11, no. 7, pp. 6771–6798, 2011.

[209] R. Fontanella, G. de Alteriis, R. Schiano Lo Moriello, D. Accardo, and L. Angrisani, "Results of field testing for an integrated GPS/INS unit based on low-cost redundant MEMS sensors," in *AIAA Scitech 2019 Forum*, 2019, p. 2378.

[210] G. Huang, "Visual-inertial navigation: A concise review," *arXiv preprint arXiv:1906.02650*, 2019.

[211] Z. Yuan, D. Zhu, C. Chi, J. Tang, C. Liao, and X. Yang, "Visual-inertial state estimation with pre-integration correction for robust mobile augmented reality," in *Proceedings of the 27th ACM International Conference on Multimedia*, 2019, pp. 1410–1418.

[212] F. Dauer, D. Görges, and A. Wienss, "Experimental analysis of sensor requirements for eBike rider assistance systems," in *2018 IEEE International Conference on Vehicular Electronics and Safety (ICVES).* IEEE, 2018, pp. 1–6.

[213] J. Schnee, J. Stegmaier, T. Lipowsky, and P. Li, “Brake detection for electric bicycles using inertial measurement units,” in *2019 IEEE Sensors Applications Symposium (SAS)*. IEEE, 2019, pp. 1–6.

[214] Z. Pentek, T. Hiller, T. Liewald, B. Kuhlmann, and A. Czmerk, “IMU-based mounting parameter estimation on construction vehicles,” in *DGON Inertial Sensors and Systems Symposium (ISS) 2017*. IEEE, 2017, pp. 1–14.

[215] S. Abdelgawad, “Low-cost outdoor robot navigation in unstructured environments,” Master’s thesis, Dortmund University, 2016, Deepfield Robotics Bosch.

[216] S. T. Howe, R. J. Aughey, W. G. Hopkins, A. M. Stewart, and B. P. Cavanagh, “Quantifying important differences in athlete movement during collision-based team sports: Accelerometers outperform global positioning systems,” in *IEEE International Symposium on Inertial Sensors and Systems 2017*. IEEE, March 2017, pp. 1–4.

List of Figures

List of Tables

A. Appendix

A.1. Integration of White Noise

Assume a mean-free, discrete, random white noise process $w[k]$ with amount of samples N, constant sample time τ_0 and standard deviation σ_w. Three subsequent integrations with integration time $t = \tau_0 N$ are defined as

$$w_1[N] = \tau_0 \sum_{k=1}^{N} w[k], \tag{A.1}$$

$$w_2[N] = \tau_0 \sum_{k=1}^{N} w_1[k], \tag{A.2}$$

$$w_3[N] = \tau_0 \sum_{k=1}^{N} w_2[k]. \tag{A.3}$$

The variance of w_1 is then derived (compare [59] [60]) as

$$
\begin{aligned}
\mathrm{Var}(w_1[N]) &= \mathrm{Var}(\tau_0 \sum_{k=1}^{N} w[k]) && \text{(A.4)}\\
&= \tau_0^2 \mathrm{Var}(\sum_{k=1}^{N} w[k]) && \text{(A.5)}\\
&= \tau_0^2 \Big(\sum_{k=1}^{N} \mathrm{Var}(w[k]) + 2 \sum_{1 \le i < j \le N} \cancelto{=0}{\mathrm{Cov}(w[i], w[j])} \Big) && \text{(A.6)}\\
&= \tau_0^2 \sum_{k=1}^{N} \mathrm{Var}(w[k]) && \text{(A.7)}\\
&= \tau_0^2 \sum_{k=1}^{N} \sigma_w^2 && \text{(A.8)}\\
&= \tau_0^2 N \sigma_w^2 && \text{(A.9)}
\end{aligned}
$$

and using $\sigma_w = \sigma_{\mathrm{ARW}}(\tau_0) = Q/\sqrt{\tau_0}$

$$
\begin{aligned}
&= Q^2 \tau_0 N && \text{(A.10)}\\
&= Q^2 t. && \text{(A.11)}
\end{aligned}
$$

Next, variance of w_2 is determined (compare [59] [60]) as

$$\begin{aligned}
\mathrm{Var}(w_2[N]) &= \tau_0^2 \mathrm{Var}(\sum_{k=1}^{N} w_1[k]) && \text{(A.12)}\\
&= \tau_0^2 \sum_{k_1,k_2}^{N} \mathrm{Cov}(w_1[k_1], w_1[k_2]) && \text{(A.13)}\\
&= \tau_0^2 \sum_{k_1,k_2}^{N} \mathrm{Cov}(\tau_0 \sum_{i=1}^{k_1} w[i], \tau_0 \sum_{j=1}^{k_2} w[j]) && \text{(A.14)}\\
&= \tau_0^4 \sum_{k_1,k_2}^{N} \sum_{i=1}^{k_1} \sum_{j=1}^{k_2} \mathrm{Cov}(w[i], w[j]) && \text{(A.15)}\\
&= \tau_0^4 \sum_{k_1,k_2}^{N} \sum_{l=1}^{\min(k_1,k_2)} \sigma_w^2 && \text{(A.16)}\\
&= \tau_0^4 \sigma_w^2 \sum_{k_1=1}^{N} \sum_{k_2=1}^{N} \min(k_1, k_2) && \text{(A.17)}\\
&= \tau_0^4 \sigma_w^2 \Big(\frac{N^3}{3} + \frac{N^2}{2} + \frac{N}{6} \Big), && \text{(A.18)}
\end{aligned}$$

using $\sigma_w = \sigma_{\mathrm{ARW}}(\tau_0) = Q/\sqrt{\tau_0}$, gives

$$\begin{aligned}
&= \tau_0^3 Q^2 \Big(\frac{N^3}{3} + \frac{N^2}{2} + \frac{N}{6} \Big) && \text{(A.19)}\\
&= Q^2 \Big(\frac{t^3}{3} + \frac{t^2 \tau_0}{2} + \frac{t \tau_0^2}{6} \Big), && \text{(A.20)}
\end{aligned}$$

which is approximately

$$\approx Q^2 \frac{t^3}{3}. \qquad \text{(A.21)}$$

Lastly, variance of w_3 is (compare [59] [60])

$$\begin{aligned}
\mathrm{Var}(w_3[N]) &= \tau_0^2 \mathrm{Var}(\sum_{k=1}^{N} w_2[k]) && \text{(A.22)}\\
&= \tau_0^2 \sum_{k_1,k_2}^{N} \mathrm{Cov}(w_2[k_1], w_2[k_2]) && \text{(A.23)}\\
&= \tau_0^2 \sum_{k_1,k_2}^{N} \mathrm{Cov}(\tau_0 \sum_{i=1}^{k_1} w_1[i], \tau_0 \sum_{j=1}^{k_2} w_1[j]) && \text{(A.24)}\\
&= \tau_0^4 \sum_{k_1,k_2}^{N} \sum_{i=1}^{k_1} \sum_{j=1}^{k_2} \mathrm{Cov}(w_1[i], w_1[j]) && \text{(A.25)}\\
&= \tau_0^6 \sum_{k_1,k_2}^{N} \sum_{i=1}^{k_1} \sum_{j=1}^{k_2} \sum_{h=1}^{i} \sum_{l=1}^{j} \mathrm{Cov}(w[i], w[j]) && \text{(A.26)}\\
&= \tau_0^6 \sum_{k_1,k_2}^{N} \sum_{i=1}^{k_1} \sum_{j=1}^{k_2} \sum_{g=1}^{\min(i,j)} \sigma_w^2 && \text{(A.27)}\\
&= \tau_0^6 \sigma_w^2 \sum_{k_1=1}^{N} \sum_{k_2=1}^{N} \sum_{i=1}^{k_1} \sum_{j=1}^{k_2} \min(i,j) && \text{(A.28)}\\
&= \tau_0^6 \sigma_w^2 \Big(\frac{N^5}{20} + \frac{N^4}{4} + \frac{5N^3}{12} + \frac{N^2}{4} + \frac{N}{30} \Big), && \text{(A.29)}
\end{aligned}$$

using $\sigma_w = \sigma_{\mathrm{ARW}}(\tau_0) = Q/\sqrt{\tau_0}$, gives

$$\begin{aligned}
&= \tau_0^5 Q^2 \Big(\frac{N^5}{20} + \frac{N^4}{4} + \frac{5N^3}{12} + \frac{N^2}{4} + \frac{N}{30} \Big) && \text{(A.30)}\\
&= Q^2 \Big(\frac{t^5}{20} + \frac{\tau_0 t^4}{4} + \frac{5\tau_0^2 t^3}{12} + \frac{\tau_0^3 t^2}{4} + \frac{\tau_0^4 t}{30} \Big), && \text{(A.31)}
\end{aligned}$$

which is approximately

$$\approx Q^2 \frac{t^5}{20}. \tag{A.32}$$

A.2. Origins and Behavior of 1/f Noise

Numerous, diverse natural processes show approximately 1/f-shaped spectral behavior at low frequencies [78] [80] [83] [191]. One author even purports that "[...] it seems that flicker noise is the rule rather than the exception." [81, p. 2]. In many cases, 1/f noise is found to continue "indefinitely" to lower and lower frequencies when the processes are measured for even longer durations [80] [81]. Being a curiosity in most other fields, 1/f noise is a critical challenge in electronics, particularly in MOSFET transistors [81]. Yet, its sources and the uniform 1/f nature are still not understood in its entirety [81] [192]. Bremsstrahlung and carrier scattering have been named as 1/f noise sources in electronic devices with a third effect of electron trapping being dominant in MOSFETs [81].

It is shown in [78], that 1/f noise can be produced to an accuracy of 5 percent, when filtering white noise through a series of zero-pole pairs, where only a single pair is placed per frequency decade. More generally, [81] states that processes with memories with time constants that are distributed evenly in logarithmic time will create 1/f noise. This notion falls in line with the electron trapping explanation, where single electrons are captured and released on time scales that depend logarithmically on the physical distance of the trap to the active region of a transistor [81]. When very few traps exist, the same effect may appear as random telegraph noise switching between two or more discrete levels [81]. In our experience, random telegraph noise oftentimes still has 1/f characteristic when measured for long durations. Large scale excitation is said to help reset those memories and reduce the generated 1/f noise level [81].

The variance of a 1/f signal grows logarithmically with recording time [81]. If one wants to create 1/f noise of a certain magnitude in simulation, the simulation and sample time needs thus to be taken into consideration. For a mean-free signal, its variance may be interpreted as its power, analogously to e.g. a voltage acting on a $1\,\Omega$ resistor. At the same time, the integral over frequency of the power spectral density also provides the power of the signal [193]. Therefore,

$$\sigma^2 = \frac{1}{2\pi} \int_{\omega_1}^{\omega_2} S_{\mathrm{PSD}}(\omega)\, d\omega, \tag{A.33}$$

where σ^2 is the variance of a band-limited, ω_1 to ω_2, signal with single-sided power spectral density S_{PSD}. In terms of ordinary frequency, f_1 and f_2, 1/f noise is described by its noise level at 1 Hz, N_{1Hz}. See also [79].

$$\sigma^2_{1/\mathrm{f}} = \int_{f_1}^{f_2} N_{\mathrm{1Hz}} \frac{1}{f}\, df \tag{A.34}$$

$$= N_{\mathrm{1Hz}} \ln \frac{f_2}{f_1} \tag{A.35}$$

If it is assumed, that flicker noise keeps its 1/f behavior even for infinitely long processes, the variance becomes infinite, even though the frequency band is limited from $f_1 = 0\,\mathrm{Hz}$ to e.g. half the sampling frequency $f_2 = \frac{1}{2\tau_0}$ [81].

For a finite signal, it is sometimes suggested that one may instead integrate from $f_1 = \frac{1}{T_{\mathrm{end}}}$ onwards, where T_{end} is the measurement duration [79] [191]. That approximation applies when the mean over the total measurement duration is subtracted, which is of course not applicable in most real-world experiments and applications. Deciding is lastly the actual, physical 1/f process and the lowest extend of its 1/f behavior, $f_1 = \frac{1}{T_1}$. Here we assume a signal generated in simulation with its mean removed.

$$\sigma^2_{1/\mathrm{f}} \approx N_{1\mathrm{Hz}} \ln \frac{T_{\mathrm{end}}}{2\,\tau_0} \tag{A.36}$$

With equation (A.78) from below, the variance of a signal of certain sample time and measurement time can be related to its bias instability level,

$$\sigma^2_{1/\mathrm{f}} \approx \frac{\sigma^2_{\mathrm{BIS}}}{2\ln 2} \ln \frac{T_{\mathrm{end}}}{2\,\tau_0}. \tag{A.37}$$

To give an example, a 1/f angular rate signal was created in simulation using

$$\tau_0 = 0.01\,\mathrm{s} \tag{A.38}$$

$$T_{\mathrm{end}} = 10\,\mathrm{h} \tag{A.39}$$

$$\sigma_{\mathrm{BIS}} = 5\,\mathrm{dph}. \tag{A.40}$$

The necessary variance to produce such a signal can then be calculated as

$$\sigma_{1/\mathrm{f}} = 0.0045\,\mathrm{dps}. \tag{A.41}$$

The resulting Allan deviation plot from the simulated signal agrees well with the formula and is shown in Figure 2.3 in Chapter 2. Since the natural logarithm rises very slowly for large numbers, a measurement duration or sample time even twice as long would only create slightly different bias instability.

A.3. Integration of 1/f Noise

It was postulated in [30] and [90] that the 1 σ standard deviation angle error of an integrated angular rate signal consisting solely of bias instability noise can be described by

$$\sigma_{\theta,\mathrm{BIS}} \approx Bt. \tag{A.42}$$

While the expression provides a good and easy-to-handle approximation, the actual mathematical background is quite challenging and no exact derivation has been published as far as the author is aware. In this section, an attempt at a more rigorous description of the problem is made.

Assume a discrete random process $v[k]$ which adheres to a 1/f noise spectrum with a power spectral density level at 1 Hz of $N_{1\mathrm{Hz}}$ and a variance of $\sigma^2_{1/\mathrm{f}}$ as defined above. The amount of samples is N and constant sample time shall be τ_0, so that time is $t = N\tau_0$. The integration of $v[k]$ is given by

$$v_1[N] = \tau_0 \sum_{k=1}^{N} v[k]. \tag{A.43}$$

Accordingly, the variance of $v_1[N]$ is

$$\begin{aligned}
\mathrm{Var}(v_1[N]) &= \mathrm{Var}(\tau_0 \sum_{k=1}^{N} v[k]) && \text{(A.44)}\\
&= \tau_0^2 \mathrm{Var}(\sum_{k=1}^{N} v[k]) && \text{(A.45)}\\
&= \tau_0^2 \Big(\sum_{k=1}^{N} \mathrm{Var}(v[k]) \; + \sum_{i,j=1;i\neq j}^{N} \mathrm{Cov}(v[i], v[j]) \Big) && \text{(A.46)}\\
&= \tau_0^2 \Big(\sum_{k=1}^{N} \mathrm{Var}(v[k]) \; + \sum_{i,j=1;i\neq j}^{N} R_{vv}(i,j) \Big) && \text{(A.47)}\\
&= \tau_0^2 \Big(N\sigma^2_{1/\mathrm{f}} \; + \sum_{i,j=1;i\neq j}^{N} R_{vv}(i,j) \Big) && \text{(A.48)}
\end{aligned}$$

where R_{vv} denotes the autocovariance of v. In finding R_{vv} we follow the derivation in [191]. Autocorrelation R_{xx} of a real-valued signal and single-sided power spectral density S_{PSD} are connected by the Fourier transform [191]

$$R_{xx}(\tau) = \int_0^{\infty} S_{\mathrm{PSD}} \cos(2\pi\tau f)\,\mathrm{d}f. \tag{A.49}$$

As in the derivation of variance above, the integral is only defined, when the lower bound is not zero.

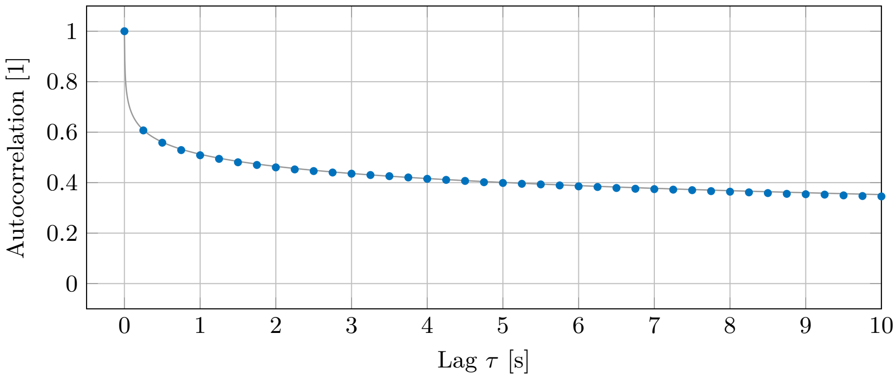

Figure A.1.: Sample autocorrelation (*blue dots*) of a simulated 1/f noise signal with a total length of $T_{\text{end}} = T_1 = 5\,\text{h}$ and $\tau_0 = 0.005\,\text{s}$. For better clarity, only every fiftieth sample was plotted. The autocorrelation function (*gray line*) from the autocovariance in equation (A.53) predicts the pattern well.

We therefore assume the power spectral density of 1/f noise to be

$$S_{\text{PSD},1/\text{f}} \approx \begin{cases} \frac{N_{1\text{Hz}}}{f} & \text{for} \quad f_1 < f < f_2 \\ 0 & \text{otherwise.} \end{cases} \tag{A.50}$$

One receives

$$R_{vv}(\tau) \approx \int_{f_1}^{f_2} \frac{N_{1\text{Hz}}}{f} \cos(2\pi\tau f)\,\text{d}f \tag{A.51}$$

$$\approx \begin{cases} N_{1\text{Hz}}\Big(\text{Ci}(2\pi\tau f_2) - \text{Ci}(2\pi\tau f_1)\Big) & \text{for} \quad \tau \neq 0 \\ N_{1\text{Hz}} \ln \frac{f_2}{f_1} & \text{for} \quad \tau = 0. \end{cases} \tag{A.52}$$

Note that $R_{vv}(\tau = 0)$ is the variance, identical to equation (A.36) above. The cosine integral functions Ci can be approximated by Taylor expansion [191]. If the 1/f behavior is assumed to reach from $f_2 = \frac{1}{2\tau_0}$ down to $f_1 = \frac{1}{T_1}$, then

$$R_{vv}(\tau) \approx \begin{cases} N_{1\text{Hz}}\Big(-\gamma - \ln(|2\pi\tau\frac{1}{T_1}|)\Big) & \text{for} \quad \tau \neq 0 \\ N_{1\text{Hz}} \ln \frac{T_1}{2\,\tau_0} & \text{for} \quad \tau = 0, \end{cases} \tag{A.53}$$

where $\gamma \approx 0.577$ is the Euler-Mascheroni constant. Figure A.1 shows the autocorrelation function, i.e. R_{vv} normalized by variance, in comparison to the sample autocorrelation of a 10 h simulated 1/f noise signal. Note, that the autocorrelation function is independent of the spectral noise level $N_{1\text{Hz}}$ because of the normalization. Evidently, equation A.53 describes the results from simulation well. The long correlation times of 1/f noise also become apparent.

The variance of integrated 1/f noise is now approximated by

$$\begin{aligned}
\mathrm{Var}(v_1) &= \tau_0^2\Big(N\sigma^2_{1/\mathrm{f}} \;+ \sum_{i,j=1;i\neq j}^{N} R_{vv}(i,j)\Big) && \text{(A.54)}\\
&\approx N_{1\mathrm{Hz}}\tau_0^2\Big(N\ln\frac{T_1}{2\,\tau_0} \;+ \sum_{i,j=1;i\neq j}^{N} -\gamma - \ln(|\frac{2\pi}{T_1}(i-j)\tau_0|)\Big) && \text{(A.55)}\\
&\approx \frac{B^2}{\pi}\tau_0^2\Big(N\ln\frac{T_1}{2\,\tau_0} \;+ \sum_{i,j=1;i\neq j}^{N} -\gamma - \ln(|\frac{2\pi}{T_1}(i-j)\tau_0|)\Big) && \text{(A.56)}\\
&\approx \frac{B^2}{\pi}\tau_0^2\Big(N\ln\frac{T_1}{2\,\tau_0} \;+ \sum_{i,j=1;i\neq j}^{N} -\gamma - \ln(\frac{2\pi\tau_0}{T_1}) - \ln(|i-j|)\Big) && \text{(A.57)}\\
&\approx \frac{B^2}{\pi}\tau_0^2\Big(N\ln\frac{T_1}{2\,\tau_0} \;+ (N^2-N)\big(-\gamma - \ln(\frac{2\pi\tau_0}{T_1})\big) - \sum_{i,j=1;i\neq j}^{N} \ln(|i-j|)\Big)
\end{aligned}$$

which can be closely approximated by dropping the linear N terms

$$\begin{aligned}
&\approx \frac{B^2}{\pi}\tau_0^2\Big(N^2\big(-\gamma - \ln(\frac{2\pi\tau_0}{T_1})\big) - \sum_{i,j=1;i\neq j}^{N} \ln(|i-j|)\Big) && \text{(A.58)}\\
&\approx \frac{B^2}{\pi}\Big(N^2\tau_0^2\big(-\gamma + \ln(\frac{T_1}{2\pi\tau_0})\big) - \tau_0^2\sum_{i,j=1;i\neq j}^{N} \ln(|i-j|)\Big). && \text{(A.59)}
\end{aligned}$$

Finally, one may reformulate for better numeric efficiency.

$$\mathrm{Var}(v_1) \approx \frac{B^2}{\pi}\Big(N^2\tau_0^2\big(-\gamma + \ln(\frac{T_1}{2\pi\tau_0})\big) - 2\tau_0^2\ln\big(\prod_{i=1}^{N-1}(N-i)^i\big)\Big) \tag{A.60}$$

Patently, $\sqrt{\mathrm{Var}(v_1)} = \sigma_{\theta,\mathrm{BIS}}$ is not a linear function of time $t = N\tau_0$.

$$\sigma_{\theta,\mathrm{BIS}} \approx B\sqrt{\frac{N^2\tau_0^2}{\pi}\big(-\gamma + \ln(\frac{T_1}{2\pi\tau_0})\big) - \frac{2\tau_0^2}{\pi}\ln\big(\prod_{i=1}^{N-1}(N-i)^i\big)} \tag{A.61}$$

Several other observations are noteworthy. When simulating for different parameter values, $\sigma_{\theta,\mathrm{BIS}}$ was found to be largely invariant to changes of sampling time τ_0. It is however influenced significantly by T_1. Figure A.2 plots equation (A.61) for values of T_1 from $200\,s$ to 3200 s. The larger the values, the more linear the plot becomes. In doing so, equation (A.61) keeps growing slowly to infinity with increasing slope for larger and larger T_1. This behavior is entirely expected, because as a “true” 1/f noise extending down all the way to $f_1 = \frac{1}{T_1} = 0\,\mathrm{Hz}$ has infinite variance, the integrated signal must also have infinite variance.

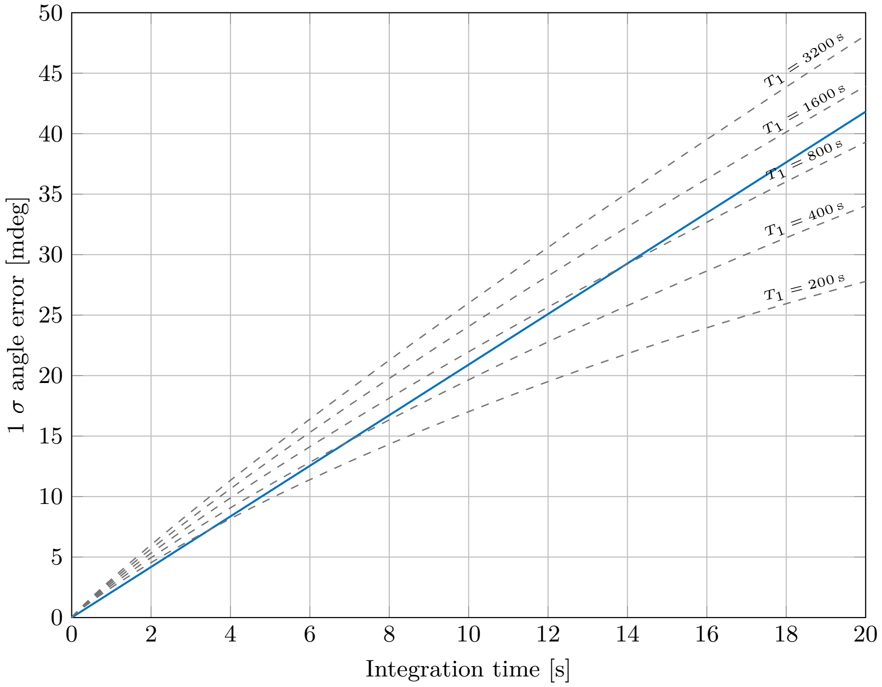

Figure A.2.: 1 σ angle error of an integrated angular rate signal with bias instability of $0.664B = 5$ dph described by the rough approximation $\sigma_{\theta,\mathrm{BIS}} \approx Bt$ (*blue*) in comparison to the analytically derived equation (A.61) for different values of T_1 (*gray, dashed*).

In summary, $\sigma_{\theta,\mathrm{BIS}} \approx Bt$ roughly matches the analytically derived equation for integration times of 20 s and reasonable values of T_1. Since no universal statement of the actual value of T_1 can be made in practice, $\sigma_{\theta,\mathrm{BIS}} \approx Bt$ constitutes a valid approximation. It is therefore used throughout this thesis. As described in the previous section, the fundamental contradiction of 1/f noise remains, namely that observed 1/f noise typically extends further and further to lower frequencies if measured for longer times, but that also its variance cannot be infinite.

A.4. Temperature Drift and Navigation

This section evaluates the influence of temperature drifts on the final navigation error in comparison to the noise-induced errors from Section 2.3. Assume, that the sensor's temperature changes linearly during the navigation period starting with zero offset at time $t = 0$. All other errors that appeared before the purely inertial navigation period are assumed to have been estimated perfectly by a suitable Kalman filter mechanism. The temperature induced offset behavior is described by

$$\Omega_T(t) = k_T \frac{\Delta T}{T_{\text{end}}} t, \tag{A.62}$$

where k_T is the temperature coefficient of the offset (TCO) in units of dps/K and ΔT the temperature difference that occurs during the navigation duration T_{end}. Integration promts the resulting angle error

$$\theta_T(t) = k_T \frac{\Delta T}{2\, T_{\text{end}}} t^2, \tag{A.63}$$

as well as the position error due to erroneous gravity compensation assuming a small angle approximation, i.e. the vehicle driving on a level surface.

$$x_T(t) = k_T \frac{\Delta T}{24\, T_{\text{end}}} t^4 \cdot \frac{\pi}{180}\, 9.81 \left[\frac{\text{rad}}{\text{deg}} \frac{\text{m}}{\text{s}^2}\right]. \tag{A.64}$$

The parameters are assumed to be

$$k_{T1} = 0.05\,\text{dps/K} \tag{A.65}$$

$$k_{T2} = 0.001\,\text{dps/K} \tag{A.66}$$

$$T_{\text{end}} = 20\,\text{s}, \tag{A.67}$$

where k_{T1} is representative for consumer-type MEMS and k_{T2} for best-of-class automotive devices. Figures A.3 and A.4 show the results in comparison to the stochastic error contributions. A sensor with a TCO similar to k_{T1} will most likely be limited by deterministic temperature effects in most practical applications, whereas a sensor with a TCO of k_{T2} will be limited equally or even dominantly by its stochastic properties. It is important to note, that temperature changes of several Kelvin within just 20 s are worst-case assumptions. For a continuously operating sensor inside a housing that is sensibly placed within a vehicle, very slow temperature drifts are expected at most times. Furthermore, the stochastic errors constitute $1\,\sigma$ value compared to the absolute measure of the deterministic errors.

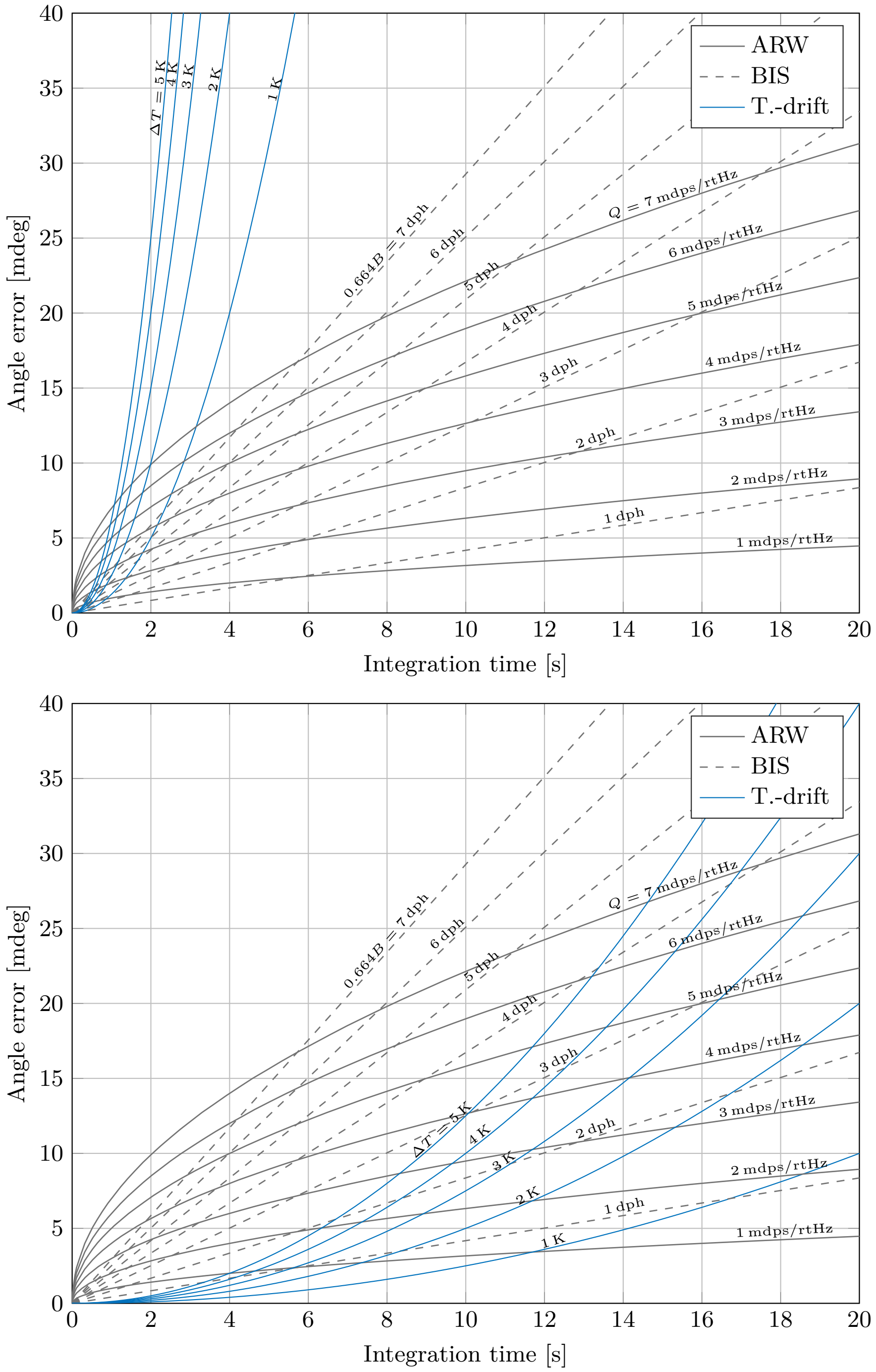

Figure A.3.: *Top:* Analytical angle error after single integration for different values of linear temperature drift (*blue*) with a TCO of $k_{T1} = 0.05\,\mathrm{dps/K}$ and $1\,\sigma$ standard deviation of angle random walk and bias instability errors (*both gray*). *Bottom:* The same assessment for a TCO of $k_{T2} = 0.001\,\mathrm{dps/K}$.

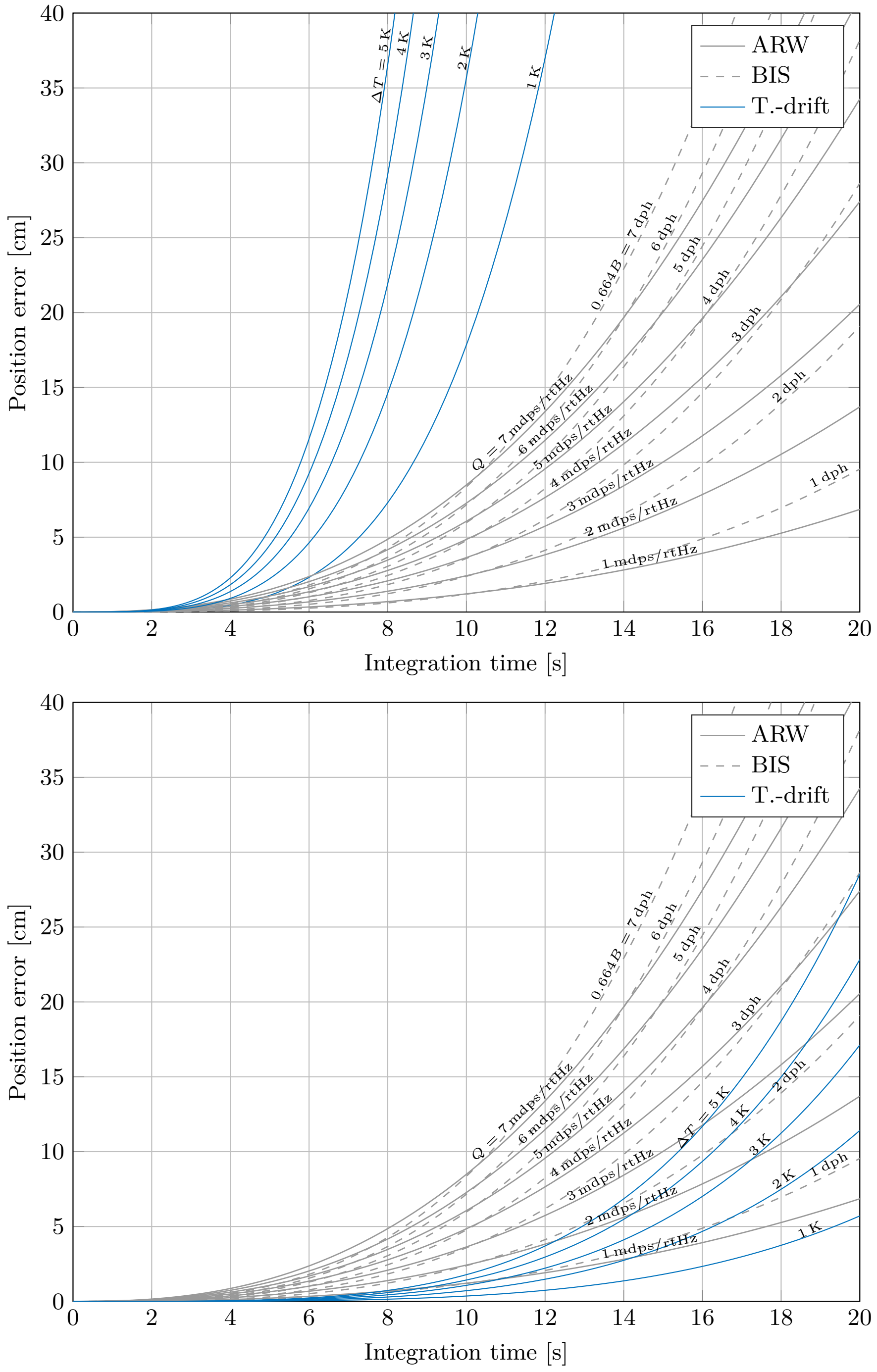

Figure A.4.: *Top:* Analytical position error due to faulty gravity compensation after triple integration for different values of linear temperature drift (*blue*) with a TCO of $k_{T2} = 0.05\,\mathrm{dps/K}$ and $1\,\sigma$ standard deviation of angle random walk and bias instability errors (*both gray*). *Bottom:* The same assessment for a TCO of $k_{T2} = 0.001\,\mathrm{dps/K}$.

A.5. Navigation Simulation Plots

The following Figures A.5 to A.8 show 50 iterations of the conservative emergency stop scenario with panning over to the road shoulder using the noise parameters from Table 2.2. Angular rates are small and braking deceleration is about one third of gravitational acceleration. Note, that the vertical axes do not always have equal scaling.

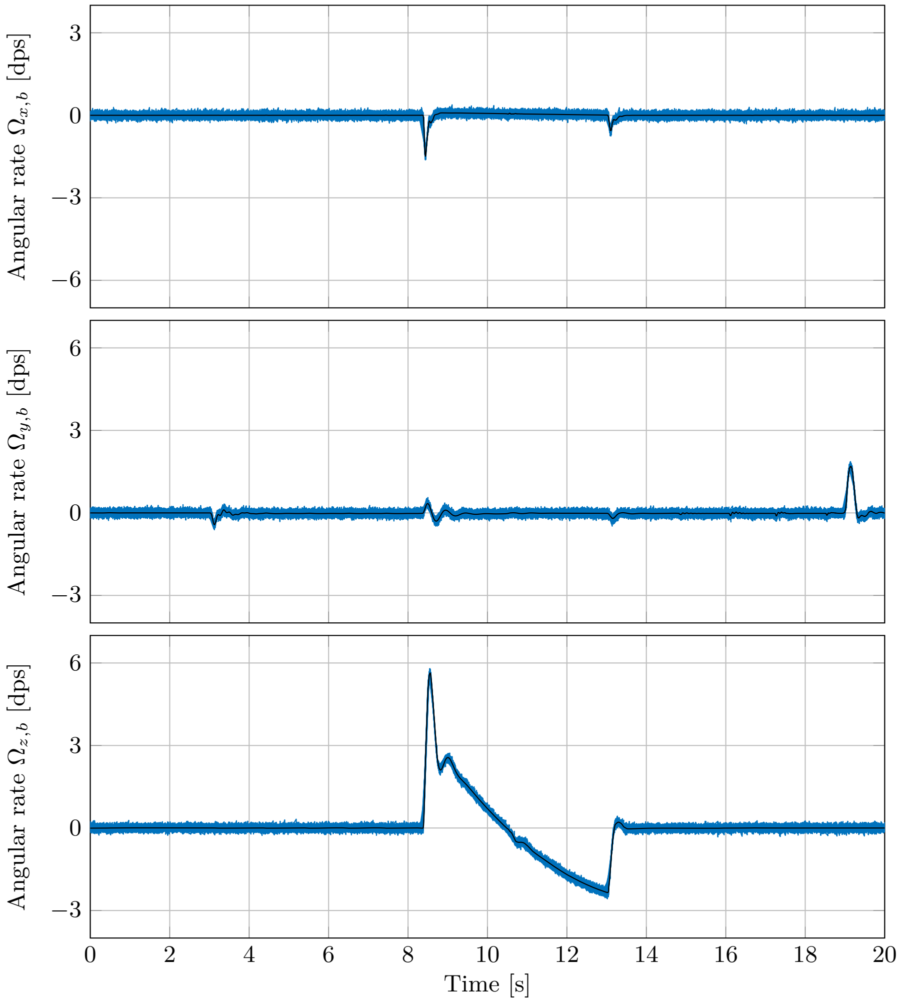

Figure A.5.: Angular rate time series plots of 50 simulation iterations (*blue*) of the conservative emergency stop scenario. The ground-truth is shown in black.

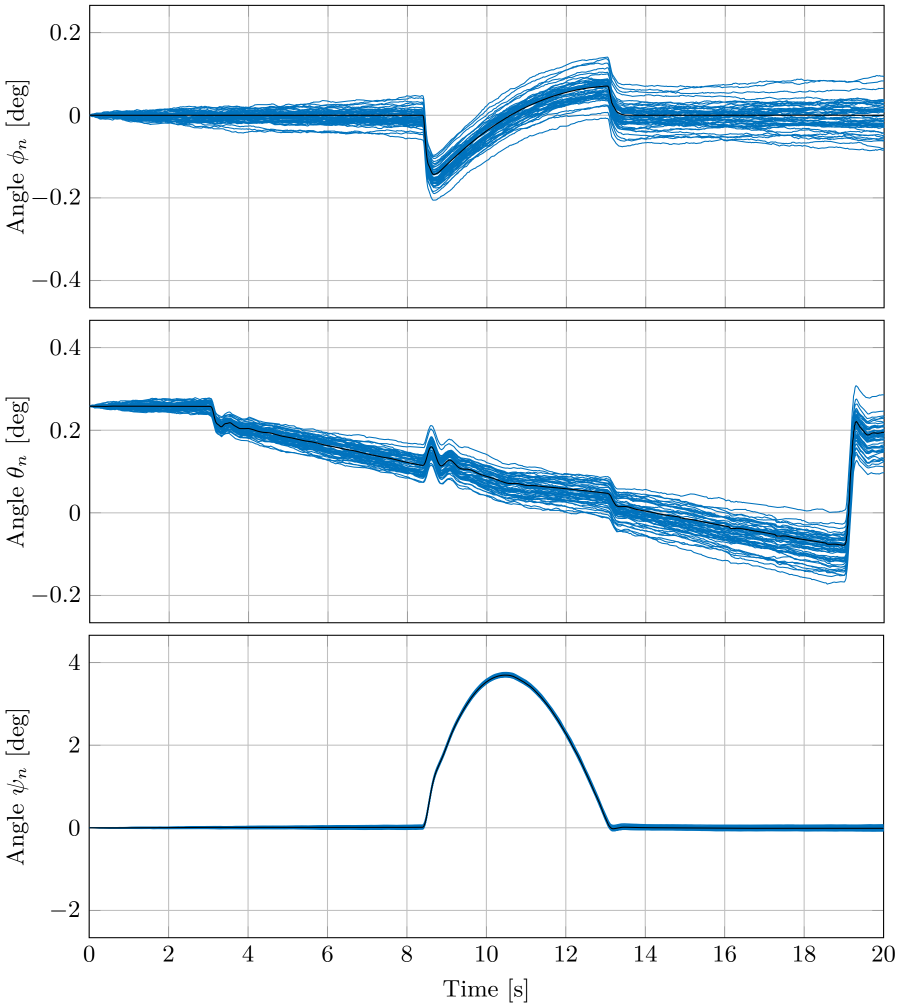

Figure A.6.: Attitude time series plots of 50 simulation iterations (*blue*) of the conservative emergency stop scenario. The ground-truth is shown in black.

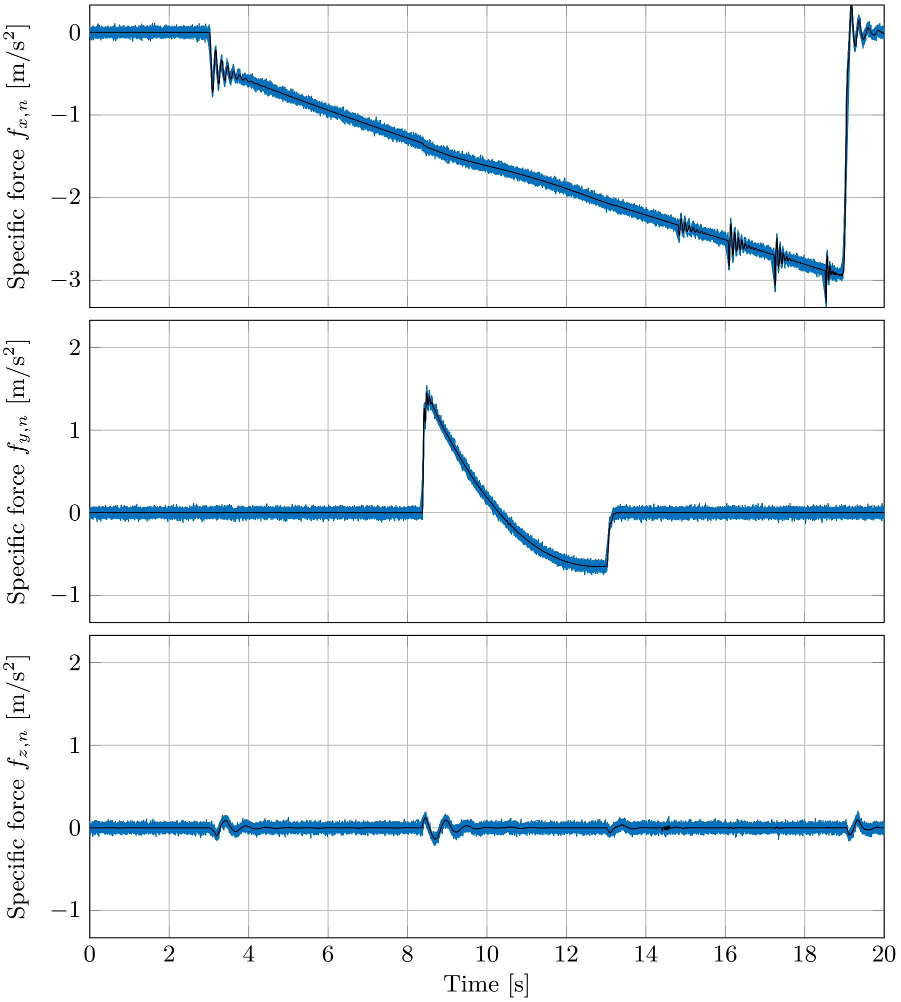

Figure A.7.: Acceleration time series plots of 50 simulation iterations (*blue*) of the conservative emergency stop scenario. The ground-truth is shown in black.

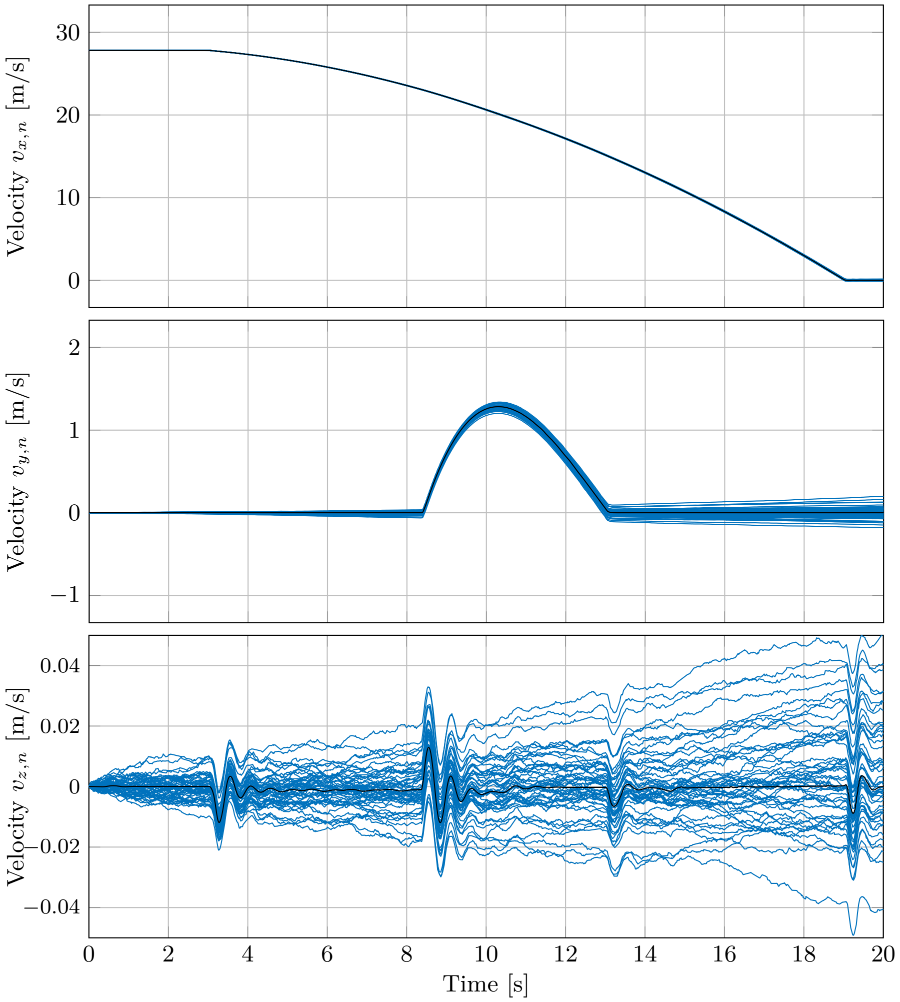

Figure A.8.: Velocity time series plots of 50 simulation iterations (*blue*) of the conservative emergency stop scenario. The ground-truth is shown in black.

A.6. Sensor Redundancy

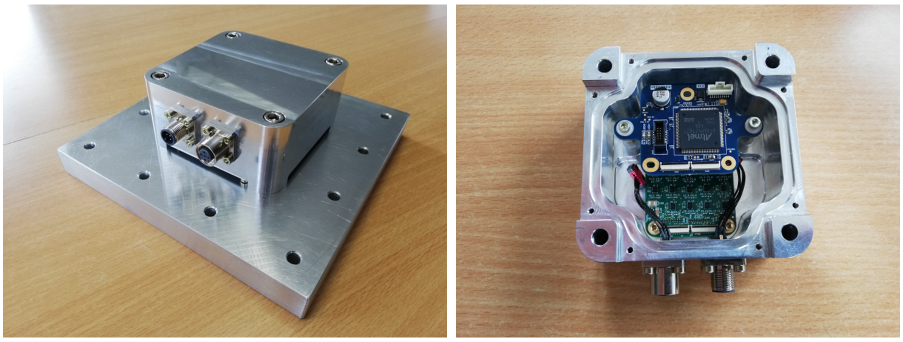

Figure A.9.: MEMS inertial sensor redundancy demonstrator as it was developed within our research group. A powerful micro-controller (*blue PCB*) and an array of 14 open-loop or 6 closed-loop triaxial, consumer-type MEMS gyroscopes (*green PCB*) are housed within a milled aluminium casing. See also [190] for more details on the setup.

Throughout the author's PhD work, some research on MEMS inertial sensor redundancy was conducted, mostly by supervision of several student theses and internships on this topic. Here, a brief summary on current challenges in this field and our findings is provided.

A natural approach for improving precision, robustness and for integrity monitoring [194] is to use redundant gyroscopes and to fuse their signals [195] [196] [197]. Sometimes, these configurations are called virtual gyroscopes [198]. In many scientific contributions, hopes are raised, that favorable, negative noise correlations between individual devices may exist [198] [199] [200]. To the knowledge of the author, none were ever experimentally demonstrated, however. This comes as no surprise, as noise sources typically originate in the individual sensor's analog circuits or its MEMS element. Even when fabricated on a single die, four gyroscopes were shown to have no significant negative correlation between them [201]. If the signals of N number of sensors are not correlated to each other, the noise (e.g. angle random walk or bias instability) improvement is limited to a factor of $\sqrt{N}$ [202]. Another recent paper shows an array of 72 gyroscopes that also exhibit only very minimal correlation [203]. In their implementation, using a Kalman filter is no better than simple (weighted) averaging. The authors of [204] reach the same conclusion, if all sensors have the same error characteristic. The excellent contribution [60] furthermore finds, that the correlations between the bias drifts of the signals cannot be estimated in their Kalman filter implementation, as the noise from angle random walk is too dominant. Successful implementation of a Kalman filter also requires high-quality models of the vehicle dynamics with further inputs like steering angle. If a Kalman filter is implemented purely for fusing redundant gyroscopes, most publications assume a simple model of zero angular rate, which of course smooths any measurement at rest. The usefulness during actual, high-dynamic movement is limited, however. The results in our group also did not show significant negative *noise* correlations, even when the devices were placed 90 deg rotated on opposing sides of a PCB [205]. Correlations for deterministic effects, e.g. due to temperature were abundant, though. Figure A.9 shows our current demonstrator setup. The authors of [206] also provide an extensive experimental characterization of differently placed sensors. It was furthermore noted in the review article [207], that some manufacturers may pick their best devices from the middle of a bell-curve distribution. Their low-cost product line may therefore have sensors with strong deterministic error effects acting in one *or* the other direction. Redundancy may then be used to compensate these effects.

In summary, improving angle random walk by e.g. a factor of two by using four sensors may be entirely practical, especially considering how much traditional engineering effort would be necessary to achieve the same feat on a single device. The benefit of adding additional sensors quickly falls off, according to the $\sqrt{N}$-law. Arrays with much more than ten devices seem thus less feasible. Redundancy is furthermore particularly suited for use of less expensive, consumer-type MEMS sensors. Use cases for these kinds of configurations may include mobility applications, that do not require full automotive certification like pedestrian dead-reckoning [208] [209], visual-inertial odometry [210] [211], electrified scooters or bicycles [212] [213], some construction site applications [214], agricultural robotics [215] or use-cases in professional sports [195] [216]. The shortcomings of consumer-type sensors for example in the area of vibration robustness may be effectively mitigated by redundancy as demonstrated by our group in [190]. There, a scheme evaluated the relative difference of one sensor to all other sensors of the same type and lowered or increased its influence on the final, virtual output accordingly.

Additional Scale-Factor Instability Experiments

The redundancy demonstrator was furthermore used to examine scale-factor instability effects in open-loop and closed-loop gyroscopes. Figure A.10 shows the Allan deviation of the z-axis of five open-loop and five closed-loop devices at rest and at a constant applied angular rate of 200 dps within an ultra-high precision rate chamber, compare Figure A.13. It was found, that the closed-loop devices had a large increase of “bias” instability with applied angular rate, whereas the open-loop devices displayed the same bias instability level compared to measurement at rest. The experiment also makes clear, that the measured scale-factor instability here and in Section 3.5 is a sensor-internal effect and is not produced by inaccuracies of the motion of the rate chamber. Particularly for use-cases with enduring, one-directional rotation, e.g. sensor placement within a wheel, an open-loop gyroscope would be preferable based on these results.

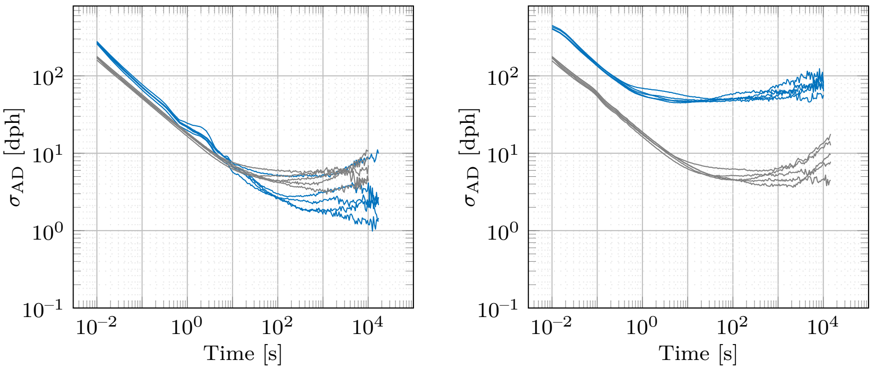

Figure A.10.: Allan deviation of five open-loop gyroscope z-axes (*gray*) and five closed-loop gyroscope z-axes (*blue*). *Left:* Measurement at rest, i.e. zero rotation. *Right:* Measurement at 200 dps of applied rate within a rotation chamber.

A.7. Gyroscope Simulation Overview

The figures below provide an overview of the Matlab/Simulink structure.

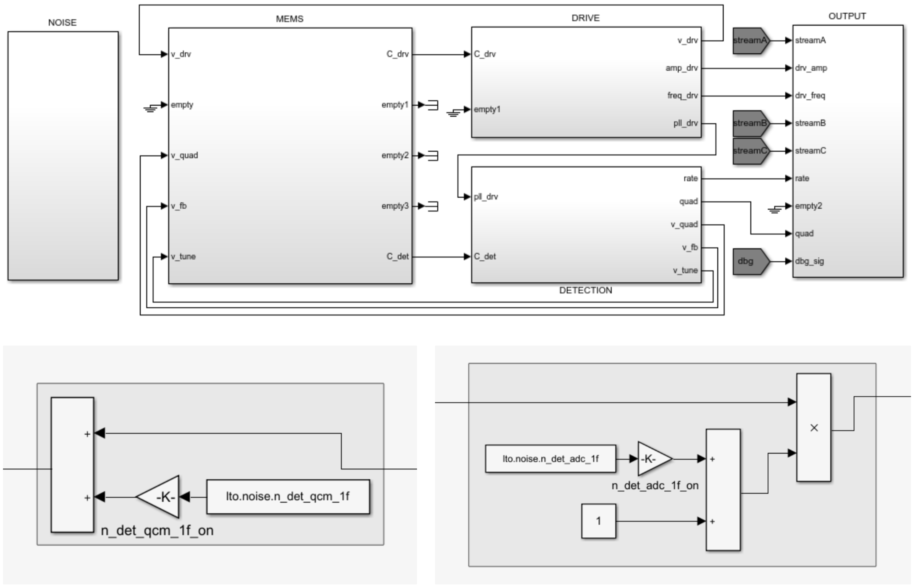

Figure A.11.: *Top:* Overview of a single-axis MEMS gyroscope modeled in Simulink. The dynamic equations from Section 3.2 are included in the MEMS subsystem. Drive and sense control transfer-functions are similar to the experimental device. *Bottom:* Flicker noise was modeled additively for e.g. the quadrature compensation common-mode voltage (*left*) or multiplicatively for the drive and sense ADCs (*right*) in the Simulink simulation.

A.8. Negating Offset Susceptibility

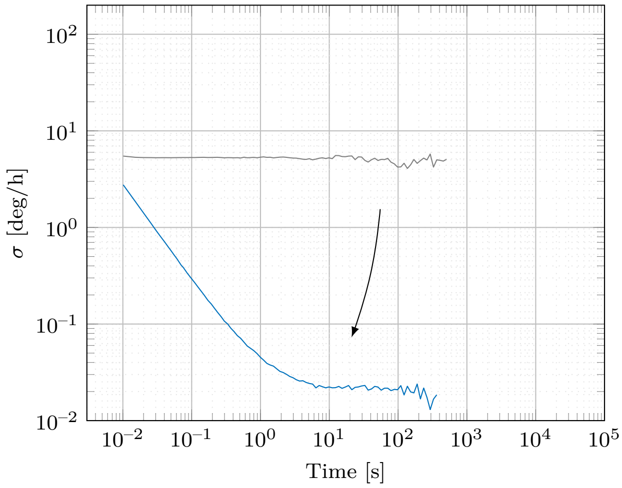

Figure A.12.: Simulated bias instability of 5.3 dph with 0.1 dps of electrical cross-coupling offset and frequency tuning voltage flicker (*gray*). An improvement to far below 0.1 dph (*blue*) is facilitated by allowing an artificial quadrature offset of 39 dps which counteracts the susceptibility of the electrical cross-coupling offset, so that the total susceptibility becomes near zero. All noise sources except the dithers were turned off for this simulation.

The detrimental offset susceptibility to frequency tuning changes created by e.g. electrical cross-coupling or additional modes may be counteracted by purposely introducing a quadrature offset as in Figure 3.2, creating the same amount of offset susceptibility but with opposing sign. Figure A.12 demonstrates the functionality in simulation, where all white noise sources except the dithers have been turned off to make bias instability more visible and to reduce simulation time. The advantage of this method lies in its simplicity. No additional tones are necessary and angle random walk is not increased. The method does however require part-individual calibration, which is not necessary for the pilot tone scheme. The calibration might be automatically performed at each sensor start-up, as long as the gyroscope is at rest for some seconds. It is important to note, that this method does not improve non-ideal mode-matching, but merely the rate output. Furthermore, even small phase changes of the drive frequency ω_{pll} would change the amount of quadrature that appears in rate. As these phase changes cannot be precluded, the viability of this method is deemed limited in actual experiment.

A.9. Derivation of Pilot Tone Measure

The pilot tones S_{pt} are applied to the sense CV converter, left and right of the drive frequency.

$$\begin{aligned} S_{\mathrm{pt}}(t) &= k_{\mathrm{pt}} \cos(\omega_{\mathrm{pt}} t) \cos(\omega_{\mathrm{pll}} t) && \text{(A.68)} \\ &= \frac{k_{\mathrm{pt}}}{2} \cos\big((\omega_{\mathrm{pll}} - \omega_{\mathrm{pt}})t\big) + \frac{k_{\mathrm{pt}}}{2} \cos\big((\omega_{\mathrm{pll}} + \omega_{\mathrm{pt}})t\big) && \text{(A.69)} \end{aligned}$$

The CV transfer function amplifies both tones with k'_{pt} and changes their phase opposingly by ϕ_{pt}. Assume there exists a detuning of drive and sense modes so that the left tone is reduced in amplitude by k_{det} and the other one concurrently increased. The detuning phase change ϕ_{det} is the same for both tones.

$$\begin{aligned} S_{\mathrm{pt,det}}(t) = &\frac{k'_{\mathrm{pt}}(1 - k_{\mathrm{det}})}{2} \cos\big((\omega_{\mathrm{pll}} - \omega_{\mathrm{pt}})t + \phi_{\mathrm{pt}} + \phi_{\mathrm{det}}\big) \\ &+ \frac{k'_{\mathrm{pt}}(1 + k_{\mathrm{det}})}{2} \cos\big((\omega_{\mathrm{pll}} + \omega_{\mathrm{pt}})t - \phi_{\mathrm{pt}} + \phi_{\mathrm{det}}\big). && \text{(A.70)} \end{aligned}$$

To retrieve the detuning information $D_{\mathrm{pt}}(t)$, the force control output signal containing $S_{\mathrm{pt,det}}(t)$ is synchronously demodulated with $2S_{\mathrm{pt}}(t)/k_{\mathrm{pt}}$,

$$\begin{aligned} D_{\mathrm{pt}}(t) &= S_{\mathrm{pt,det}}(t) 2 S_{\mathrm{pt}}(t)/k_{\mathrm{pt}}. && \text{(A.71)} \\ &= k'_{\mathrm{pt}} \big[(1 - k_{\mathrm{det}}) \cos\big((\omega_{\mathrm{pll}} - \omega_{\mathrm{pt}})t + \phi_{\mathrm{pt}} + \phi_{\mathrm{det}}\big) \\ &\quad + (1 + k_{\mathrm{det}}) \cos\big((\omega_{\mathrm{pll}} + \omega_{\mathrm{pt}})t - \phi_{\mathrm{pt}} + \phi_{\mathrm{det}}\big)\big] \\ &\quad \cdot \big[\cos\big((\omega_{\mathrm{pll}} - \omega_{\mathrm{pt}})t\big) + \cos\big((\omega_{\mathrm{pll}} + \omega_{\mathrm{pt}})t\big)\big] && \text{(A.72)} \\ &= \frac{k'_{\mathrm{pt}}}{2} \Big[(1 - k_{\mathrm{det}}) \Big(\cos(\phi_{\mathrm{pt}} + \phi_{\mathrm{det}}) + \cos(2(\omega_{\mathrm{pll}} - \omega_{\mathrm{pt}})t + \phi_{\mathrm{pt}} + \phi_{\mathrm{det}})\Big) \\ &\quad + (1 - k_{\mathrm{det}}) \Big(\cos(-2\omega_{\mathrm{pt}} t + \phi_{\mathrm{pt}} + \phi_{\mathrm{det}}) + \cos(2\omega_{\mathrm{pll}} t + \phi_{\mathrm{pt}} + \phi_{\mathrm{det}})\Big) \\ &\quad + (1 + k_{\mathrm{det}}) \Big(\cos(2\omega_{\mathrm{pt}} t - \phi_{\mathrm{pt}} + \phi_{\mathrm{det}}) + \cos(2\omega_{\mathrm{pll}} t - \phi_{\mathrm{pt}} + \phi_{\mathrm{det}})\Big) \\ &\quad + (1 + k_{\mathrm{det}}) \Big(\cos(-\phi_{\mathrm{pt}} + \phi_{\mathrm{det}}) + \cos(2(\omega_{\mathrm{pll}} + \omega_{\mathrm{pt}})t - \phi_{\mathrm{pt}} + \phi_{\mathrm{det}})\Big)\Big] \end{aligned}$$

After suitable low-pass filtering one receives only the "constant" components

$$\begin{aligned} D_{\mathrm{pt,lp}} &= \frac{k'_{\mathrm{pt}}}{2} (1 - k_{\mathrm{det}}) \cos(\phi_{\mathrm{pt}} + \phi_{\mathrm{det}}) + \frac{k'_{\mathrm{pt}}}{2} (1 + k_{\mathrm{det}}) \cos(-\phi_{\mathrm{pt}} + \phi_{\mathrm{det}}) \\ &= k'_{\mathrm{pt}} \big(\cos(\phi_{\mathrm{pt}}) \cos(\phi_{\mathrm{det}}) + k_{\mathrm{det}} \sin(\phi_{\mathrm{pt}}) \sin(\phi_{\mathrm{det}})\big). && \text{(A.73)} \end{aligned}$$

Since cosine is an even function, the left term cannot differentiate the sign of detuning, but the right term does. The pilot tone measure therefore has a small offset which amounts to $D_{\mathrm{pt,lp,ideal}} = k'_{\mathrm{pt}} \cos(\phi_{\mathrm{pt}})$ at ideal tuning, as in Figure 4.6.

A.10. Derivation of Bias Instability Factor

Equation (2.12) or [50] defines bias instability for frequencies below a certain cutoff frequency as

$$\sigma^2_{\mathrm{BIS}} = \frac{2\ln 2}{\pi} B^2. \tag{A.74}$$

The coefficient B is furthermore related to the two-sided power spectral density $S_{2\mathrm{PSD}}$ of 1/f noise according to [50] by

$$S_{2\mathrm{PSD}}(f) = \frac{B^2}{2\pi}\frac{1}{f}. \tag{A.75}$$

Substituting equation (A.74) into (A.75) and dividing by 2 for the one-sided PSD grants

$$\sigma^2_{\mathrm{BIS}} = 2\ln 2\, S_{\mathrm{PSD}} f. \tag{A.76}$$

Because the power spectrum of Flicker noise is not constant over frequency, it is typically specified with its magnitude at $f = 1\,\mathrm{Hz}$. We therefore write

$$\sigma^2_{\mathrm{BIS}} = 2\ln 2\, N_{1\mathrm{Hz}} \cdot 1\,\mathrm{Hz}. \tag{A.77}$$

The relationship between flicker noise with a one-sided root power spectral density at 1 Hz, $\sqrt{N}_{1\mathrm{Hz}}$, and its Allan deviation is thus

$$\sigma_{\mathrm{BIS}} = \sqrt{N}_{1\mathrm{Hz}}\sqrt{2\ln 2}\,\mathrm{rtHz}. \tag{A.78}$$

Here, σ_{BIS} is a dimensionless quantity and $\sqrt{N}_{1\mathrm{Hz}}$ is in units of 1/rtHz. In order to determine the effect of flicker voltage V_{flic} to the Allan deviation of a rate offset, we need to factor in the experimentally found susceptibility of said offset created by voltage change, S_V, in units of dps/V.

$$\sigma_{\mathrm{BIS},V} = |S_V|\, V_{\mathrm{flic}}\sqrt{2\ln 2}\,\mathrm{rtHz}. \tag{A.79}$$

The calculation for scale-factor instability works analogously. Deciding is the difference between the actual angular rate and the angular rate after scale-factor disturbance by small feedback voltage variation, which is approximately $|\Omega| \cdot 2\frac{\Delta V_{\mathrm{FB}}}{V_{\mathrm{FB}}}$ in units of dps, see equation (3.41). In terms of rate offset change per voltage change one therefore receives $|\Omega| \cdot \frac{2}{V_{\mathrm{FB}}}$ and thus

$$\sigma_{\mathrm{SIS},V_{\mathrm{FB}}} = |\Omega| \cdot 2\frac{V_{\mathrm{FB,flick}}}{V_{\mathrm{FB}}} \cdot \sqrt{2\ln 2}\,\mathrm{rtHz}. \tag{A.80}$$

A.11. Derivation of Scale-Factor Change

Figure A.13.: An ultra-high precision rotation chamber was used to analyze scale-factor instability effects by continuously rotating the sensors at a constant angular rate for extended durations on the order of 24 h and longer.

Here, the derivation for scale-factor in the presence of feedback voltage changes, equation (3.41), is provided. The term k_{fDAC} from equation (3.11) relates the digital signal in LSB to the output force generated by the force-feedback voltage

$$k_{\mathrm{fDAC}} = k_{\mathrm{fb}} \left(\frac{V_{\mathrm{fDAC,full\text{-}scale}}}{\mathrm{LSB}_{\mathrm{fDAC,full\text{-}scale}}} \right)^2 . \tag{A.81}$$

In our implementation, a single-bit DAC is used, hence

$$k_{\mathrm{fDAC}} = k_{\mathrm{fb}} V_{\mathrm{FB}}^2, \quad \text{where } V_{\mathrm{FB}} = 1.23\,V. \tag{A.82}$$

A non-ideal (i.e. not value 1) rate scale-factor due to variations ΔV_{FB} in force-feedback voltage is thus given by

$$\begin{aligned} \mathrm{SF}_{V_{\mathrm{FB}}} &= \frac{H_{\Omega_{\mathrm{r}} \to \star, \Delta_{\mathrm{FB}}}\big|_{\omega_y}}{H_{\Omega_{\mathrm{r}} \to \star, \mathrm{ideal}}\big|_{\omega_y}} && \text{(A.83)} \\ &\approx \frac{k_{\mathrm{fDAC,ideal}}}{k_{\mathrm{fDAC},\Delta_{\mathrm{FB}}}} && \text{(A.84)} \\ &\approx \frac{V_{\mathrm{FB}}^2}{(\Delta_{\mathrm{FB}} + V_{\mathrm{FB}})^2} . && \text{(A.85)} \end{aligned}$$

The principle also applies to multi-bit DACs, only that variations of several DAC voltage stages must be considered. Scale-factor instability is therefore not limited to single-bit force-feedback implementations, but is inherent to all force-feedback type implementations.